UNIVERSITY OF OKLAHOMA

GRADUATE COLLEGE

IMPACT OF ANTHROPOGENIC CONTAMINANTS ON POLAR ICE REFLECTIVITY AND HEAT ABSORPTION: SOOT AND CARBON NANOTUBES

A THESIS

SUBMITTED TO THE GRADUATE FACULTY

in partial fulfillment of the requirements for the

Degree of

MASTER OF SCIENCE

By REGIS OLUWANIFEMI NOUHESSEWA BONOU

Norman, Oklahoma

2026

IMPACT OF ANTHROPOGENIC CONTAMINANTS ON POLAR ICE REFLECTIVITY AND HEAT ABSORPTION: SOOT AND CARBON NANOTUBES

A THESIS APPROVED FOR THE

SCHOOL OF AEROSPACE AND MECHANICAL ENGINEERING

BY THE COMMITTEE CONSISTING OF

Dr. Wilson Merchan Merchan, Chair

Dr. Pejman Kazempor

Dr. Iman Ghamarian

Acknowledgements

I would like to extend my sincere gratitude to my committee chair, Dr. Wilson Merchan Merchan, for his constant guidance, advice, and support throughout this research. His thoughtful questions and critical perspective challenged me to think deeper and ultimately strengthened the scientific rigor of this work. I am truly grateful for his mentorship and the time he invested in helping me grow as a researcher.

I would like to thank Dr. Iman Ghamarian and Dr. Pejman Kazempor for their time and for serving on my committee.

I would like to acknowledge the Samuel Roberts Noble Microscopy Laboratory at the University of Oklahoma for providing access to advanced imaging facilities. I am especially grateful to Dr. Preston Larson for his significant assistance with the scanning electron microscopy (SEM) work. His guidance and support in SEM sample preparation, instrument operation, and image acquisition were essential to the success of this work.

My sincere thanks go to Greg Williams and the late Billy Mays, as well as everyone at the AME machine shop, for their innovative solutions to the many challenges I encountered. Their expertise and resourcefulness played a crucial role in bringing many of my ideas to life and provided invaluable support throughout my work.

Lastly, my deepest gratitude goes to my loved ones, my mom, dad, and siblings for their unwavering support, encouragement, and belief in me. They constantly reminded me of my strength and ability to achieve my goals, and this accomplishment would not have been possible without them.

Table of Contents

Table of Figures

Abstract

This thesis investigates the photothermal ice-melting effects of two anthropogenic carbonaceous contaminants; soot (black carbon) and carbon nanotubes (CNT) under controlled infrared radiation, examining how particle type, mass loading, deposition geometry, and ice structure govern the rate and spatial pattern of surface melting. The study focuses on ice samples prepared in custom 3D-printed containers under two structural configurations: crushed ice and solid ice which are subjected to surface, layered, and mixed-ratio contaminant deposition across a range of mass loadings from 5 mg to 1 g. The research adopts a systematic experimental approach, utilizing a four-thermocouple array embedded at defined heights within the ice column, a calibrated infrared radiation source, and high-frequency data acquisition at 240 Hz to resolve internal temperature profiles throughout each melting event. This detailed analysis reveals that photothermal heating is strictly surface-localized in all configurations: the highest thermocouple (TC4), positioned at the contaminant-ice interface, was the sole channel to register temperature rises driven by the surface deposit, while the lower thermocouples (TC1–TC3) remained thermally inert regardless of contaminant type, loading, or deposition method. Scanning electron microscopy characterization of both contaminants confirms their distinct morphologies; soot exhibiting spherical agglomerated nanoparticles and carbon nanotubes displaying high-aspect-ratio fibrous structures, which directly influence their optical absorptance and deposit packing behavior on the ice surface. Part of the study involves evaluating the non-monotonic relationship between contaminant mass and photothermal response, where both soot and carbon nanotubes exhibit complete suppression of surface heating at the intermediate 15 mg loading despite strong responses at 5 mg and 25 mg, and where mixed CNT-soot binary deposits at a fixed total mass of 25 mg produce a compositional window effect in which two specific ratios completely suppress

melting acceleration while three others remain active. These findings highlight the complexity of particle-level interactions in co-deposited carbonaceous layers and the limitations of linear albedo-reduction models for predicting contaminant-driven melt dynamics. Furthermore, scaled-up experiments and solid ice trials demonstrate that ice structure and substrate thermal conductivity are as important as contaminant properties in determining melt acceleration, with the same gram-scale soot deposit producing a 33.6-minute swing in surface melted onset time between crushed and solid ice substrates. This study enhances the understanding of anthropogenic carbonaceous particle interactions with ice surfaces and underscores the need for geometry- and substrate-aware parameterizations of aerosol-driven albedo reduction in polar climate models.

Chapter 1: Introduction

1.1 Background

Polar ice plays a critical role in regulating the Earth's climate system due to its high surface reflectivity, or albedo, which enables it to reflect a significant portion of incoming solar radiation back into space [1, 2]. This reflective capability is a key component of the global energy balance, particularly in the Arctic and Antarctic regions, where vast ice-covered surfaces act as natural cooling agents [2]. Any reduction in ice albedo results in increased solar absorption, leading to enhanced surface warming and accelerated melting [3]. This process contributes to a well-known positive feedback mechanism, commonly referred to as the ice–albedo feedback, which amplifies regional and global climate change [3]. As a result, understanding the factors that influence polar ice reflectivity is essential for improving predictions of climate evolution and associated environmental impacts.

One of the primary factors contributing to changes in ice albedo is the deposition of anthropogenic contaminants. Light-absorbing particles such as soot (black carbon), industrial emissions, and emerging engineered nanomaterials can be transported over long distances through atmospheric circulation [4, 5]. These particles originate from sources including fossil fuel combustion, biomass burning, and industrial processes, and can travel thousands of kilometers before being deposited in polar regions [5]. Despite their geographic remoteness, both the Arctic and Antarctic are increasingly affected by these contaminants due to global transport pathways and atmospheric dynamics [4]. Once deposited on ice surfaces, these particles alter the optical properties of the ice, significantly reducing its reflectivity [1].

The presence of carbonaceous materials on ice surfaces leads to increased radiative forcing by enhancing the absorption of incoming solar radiation [3, 6]. soot, in particular, is highly effective at absorbing visible light, causing surface darkening and localized heating [6] . This results in faster melting rates and further exposure of darker underlying layers, which in turn absorb even more radiation [3]. In addition to soot, carbon nanotubes (CNTs) represent a class of engineered nanomaterials with unique optical and thermal properties, including strong light absorption and high thermal conductivity [7, 8]. While CNTs are widely used in advanced engineering applications, their potential environmental impact in cryospheric systems remains largely unexplored [8]. Their nanoscale structure and interaction with ice surfaces may introduce distinct heat transfer mechanisms compared to traditional contaminants.

Although the effects of surface darkening and radiative forcing have been widely studied through field observations and climate modeling, there remains a significant gap in controlled laboratory investigations [2, 9]. Natural environments present complex and variable conditions, including fluctuating temperatures, wind effects, heterogeneous particle distributions, and varying ice structures [9]. These factors make it difficult to isolate the individual contributions of specific contaminants and to establish clear cause-and-effect relationships. In particular, comparative studies between soot and carbon nanotubes under controlled conditions are limited, and the influence of parameters such as particle concentration, deposition method, and ice structure is not fully understood [10].

This research aims to address these gaps through a systematic experimental investigation of the impact of soot and carbon nanotubes on ice reflectivity and heat absorption. The primary objective is to quantify how different types and concentrations of contaminants influence thermal response

and melting behavior in ice. It is hypothesized that both soot and CNTs will reduce ice albedo and increase heat absorption, leading to accelerated melting rates. Furthermore, due to their unique morphology and thermal properties, CNTs are expected to exhibit distinct behavior compared to soot, particularly in terms of heat distribution and interaction with the ice matrix. Additional hypotheses consider the role of deposition methods, ice type, and environmental conditions in modifying heat transfer mechanisms and melt dynamics.

This thesis is organized to systematically investigate the photothermal effects of carbonaceous contaminants on ice melting. Chapter 2 establishes the theoretical foundation, covering the thermophysical properties of ice, snow, soot, and carbon nanotubes, the heat transfer mechanisms present in the experiments, and the interaction between contaminants and ice surfaces. Chapter 3 characterizes the two contaminant materials (soot and CNT) through scanning electron microscopy, examining their morphology and particle size distributions. Chapter 4 details the experimental design, including the 3D-printed ice containers, ice preparation methods, thermocouple placement, contaminant deposition parameters, and environmental control conditions such as the radiation source and ambient temperature. Chapter 5 presents the experimental results across two ice types: crushed ice experiments covering surface deposition, layered deposition, mixed contaminant ratios, and a scaled-up geometry; and solid ice experiments examining embedded contaminants and a direct comparison between the two ice structures. Chapter 6 synthesizes the findings, discusses the dominant mechanisms identified across the experimental process, and presents the key conclusions alongside recommendations for future work.

1.2 Literature Review

1.2.1 Black Carbon in the Cryosphere: Sources, Distribution, and Historical Trends

The deposition of black carbon (BC) on snow and ice surfaces has emerged as one of the most consequential mechanisms linking anthropogenic pollution to cryospheric change. BC has been identified as an important short-lived climate forcer that, due to its light absorption properties, darkens snow and ice surfaces, perturbs the local energy balance, and accelerates the melting of glaciers, snow cover, and sea ice [11]. The origins of this contamination are well established: BC is produced by incomplete combustion of carbonaceous material (mainly fossil fuels and biomass) with vehicular emissions alone accounting for approximately 25% of global BC production [11].

From a historical perspective, ice core records reveal a rapid increase in BC concentrations beginning in the 1850s and continuing through the 20th century, consistent with rising emissions driven by industrialization, while a decline in BC concentrations observed in Arctic and European ice cores since the 1970s has been partially attributed to the introduction of clean air legislation [11]. This long-term record establishes a direct link between industrial activity and polar contamination. The radiative significance of BC is substantial: its globally averaged radiative forcing has been estimated at approximately 1.2 W m^{-2}, the second highest of any climate forcer after carbon dioxide [11]. At the regional scale, BC in snow has been linked to an increase in average annual glacier melt of 15–19% in the Alps, with mean annual mass balance reductions of approximately 280–490 mm water equivalent attributed to the BC effect [11].

1.2.2 Laboratory Evidence for Albedo Reduction by Black Carbon

While field observations and modelling studies have characterized the broad scope of BC-induced albedo loss, controlled laboratory experiments provide the mechanistic precision necessary to isolate individual variables and validate radiative transfer models. The foundational laboratory contribution in this domain is the work of Hadley and Kirchstetter [12], who generated BC-laden artificial snow under controlled conditions and demonstrated that contamination at levels representative of natural settings measurably reduces snow albedo. Critically, they showed that increasing snow grain size both decreases baseline albedo and amplifies the radiative perturbation caused by BC, thereby justifying the grain-aging positive feedback loops incorporated into contemporary climate models [12].

This finding establishes that snow grain morphology is not a passive background variable but an active determinant of BC's radiative impact. Radiation-transfer calculations indicate that BC concentrations on the order of 10 to 100 parts per billion by mass can decrease snow albedo by 1 to 5% [12] . A positive feedback is thereby initiated, as absorbed solar energy causes ice grains to melt, fuse, and grow faster than in clean snow, further reducing reflectivity [12]. A key limitation identified by Hadley and Kirchstetter is that in natural field settings, the BC effect is routinely masked by confounding variables including snow grain size, snow density, snow depth, solar zenith angle, and interactions with the underlying surface and tree cover [12]. This observation directly motivates the controlled laboratory methodology adopted in the present investigation, which seeks to eliminate such confounding factors.

1.2.3 The Role of Particle Mixing State: Coated and Internally Mixed Black Carbon

A significant refinement in understanding black carbon (BC)–snow interactions concerns the mixing state of BC particles, specifically whether BC exists in isolation (external mixing) or encapsulated within shells of sulfate or organic carbon (internal mixing, or a core-shell structure).Pu et al [13]. addressed this complexity using Mie theory in combination with the SNICAR radiative transfer model, and found that the BC coating effect enhances snow albedo reduction by a factor of 1.1 to 1.8 for a non-absorbing shell and 1.1 to 1.3 for an absorbing shell, depending on BC concentration, snow grain radius, and the core-to-shell ratio [13]. This enhancement arises because internal mixing amplifies the effective absorption cross-section of the BC core through an optical lensing mechanism.

The spectral character of this effect is also important: the impact of coating on snow albedo is most pronounced at wavelengths below 1200 nm, and higher BC concentrations or larger core-to-shell ratios produce correspondingly greater differences between coated and uncoated particles [13]. At the regional scale, Pu et al. found that the contribution of the BC coating effect to snow light absorption exceeded that of mineral dust over northern China, based on a comprehensive set of in situ Northern Hemisphere measurements [13]. For the present thesis, this body of work highlights that particle preparation and deposition methodology, including whether particles are deposited dry or in suspension, can meaningfully influence the optical behavior of BC within the ice matrix, a variable that must be carefully controlled and documented.

1.2.4 Variability with Ice and Snow Type

The response of ice and snow to BC contamination is not uniform but depends critically on the physical characteristics of the substrate. Marks and King [14] investigated this variability systematically using radiative transfer modelling calibrated against Arctic field data, calculating albedo responses for both bare and snow-covered sea ice under a range of BC loadings. A key finding is that first-year sea ice is more sensitive to additional BC than multi-year sea ice [14], a difference explained by the greater porosity and lower intrinsic scattering of first-year ice, which offers less compensation for the absorptive effect of impurities.

Snow cover further modulates the BC response: dry snow provides greater mitigation of BC-induced albedo reduction than wet snow, because dry snow is a more efficient scattering medium per unit depth [14]. These findings are directly relevant to the present thesis, which treats ice structure and environmental conditions as experimental variables, and they underscore the necessity of characterizing and controlling substrate properties carefully in any comparative laboratory investigation. They also suggest that experimental results obtained under one set of ice conditions may not be directly transferable to others, reinforcing the importance of systematic parametric variation.

1.2.5 Measurement Techniques, Modelling Frameworks, and Uncertainties

A broader synthesis of measurement and modelling approaches is provided by Qian et al. [15], whose review encompasses Arctic, Tibetan Plateau, and mid-latitude regions and evaluates a wide range of field techniques for quantifying light-absorbing particles in snow and ice (LAPSI). The review identifies LAPSI as one of the major forcings affecting climate change, as recognized in the IPCC Fourth and Fifth Assessment Reports, while noting that the uncertainty level in

quantifying this effect remains very high [15]. Sources of uncertainty include differences in the amount and spatial distribution of BC, variations in particle size and mixing state, and limitations in the measurement techniques themselves [15].

One mechanism highlighted by Qian et al. of particular relevance to melt dynamics is post-depositional enrichment: as snowmelt progresses, meltwater percolates downward while scavenging BC particles, concentrating them progressively near the surface and thereby amplifying the albedo-reduction feedback over time [15]. Progress in modelling mass concentrations, albedo reduction, radiative forcing, and both climatic and hydrological impacts at global and regional scales is documented, alongside a set of priority research needs for reducing remaining uncertainties [15]. These persistent knowledge gaps in the field literature reinforce the value of the controlled laboratory approach taken in this thesis.

1.3 Research Gap & Motivation

Despite extensive research on polar ice melting, albedo reduction, and climate forcing, several critical research gaps remain unaddressed. Most existing studies on ice–contaminant interactions rely heavily on field observations and large-scale climate models, which, while valuable, do not allow for precise control over individual variables such as particle concentration, deposition method, and ice microstructure. As a result, the isolated effects of specific anthropogenic contaminants on ice reflectivity and heat absorption remain poorly quantified.

In particular, existing literature on soot (black carbon) deposition on snow and ice has primarily focused on atmospheric transport, radiative forcing estimates, and large-scale climatic impacts. However, there is a lack of comprehensive controlled laboratory studies that directly compare soot with emerging engineered nanomaterials such as carbon nanotubes (CNTs) under identical thermal

and environmental conditions. The role of CNTs in cryospheric environments remains largely unexplored, despite their strong light absorption and high thermal conductivity, which may significantly influence heat transfer processes in ice.

Additionally, there is limited understanding of how contaminant characteristics such as particle morphology, size distribution, and surface area influence radiative absorption and melt dynamics when deposited on ice. The combined effects of surface deposition, embedded contamination, and layered contaminant structures across ice depth have not been systematically investigated. Furthermore, the influence of ice structural variations (e.g., clear ice versus porous or crushed ice), thermocouple placement, and internal temperature gradients on observed melting behavior remain underexplored.

Another key gap lies in the separation of radiative, conductive, and convective heat transfer contributions during melting. Most existing studies treat ice melting as a bulk energy balance problem, without resolving localized thermal gradients or coupling between airflow, radiation, and contaminant-enhanced absorption. This limits the ability to fully understand the mechanisms driving accelerated melting in contaminated ice systems.

The motivation for this research is to address these knowledge gaps through a systematic experimental and computational investigation of soot and carbon nanotubes on ice reflectivity and heat absorption under controlled laboratory conditions. This work seeks to provide a comprehensive study of:

- The comparative effects of soot and carbon nanotubes on ice albedo reduction and thermal response under identical conditions.

- The influence of contaminant concentration, deposition method (surface, embedded, and layered), and particle distribution on melt dynamics.
- The role of ice structure, porosity, and thermocouple-resolved thermal gradients in governing heat transfer behavior.

By addressing these objectives, this research aims to improve the mechanistic understanding of anthropogenic contaminant–ice interactions and contribute to more accurate representation of particulate-driven albedo changes in polar climate models. Ultimately, the findings are intended to support better predictions of ice–albedo feedback mechanisms and their implications for global climate change.

1.4 Research Objectives and Hypothesis

The primary objective of this research is to experimentally and analytically investigate the impact of anthropogenic carbonaceous contaminants, specifically soot (black carbon) and carbon nanotubes (CNTs), on polar ice reflectivity and heat absorption under controlled laboratory conditions. This study aims to isolate and quantify the individual and combined effects of contaminant type, concentration, and deposition configuration on ice melting behavior and thermal response.

To achieve this goal, the research is structured around the following specific objectives:

- To experimentally quantify the effect of soot and carbon nanotubes on ice surface darkening, heat absorption, and melt rate under identical radiative and environmental conditions.
- To evaluate the influence of contaminant concentration on temperature evolution, thermal gradients, and time-to-melt behavior in ice systems.

- To compare surface-only, embedded (mixed), and layered contaminant deposition methods and determine their respective impacts on heat transfer and melt dynamics.
- To investigate the role of ice structural properties, including clear ice versus porous/crushed ice, on heat penetration depth and melting stability.
- To characterize internal thermal behavior using thermocouple arrays and develop temperature–time profiles across ice depth.

Based on these objectives, the following hypotheses are proposed:

It is hypothesized that both soot and carbon nanotubes will significantly reduce ice reflectivity, leading to increased solar energy absorption and accelerated melting compared to uncontaminated ice. Due to its strong optical absorption, soot is expected to produce rapid surface warming, while carbon nanotubes may exhibit distinct heat transfer behavior due to their high thermal conductivity and nanoscale structure, potentially enhancing subsurface heat distribution.

It is further hypothesized that increasing contaminant concentration will lead to a nonlinear increase in melt rate, with higher loading intensifying radiative absorption and reducing thermal stability of the ice. Surface-deposited contaminants are expected to produce faster initial melting compared to embedded or layered configurations; however, layered structures may generate more sustained and spatially distributed heat absorption over time.

Additionally, porous or crushed ice is expected to exhibit faster melt rates compared to clear ice due to higher surface area and enhanced heat penetration pathways. Collectively, these objectives and hypotheses aim to establish a mechanistic understanding of how anthropogenic particulate matter alters ice thermal behavior, with implications for polar albedo feedback and climate system modeling.

Chapter 2: Theoretical Background

2.1 Thermophysical Properties

Understanding the thermophysical properties of the materials involved in this study is essential for interpreting heat transfer behavior and melting dynamics. The interaction between radiation, contaminants, and ice is strongly influenced by properties such as thermal conductivity, heat capacity, density, and absorptivity. These properties determine how energy is absorbed, stored, and transported within the system.

2.1.1 Thermophysical Properties of Ice

Ice is a crystalline solid with well-characterized thermophysical properties that govern its response to thermal loading. According to The Engineering Toolbox [16]:

- Thermal Conductivity: ~2.2 W/m·K
- Specific Heat Capacity: ~2.1 kJ/kg·K
- Density: ~917 kg/m³
- Latent Heat of Fusion: ~334 kJ/kg

The relatively high thermal conductivity of ice allows heat to be conducted efficiently from the surface into the interior. However, the large latent heat of fusion means that significant energy is required for phase change, which explains the temperature plateau observed during melting. In this study, these properties are critical for understanding how absorbed radiation is redistributed within the ice and how melting progresses over time.

2.1.2 Thermophysical Properties of Snow

Snow can be considered a porous form of ice, consisting of ice grains and trapped air. This structure significantly alters its thermophysical behavior compared to solid ice. According to The Engineering Toolbox [16]:

- Thermal Conductivity: ~0.05-0.5 W/m·K
- Specific Heat Capacity: ~2.0 kJ/kg·K
- Density: ~50-500 kg/m³
- Latent Heat of Fusion: ~334 kJ/kg

The presence of air pockets drastically reduces thermal conductivity, making snow an effective thermal insulator. Additionally, snow exhibits strong scattering of radiation due to its porous structure, which increases optical path length and enhances interaction with contaminants. In the context of this experiment, crushed ice mimics snow-like conditions, leading to more localized heating near the surface compared to solid ice.

2.1.3 Thermophysical Properties of Soot

Soot is a carbonaceous material composed of agglomerated nanoparticles with a fractal-like structure. Its thermophysical properties make it highly effective at absorbing radiation [10]:

- Thermal Conductivity: 0.1-0.5 W/m.K (structure dependent)
- Specific Heat Capacity: ~0.7-1 kJ/kg·K
- Density: ~1800–2000 kg/m³
- Optical Behavior: Very high absorptivity across UV and visible wavelengths

Soot particles strongly absorb incident radiation and convert it into heat. Due to their morphology, they also enhance multiple scattering and trapping of radiation at the surface. In this study, soot primarily influences surface heating, leading to rapid temperature increases and accelerated melting at the ice surface.

2.1.4 Thermophysical Properties of Carbon Nanotubes

Carbon Nanotubes (CNTs) exhibit unique thermophysical properties due to their nanoscale structure and high aspect ratio [17]:

- Thermal Conductivity: 2000-6000 W/m·K (along tube axis)
- Specific Heat Capacity: ~ 0.7 to 0.9 kJ/kg·K
- Density: 1300–1600 kg/m³
- Optical Behavior: Near-blackbody behavior (UV–visible–IR)

CNTs are highly efficient at absorbing radiation and rapidly conducting heat. Unlike soot, which tends to localize heat at the surface, CNTs can facilitate heat transfer into the surrounding medium due to their high thermal conductivity. This makes them particularly important in understanding subsurface heat redistribution, especially in embedded contaminant configurations.

2.1.5 Comparative Thermophysical Properties: Soot, CNTs, and Engineering Metals

To contextualize the thermal behavior of the contaminants investigated in this study, the table below compares the thermal conductivity, specific heat capacity, and density of soot and CNTs against common engineering metals.

Table 1: Material Properties of Contaminant compared to Metals

Material	Thermal Conductivity (W/m·K)	Specific Heat Capacity (J/kg·K)	Density (kg/m³)
Soot (black carbon) [10]	0.1 – 1.0	710 – 840	1,700 – 1,900
Carbon Nanotubes (axial) [18]	3,000 – 6,600	600 – 750	1,300 – 1,400
Stainless Steel (316) [19]	13 – 16	500	7,900 – 8,000
Aluminum (6061) [19]	150 – 205	897	2,700
Copper [19]	385 – 401	385	8,960

Three observations emerge from this comparison. First, the axial thermal conductivity of CNTs (3,000 to 6,600 W/m·K) substantially exceeds that of copper, placing them among the highest thermally conductive materials known and directly explaining the rapid lateral and downward heat conduction observed in the photothermal melting experiments. Soot, two to three orders of magnitude lower in conductivity, behaves more like an insulating ceramic, retaining absorbed heat locally rather than distributing it efficiently into the ice. Second, both carbonaceous materials have substantially lower densities than any of the metals listed, enabling long-range atmospheric transport to polar regions and making them attractive for weight-sensitive engineering applications. Third, specific heat capacities are broadly comparable across all materials, meaning thermal conductivity is the dominant thermophysical differentiator between soot and CNTs and the primary driver of their divergent photothermal behavior as will be observed in Chapter 5.

2.2 Heat Transfer Mechanisms Present in the Experiment

Understanding the modes of heat transfer is critical for interpreting ice melting and the effect of contaminants in your experiment. In this study, heat transfer occurs primarily via conduction, convection, and radiative absorption.

2.2.1 Conduction

Conduction is the transfer of heat through a material due to a temperature gradient [19]. In the experiment, heat is conducted:

- Within the ice itself
- From the ice to the thermocouple sensors
- Through the PLA container walls

Fourier's Law describes the one-dimensional heat conduction equation [19]:

$$Q_{cond} = -kA\frac{dT}{dx}\ (W) \tag{1}$$

Where the terms in equation one are:
Q_{cond}= heat transfer rate (W)
k= thermal conductivity (W/m·K)
A= cross-sectional area (m^2)
dt/dx= temperature gradient in one direction (K/m)

In the context of this experiment, heat conduction plays a critical role in governing how thermal energy propagates through the ice and surrounding materials. The thermal conductivity of ice determines how quickly heat absorbed at the surface is transferred into the interior, directly influencing internal temperature gradients and the overall melting behavior. The PLA container used in the setup acts as a thermal barrier due to its relatively low thermal conductivity, thereby

minimizing lateral heat loss and ensuring that heat transfer is primarily directed through the ice. Additionally, different ice structures exhibit varying effective thermal conductivities; solid ice allows for more efficient heat transfer, while crushed or porous ice contains air pockets that reduce conductivity and enhance insulating behavior. This difference significantly affects how heat penetrates the ice and contributes to variations in melting dynamics observed during the experiment.

2.2.2 Convection

Convection is the transfer of heat through the movement of a fluid (liquid or gas) driven by temperature-induced density differences [19]. In the experiment, heat is transferred by convection:

- At the ice–air interface
- Within any melted water (liquid phase) surrounding or within the ice
- Between the ice surface and the surrounding air

The rate of convective heat transfer is commonly described by Newton's law of cooling [19]:

$$Q_{conv} = hA(T_s - T_\infty) \quad (2)$$

Where the terms in equation two are:
Q_{conv}= convective heat transfer rate (W)
h= convective heat transfer coefficient (W/m²·K)
A= surface area (m²)
T_s= surface temperature (K)
T_∞= ambient fluid temperature (K)

In the context of this experiment, convection governs how thermal energy is exchanged between the ice and its surrounding environment. When the surface of the ice is exposed to warmer air, heat is transferred via convection, raising the surface temperature and initiating melting. As the ice melts, a thin layer of liquid water forms, and convection within this layer

enhances heat transfer by promoting fluid motion, which redistributes thermal energy more efficiently than conduction alone.

Air movement around the experimental setup plays a significant role in enhancing convective heat transfer. Additionally, the geometry and orientation of the ice and container influence airflow patterns and thus the effectiveness of convective heat exchange. Compared to conduction, convection can significantly increase the rate at which the ice absorbs heat from its surroundings and transitions into the liquid phase.

2.2.3 Radiation Heat Transfer

Radiation is the transfer of heat through electromagnetic waves without the need for a material medium [19]. In the experiment, heat is transferred by radiation:

- From surrounding surfaces and the environment to the ice
- From heat sources to the ice
- Between the ice surface and the inner walls of the PLA container
- From the ice surface to the surrounding environment

The rate of radiative heat transfer is described by the Stefan–Boltzmann law [19]:

$$Q_{\text{rad}} = \varepsilon\sigma A(T_s^4 - T_\infty^4) \quad (3)$$

Where the terms in equation three are:
Q_{rad}= radiative heat transfer rate (W)
ε= emissivity of the surface (dimensionless)
σ= Stefan–Boltzmann constant (5.67×10^{-8} W/m²·K⁴)
A= surface area (m²)
T_s= surface temperature (K)
T_∞= surrounding temperature (K)

In the context of this experiment, radiation contributes to the overall heat exchange between the ice and its environment, particularly when there is a temperature difference between the ice surface and surrounding objects. Even in the absence of direct contact, the ice can absorb or emit thermal radiation, influencing its energy balance.

Radiative heat transfer becomes more significant at higher temperatures, as it depends on the fourth power of temperature, making it sensitive to changes in surface and surrounding temperatures. The emissivity of the ice and the PLA container also affect how effectively each surface emits and absorbs radiation. For example, materials with higher emissivity exchange radiant energy more efficiently, which can increase the rate of heat gain by the ice.

Although radiation is often less dominant than conduction and convection at lower temperature ranges, it still plays a measurable role in the melting process, especially when external heat sources or warm surroundings contribute to the system's energy input.

2.3 Interaction Between Contaminants and Ice surface

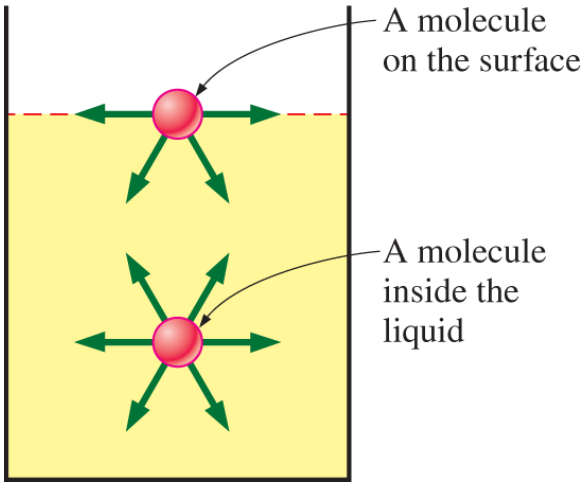

Figure 1:Attractive forces acting on a liquid molecule at the surface and deep inside the liquid. [20]

Understanding the contact angle and microscopic interactions between the contaminants and the ice is essential for analyzing how these particles adhere to and influence the surface. These interactions play a critical role in determining how contaminants are distributed on or within the ice, which in turn affects radiative absorption, heat transfer, and overall albedo. The wetting behavior, governed by contact angle, along with intermolecular forces and surface roughness, influences whether particles remain on the surface, become partially embedded, or redistribute during melting. These mechanisms are important for interpreting the experimental results presented in later chapters and for making informed assumptions about the thermal and optical behavior of contaminated ice.

2.4 Surface Absorptance, Albedo Reduction, and Net Radiative Heat Flux

When infrared radiation from the lamp is incident on the ice surface, the fraction of that energy absorbed depends critically on the optical properties of the surface. For clean ice, the surface albedo which is defined as the ratio of reflected to incident irradiance, is high across much of the solar and near-infrared spectrum, meaning the majority of incident radiation is reflected rather than absorbed [21]:

$$\alpha = \frac{G_{reflected}}{G_{incident}} \tag{4}$$

Where the terms in equation four are:

α is albedo (dimensionless, $0 \leq \alpha \leq 1$),

$G_{reflected}$ is the reflected irradiance (W/m²),

$G_{incident}$ is the total incident irradiance (W/m²).

Pure ice and snow can have albedo values between 0.5 and 0.9 depending on grain size and surface condition [22]. This high reflectivity explains why uncontaminated ice absorbs relatively little of

the incident lamp radiation, and why the pure-ice control experiments in Chapter 5 exhibit long baseline melt times before TC4 responds.

When a carbonaceous contaminant such as soot or carbon nanotubes is deposited on the ice surface, the effective surface albedo drops dramatically. Both soot and CNT are strong broadband absorbers across the infrared spectrum, with absorptance values approaching [10]. The deposited particle layer intercepts the incident irradiance before it reaches the ice, converting electromagnetic energy into thermal energy directly at the surface. The net radiative heat flux absorbed by the contaminated surface can be expressed as [21]:

$$q''_{abs} = (1 - \alpha_c) \cdot G_{incident} \quad (5)$$

Where: $q''_{abs}$is the net absorbed heat flux (W/m²) and $\alpha_c$is the effective albedo of the contaminated surface, which is substantially lower than that of clean ice. The reduction in albedo $\Delta\alpha = \alpha_{ice} - \alpha_c$represents the additional radiative energy intercepted by the contaminant layer and converted to heat, driving the accelerated TC4 temperature rises observed experimentally.

The total radiative energy balance at the contaminated ice surface combines this absorbed flux with re-emission losses and can be written as [19]:

$$q''_{net} = q''_{abs} - q''_{emitted} = (1 - \alpha_c)G_{incident} - \varepsilon\sigma T_s^4 \quad 6$$

Where the terms in equation six are:
ε is the surface emissivity,
σ is the Stefan–Boltzmann constant (5.67×10^{-8} W/m²·K⁴),
and T_s is the surface temperature (K)

Most surface temperatures recorded in the experiments were typically below 25 °C, the re-emission term $\varepsilon\sigma T_s^4$is small relative to the absorbed flux, meaning the net heat gain at the surface is dominated by the absorptance of the contaminant layer.

The effectiveness of a given contaminant as a photothermal agent therefore depends on two material properties: its absorptance across the lamp's emission spectrum, and its thermal coupling to the underlying ice. Soot particles are composed of disordered graphitic carbon and exhibit near-unity absorptance across infrared wavelengths, making them highly efficient converters of incident radiation to heat [10]. Carbon nanotubes similarly possess exceptionally high infrared absorptance due to their one-dimensional electronic structure and large surface area per unit mass [23].

Chapter 3: Materials Characterization of Soot and Carbon Nanotubes (SEM & Physical Properties)

3.1 Introduction

Understanding the physical and morphological characteristics of contaminants is essential for interpreting their influence on radiative absorption and heat transfer in ice. In this study, detailed material characterization was conducted to analyze the structure, distribution, and surface features of soot and carbon nanotubes (CNTs), which are expected to play a significant role in modifying ice reflectivity and thermal behavior.

To achieve a comprehensive characterization across multiple length scales, two complementary imaging techniques were employed. A light microscope (Keyence VHX-7000 ultramicroscopy system) was used to visualize particle distribution and coverage at the macroscale, allowing for observation of dispersion patterns and surface uniformity. In parallel, a Thermo Fisher Scientific (TFS) Quattro Scanning Electron Microscope (SEM) was utilized to obtain high-resolution images of particle morphology, surface texture, and micro-scale interactions between particles. The SEM imaging enabled detailed examination of the structural differences between soot and CNTs, including shape, aggregation behavior, and surface complexity.

This chapter presents the methodology used for sample preparation and imaging, followed by a detailed analysis of the morphological characteristics of both soot and carbon nanotubes. Key properties such as particle size distribution, surface area implications, and structural features are discussed in relation to their expected impact on radiative absorption and heat transfer mechanisms. By establishing a clear understanding of these material properties, this chapter

provides a critical foundation for interpreting the experimental results presented in subsequent chapters.

3.2 Sample Preparation and Imaging Methodology

Figure 2: Sample preparation process

Proper sample preparation is critical to ensure reliable imaging and accurate interpretation of particle morphology and distribution. In this study, soot and carbon nanotube (CNT) samples were prepared in the University of Oklahoma combustion laboratory using a controlled and repeatable protocol designed to minimize agglomeration and ensure uniform dispersion prior to imaging.

Three different masses of each contaminant—5 mg, 15 mg, and 25 mg—were measured using a Veritas ES422 analytical balance (±0.01 g precision), which is suitable for laboratory-scale measurements requiring high accuracy [24]. These mass ranges were intentionally selected to represent varying particle loadings, enabling qualitative assessment of concentration-dependent dispersion behavior and morphological features at the microscale.

Each measured sample was transferred into a 30 mL glass vial, after which 15 mL of deionized (DI) water was added using a syringe. The use of DI water ensured minimal interference from dissolved impurities during imaging. The vials were then sealed and placed in a Branson

CPX2800H Digital Heated Ultrasonic Cleaner for approximately 20 minutes. Ultrasonic agitation promotes particle dispersion by breaking up agglomerates through cavitation effects, a widely used technique for preparing nanoparticle suspensions [25]. This step was particularly important for CNT samples, which are prone to bundling due to strong van der Waals interactions. The resulting soot and carbon nano tubes are respectively shown in figure 1 and figure 2 below.

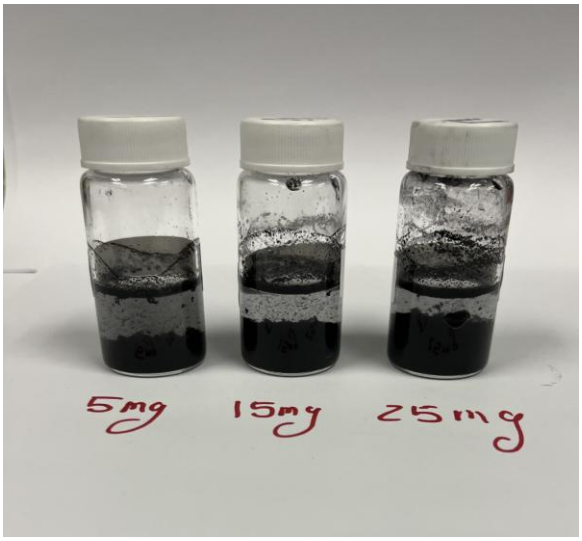

Figure 3: Solution of Soot Shown at Different Weight

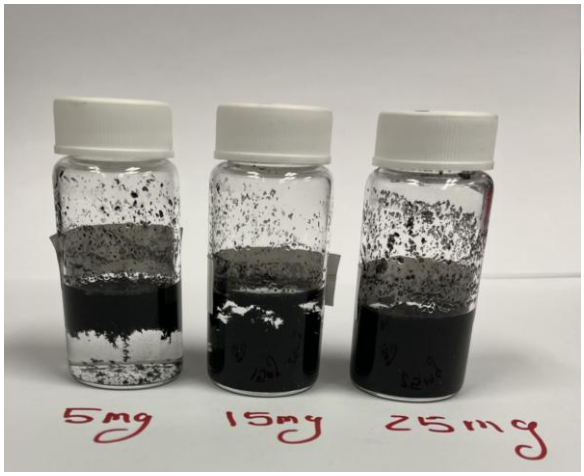

Figure 4: Solution of CNT Shown at Different Weight

Following sonication, the suspensions were allowed to rest briefly to reduce bubble formation. A micropipette was then used to extract a small droplet (on the order of a few microliters) from each

suspension. The droplet was carefully deposited onto pre-marked aluminum disk to ensure consistent sample positioning and traceability between different concentrations and materials. The aluminum substrates provided a conductive surface suitable for electron microscopy imaging.

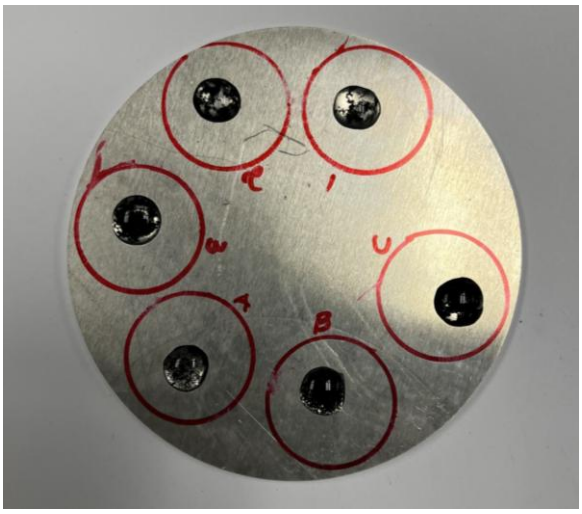

Figure 5: Aluminum disk with deposited contaminant suspension droplets. Labelled regions correspond to material type and mass loading as detailed in Table 1

Table 2: Label key identifying contaminant suspension droplets deposited on the aluminum disk shown in Figure 5, organized by material type and mass loading

Label	Material
A	Soot 5mg
B	Soot 15mg
C	Soot 25mg
1	CNT 5mg
2	CNT 15mg
3	CNT 25mg

The samples deposited were placed in a sealed breaker and allowed to dry under ambient conditions for approximately one week to ensure complete solvent evaporation. Slow drying minimized particle redistribution and clustering effects that can occur with rapid evaporation [26]. In some cases, mild heating or controlled airflow may be used to accelerate drying; however,

ambient drying was preferred in this study to preserve the natural dispersion patterns of the particles.

Figure 6: Sealed beaker containing deposited contaminant samples during ambient drying

Once fully dried, the samples were imaged using both light microscopy (Keyence VHX-7000) and scanning electron microscopy (TFS Quattro SEM). The combination of these techniques enabled analysis of particle distribution at larger scales as well as detailed characterization of morphology, aggregation, and surface features at the micro- and nanoscale.

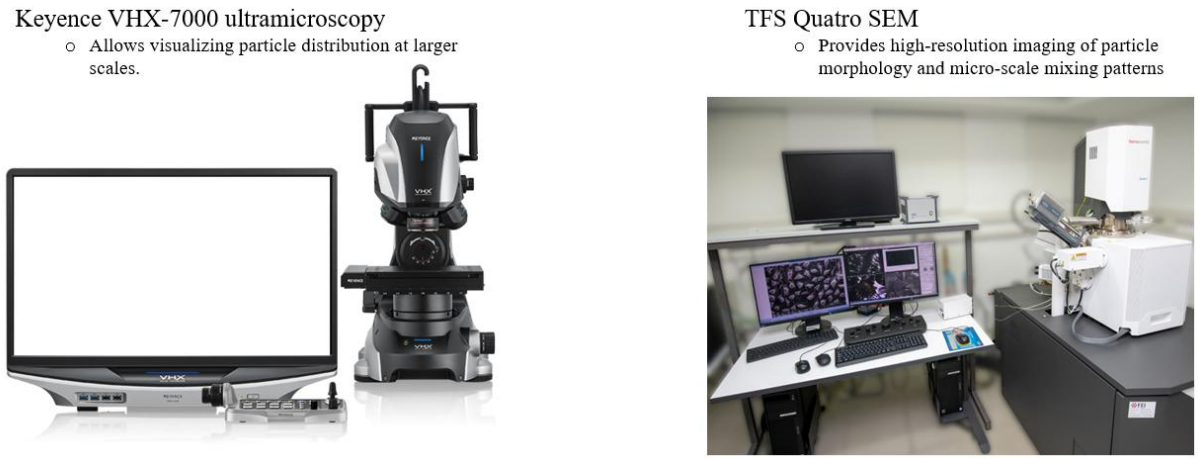

Figure 7: Samuel Roberts Noble Microscopy Laboratory imaging equipment used for sample characterization

This preparation methodology ensured consistent, repeatable samples suitable for comparative analysis of soot and CNT morphology and provided a reliable foundation for subsequent interpretation of their radiative and thermal behavior.

3.3 Morphology and Particle Size Distribution of Soot

The morphological characterization of soot was conducted using both light microscopy (Keyence VHX-7000) and scanning electron microscopy (SEM) to capture structural features across multiple length scales. This multi-scale imaging approach provides insight into both macroscopic distribution patterns and microscopic particle characteristics, which are critical for understanding radiative absorption behavior and heat transfer interactions in contaminated ice systems.

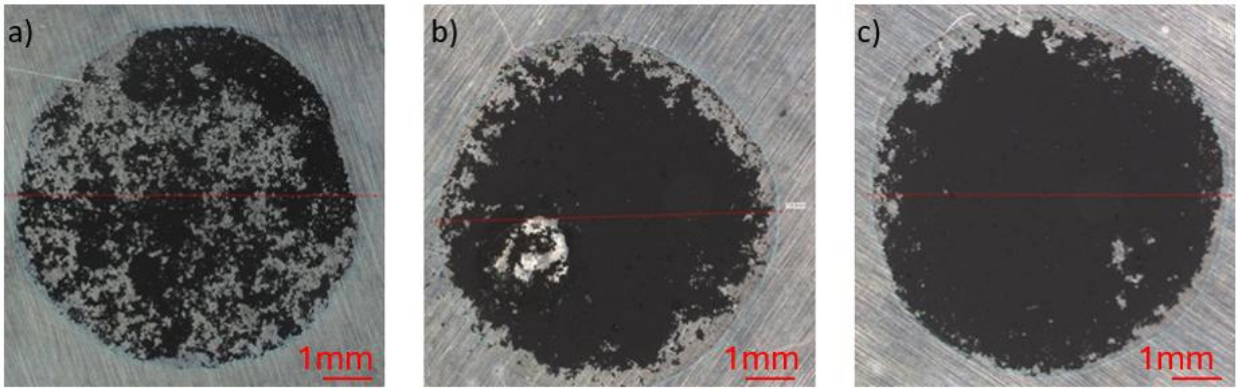

Figure 8: Optical microscopy images of dried soot droplets at ×20 magnification showing (a) 5 mg, (b) 15 mg, and (c) 25 mg deposits

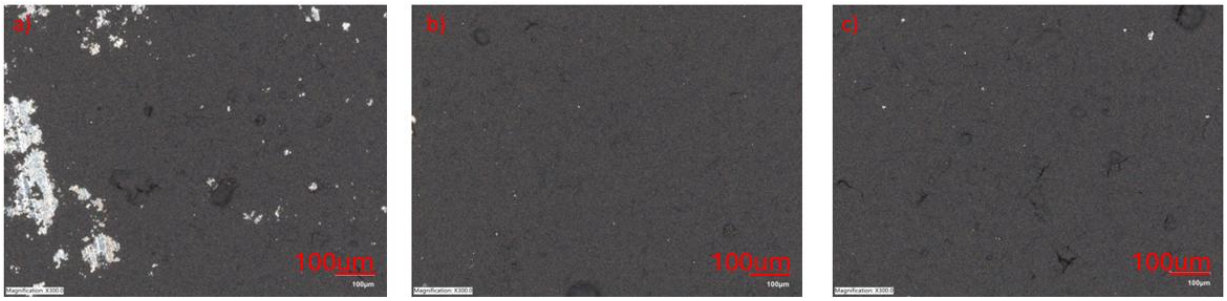

Figure 9: Optical microscopy images of dried soot droplets at ×300 magnification showing (a) 5 mg, (b) 15 mg, and (c) 25 mg deposits

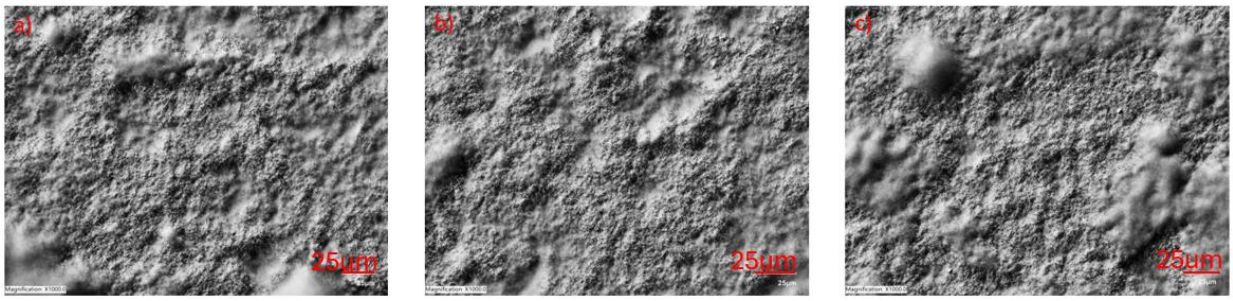

Figure 10:Optical microscopy images of dried soot droplets at ×1000 magnification showing (a) 5 mg, (b) 15 mg, and (c) 25 mg deposit

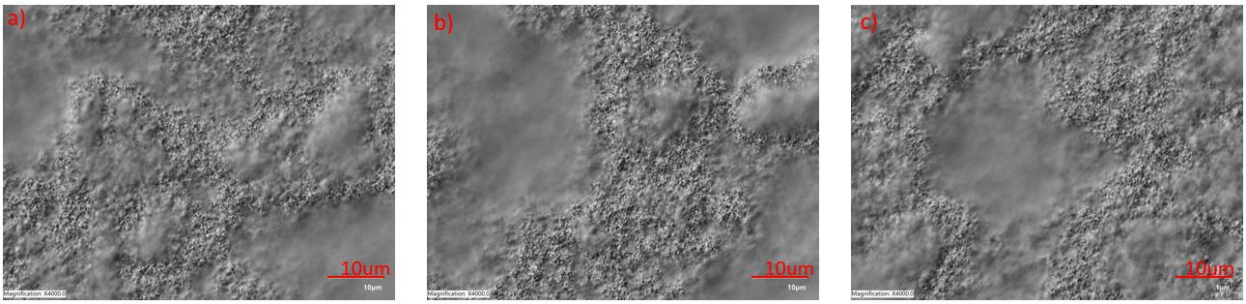

Figure 11: Optical microscopy images of dried soot droplets at ×4000 magnification showing (a) 5 mg, (b) 15 mg, and (c) 25 mg deposits

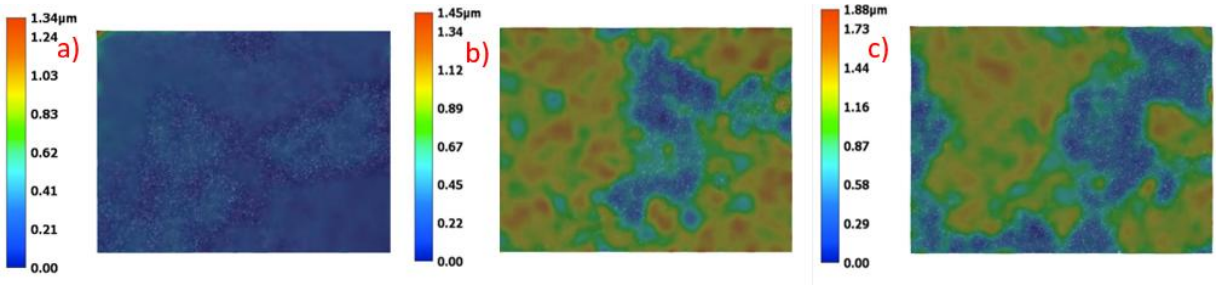

Figure 12: Three-dimensional surface profile images showing deposit depth of dried soot droplets at (a) 5 mg, (b) 15 mg, and (c) 25 mg loadings

Initial observations were performed using the Keyence VHX-7000 ultramicroscope. Images were acquired at magnifications of 20×, 300×, 1000×, and 4000× for each soot concentration (5 mg, 15 mg, and 25 mg). At lower magnifications (20×), the overall spatial distribution of soot on the substrate could be clearly observed. A noticeable increase in surface coverage and apparent density was observed with increasing mass loading. The 5 mg samples exhibited sparse and discontinuous particle coverage, while the 25 mg samples showed significantly denser and more uniform deposition. This trend demonstrates how contaminant concentration directly influences macroscopic surface darkening, which is closely related to albedo reduction.

At intermediate magnifications (1000×), clustering behavior became more apparent. soot particles were observed to form irregular agglomerates, with higher concentrations leading to increased particle overlap and reduced visible substrate areas. These agglomerates are indicative of strong interparticle interactions, which influence how light is absorbed and scattered at the surface.

At the highest magnification (4000×), finer details of the soot distribution were captured, revealing localized regions of dense particle accumulation. Additionally, 3D surface profiling images obtained from the Keyence system provided valuable information on the vertical distribution of the deposited particles. These 3D images highlighted variations in deposit thickness within the

dried droplet ("bubble") region, showing that soot particles tend to accumulate more heavily along certain regions due to evaporation-driven flow (e.g., coffee-ring effects). This non-uniform thickness distribution is important, as it directly affects local heat absorption and can lead to spatially varying melt behavior in ice.

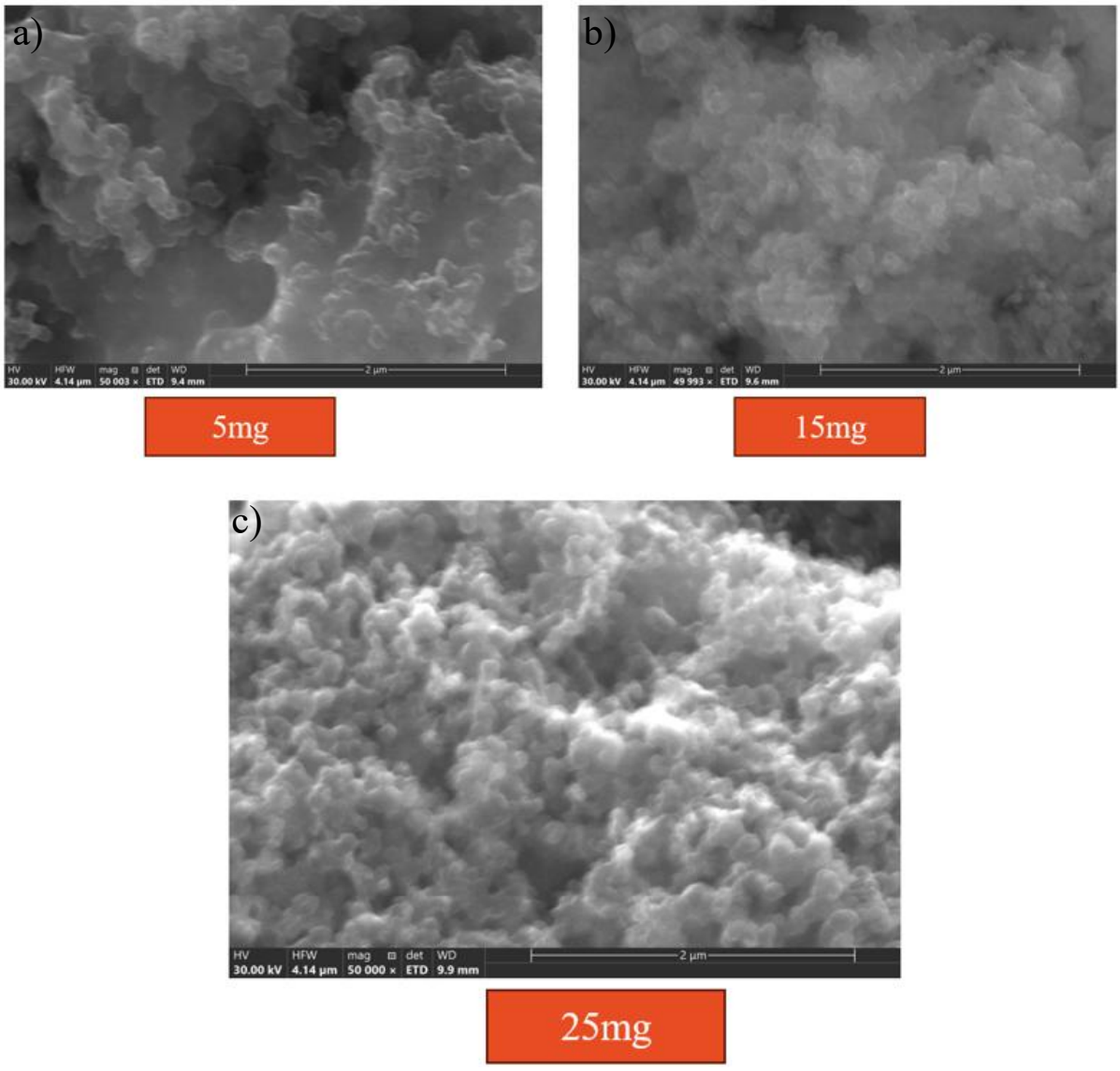

Figure 13: Scanning electron microscopy images of representative soot deposits on the aluminum substrate at (a) 5 mg, (b) 15 mg, and (c) 25 mg loadings

Following light microscopy, high-resolution imaging was conducted using the TFS Quattro SEM to further investigate the microscopic structure of soot particles. SEM images revealed that soot

consists of irregularly shaped, near-spherical primary particles that form complex fractal-like aggregates. These aggregates are characterized by high surface roughness and significant porosity, resulting in a large effective surface area. The nanoscale size of the primary particles, combined with their aggregated structure, enhances their ability to absorb and trap incoming radiation.

This detailed morphological information is critical for understanding the interaction between soot particles and incident radiation from the heat source. The irregular geometry and high surface area of soot aggregates promote multiple scattering and absorption events, leading to efficient conversion of incident UV and visible radiation into thermal energy. Furthermore, the porous structure of soot clusters may facilitate localized heat retention and transfer to the surrounding ice matrix, thereby accelerating melting.

In addition, SEM imaging allows for more accurate estimation of particle size distribution and aggregation scale, which are key parameters in modeling radiative transfer using principles such as the Beer–Lambert law. By understanding the microscopic structure and arrangement of soot particles, it becomes possible to better predict how these contaminants influence light attenuation, energy absorption, and subsequent heat transfer within the ice.

Overall, the combination of light microscopy and SEM provides a comprehensive understanding of soot morphology, from macroscopic distribution patterns to nanoscale particle structure. This multi-scale characterization is essential for linking physical properties of the contaminant to its thermal and radiative behavior in ice, thereby supporting the broader objectives of this study.

3.4 Morphology and Particle Size Distribution of Carbon Nanotubes

The morphological characterization of carbon nanotubes (CNTs) was conducted using both light microscopy (Keyence VHX-7000) and scanning electron microscopy (SEM) to capture their

structure and distribution across multiple length scales. Similar to soot, this combined imaging approach enables a comprehensive understanding of CNT behavior, from macroscale dispersion patterns to nanoscale structural features, which are critical for evaluating their impact on radiative absorption and heat transfer in ice.

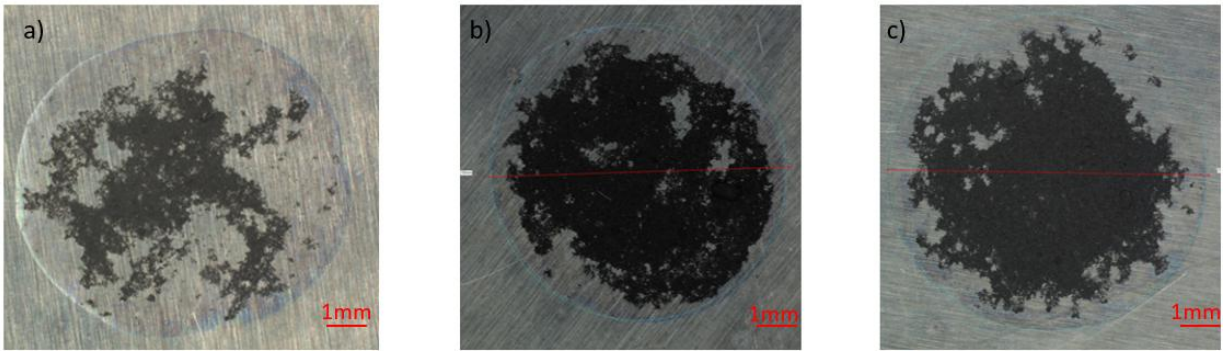

Figure 14: Optical microscopy images of dried CNT droplets at ×20 magnification showing (a) 5 mg, (b) 15 mg, and (c) 25 mg deposits

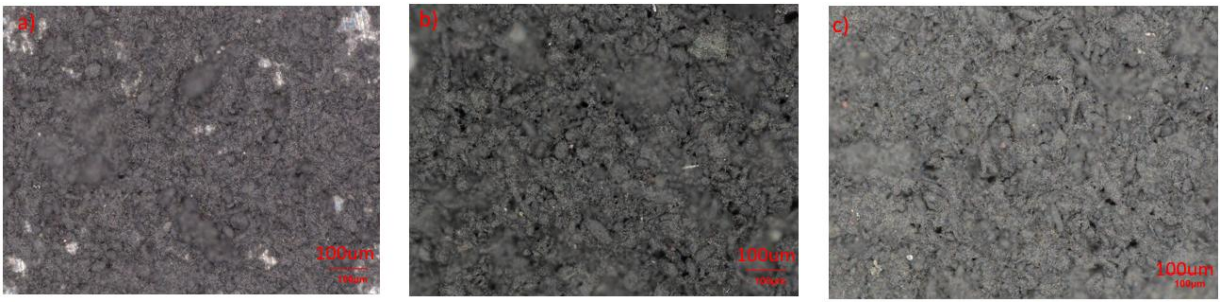

Figure 15: Optical microscopy images of dried CNT droplets at ×300 magnification showing (a) 5 mg, (b) 15 mg, and (c) 25 mg deposits

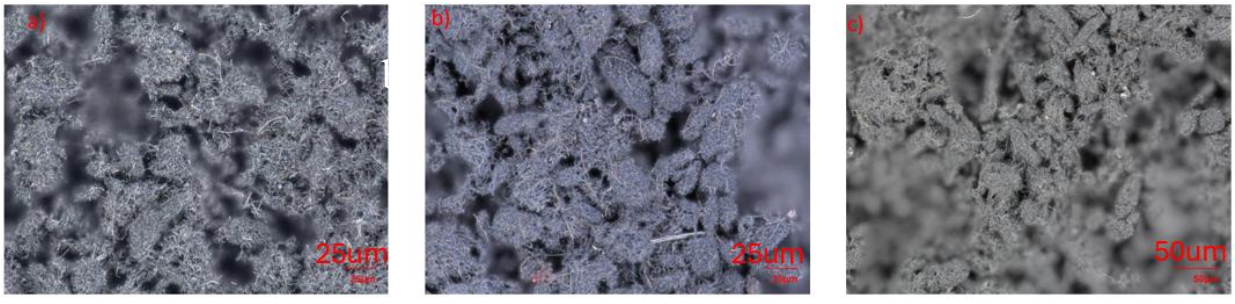

Figure 16: Optical microscopy images of dried CNT droplets at ×1000 magnification showing (a) 5 mg, (b) 15 mg, and (c) 25 mg deposits

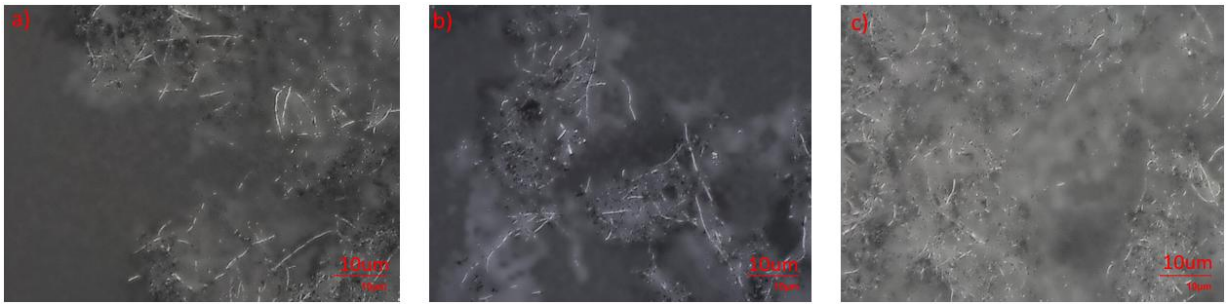

Figure 17:Optical microscopy images of dried CNT droplets at ×4000 magnification showing (a) 5 mg, (b) 15 mg, and (c) 25 mg deposits

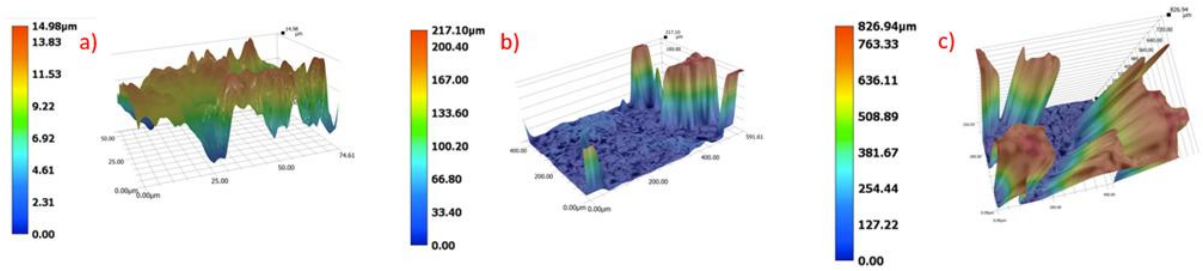

Figure 18:Three-dimensional surface profile images showing deposit depth of dried CNT droplets at (a) 5 mg, (b) 15 mg, and (c) 25 mg loadings

Initial imaging using the Keyence VHX-7000 ultramicroscope was performed at magnifications of 20×, 300×, 1000×, and 4000× for each concentration (5 mg, 15 mg, and 25 mg). At low magnification (20×), CNT deposits appeared less uniformly distributed compared to soot, with visible clustering even at lower concentrations. As mass increased, the surface coverage became denser; however, unlike soot, CNTs tended to form darker, more interconnected regions rather than evenly dispersed layers. This behavior is attributed to the fibrous and entangled nature of CNTs, which promotes network formation rather than discrete particle spreading.

At intermediate magnifications (1000×) the aggregation behavior of CNTs became more pronounced. Instead of forming compact clusters like soot, CNTs appeared as elongated, web-like structures, often bridging across regions of the substrate. These interconnected networks increase in density with higher concentrations, leading to more continuous conductive pathways across the

surface. This structural difference is significant, as it suggests a fundamentally different mechanism of heat distribution compared to soot.

At higher magnification (4000×), the fibrous morphology of CNT bundles became clearer, although individual nanotubes were beyond the resolution of the light microscope. The 3D surface profiling capability of the Keyence system further revealed variations in deposit thickness within the dried droplet region. Similar to soot, CNTs exhibited non-uniform deposition due to evaporation-driven effects; however, the resulting structures showed more pronounced height variations due to the entangled and layered nature of CNT networks. These variations in vertical structure are expected to influence local heat absorption and penetration into the ice.

High-resolution SEM imaging using the TFS Quattro SEM provided detailed insight into the nanoscale morphology of CNTs. The images revealed that CNTs consist of long, cylindrical nanostructures with high aspect ratios, often forming bundles due to strong van der Waals forces. These bundles create a highly porous and interconnected network with significant surface area and structural anisotropy. Compared to soot, CNTs exhibit a more ordered yet entangled morphology, which can facilitate directional heat transfer along the length of the nanotubes.

This nanoscale structure plays a crucial role in how CNTs interact with incident radiation. CNTs are known for their strong broadband absorption, including UV and visible wavelengths, making them highly efficient at converting radiation into thermal energy. Additionally, their high intrinsic thermal conductivity enables rapid heat transfer along the nanotube network, potentially allowing absorbed energy to be distributed more effectively across the ice surface and into subsurface regions.

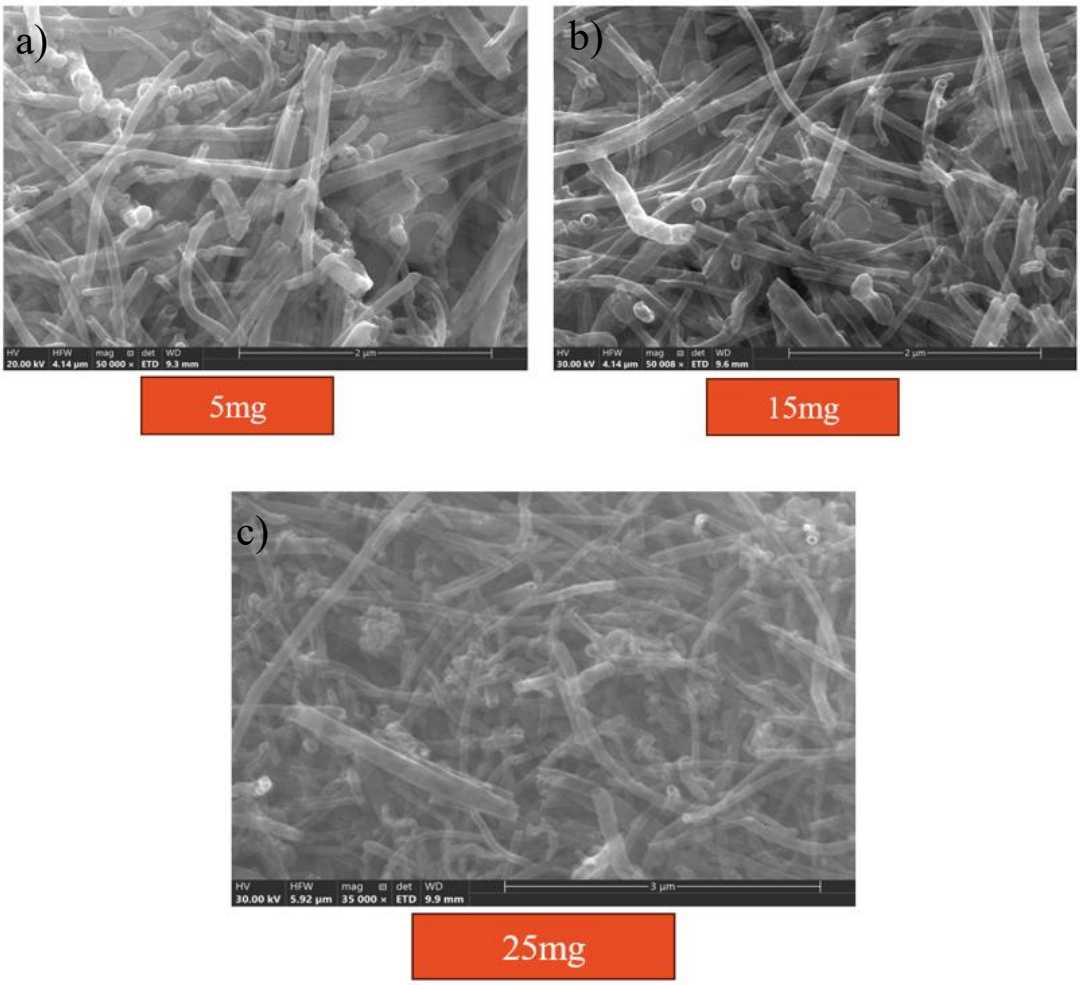

Figure 19: Scanning electron microscopy images of representative carbon nanotube deposits on the aluminum substrate at (a) 5 mg, (b) 15 mg, and (c) 25 mg loadings

The SEM analysis also provides important information regarding bundle size, alignment, and network density, which are key parameters in understanding radiative attenuation and heat transfer behavior. Unlike soot, which primarily enhances localized absorption, CNT networks may promote both absorption and lateral heat spreading, leading to different melting dynamics.

Overall, the combination of light microscopy and SEM imaging highlights the distinct morphological differences between CNTs and soot. While soot forms compact, fractal-like aggregates, CNTs create fibrous, interconnected networks with high aspect ratios and enhanced thermal transport capabilities. This multi-scale characterization provides essential insight into

how CNTs interact with radiation and heat, thereby contributing to a deeper understanding of their role in modifying ice reflectivity and melting behavior

3.5 Chapter Conclusion

This chapter presented a comprehensive multi-scale morphological characterization of soot and carbon nanotubes using light microscopy and scanning electron microscopy, establishing a clear physical basis for interpreting their respective radiative and thermal behaviors in ice. Sample preparation followed a controlled sonication and ambient-drying protocol designed to preserve natural dispersion patterns and ensure reproducibility across the three mass loadings of 5 mg, 15 mg, and 25 mg.

The characterization revealed fundamentally distinct morphologies between the two contaminants. soot was found to consist of near-spherical primary particles forming irregular, fractal-like aggregates with high surface roughness and significant porosity, promoting efficient absorption and localized heat retention within the ice matrix. CNTs, by contrast, exhibited long cylindrical nanostructures with high aspect ratios that form fibrous, entangled networks, a morphology associated with broadband radiation absorption and enhanced lateral heat conduction along the nanotube length. Both materials showed concentration-dependent increases in surface coverage, though their deposition patterns differed markedly, with soot forming compact discrete clusters while CNTs produced interconnected web-like networks.

These structural differences carry direct implications for the heat transfer and melting dynamics investigated in subsequent chapters. The compact, high-surface-area aggregates of soot are expected to promote intense localized heating, whereas the networked architecture of CNTs suggests a capacity for broader heat distribution across and into the ice surface. The morphological

data established here therefore provides an essential interpretive foundation for the experimental results that follow.

Chapter 4: Experimental Design and Methodology

4.1 Introduction

An experiment was designed to investigate the *Impact of Anthropogenic Contaminants on Polar Ice Reflectivity and Heat Absorption* under controlled laboratory conditions. The primary objective of this setup was to replicate, as closely as possible, the physical processes occurring in polar ice environments while maintaining the ability to isolate and systematically vary key parameters. By bridging real-world conditions with controlled experimentation, this study enables a clearer understanding of the mechanisms governing contaminant-induced ice melting.

The experimental design incorporated several critical variables that directly influence heat transfer and melting behavior. These included a controlled radiative heat source to simulate solar irradiation, precise quantities of soot and carbon nanotubes (CNTs) to represent anthropogenic contamination, and different ice structures (crushed versus solid ice) to capture variability in natural ice formations. Additionally, thermocouples were strategically placed at varying vertical heights while maintaining a consistent radial position, allowing for detailed measurement of temperature gradients within the ice. Custom-designed containers were developed to ensure repeatability, geometric consistency, and proper integration of all components within the system.

The selection and control of these variables are essential for isolating cause-and-effect relationships. For example, contaminant concentration directly influences surface albedo and radiative absorption, while ice structure affects thermal conductivity and heat penetration. Similarly, thermocouple placement enables spatial resolution of temperature evolution, providing insight into internal heat transfer mechanisms rather than relying solely on surface observations.

By systematically controlling these parameters, the experiment ensures that observed differences in melting behavior can be attributed to specific physical processes.

A key aspect of this study is its emphasis on reproducibility and data reliability. All experiments were conducted under consistent environmental conditions, with repeated trials performed to validate trends and minimize uncertainty. The use of a standardized setup ensures that comparisons between different test cases, such as soot versus CNTs, or surface versus embedded contamination, are meaningful and scientifically robust.

Data acquisition was performed using a high-speed data acquisition (DAQ) system directly connected to the thermocouples. This system enabled continuous, real-time temperature monitoring throughout each experiment, capturing transient thermal behavior with high temporal resolution. The DAQ system ensures accurate synchronization of temperature data across multiple measurement points, allowing for precise analysis of temperature gradients, heat propagation, and time-to-melt characteristics. This level of detail is critical for developing a comprehensive understanding of coupled heat transfer processes, including radiative absorption, conduction within the ice, and convective effects at the surface.

Overall, the experimental design was developed to balance realism and control to mimic key aspects of polar ice conditions while enabling systematic investigation of individual variables. This approach provides a strong foundation for analyzing how anthropogenic contaminants alter ice reflectivity and heat absorption, ultimately contributing to a deeper understanding of their role in climate-related melting processes.

4.2 Ice Preparation and Thermocouple Placement

This subchapter focuses on the process behind the preparation of the ice for the purpose of the experiment.

4.2.1 3D Printed Containers

In order to ensure accurate and repeatable temperature measurements using thermocouples, a custom, modular ice container was designed and fabricated. The purpose of this container was to provide a controlled and consistent experimental environment while allowing precise placement of sensors and reproducibility across multiple test conditions.

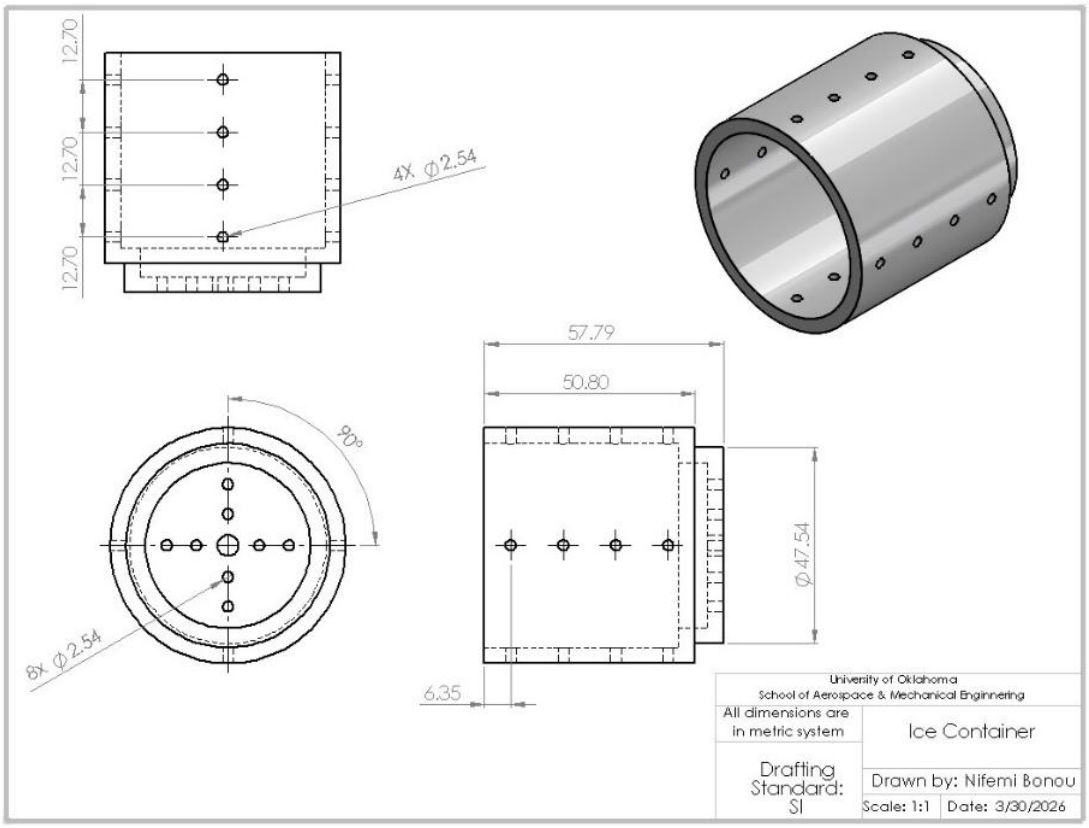

Figure 20: Engineering drawing of Crushed Ice container

The container was manufactured using white polylactic acid (PLA) filament. The choice of white PLA was intentional to minimize any interference with the heat transfer process. White surfaces

are known to reflect a large portion of incident radiation, including visible and infrared wavelengths, thereby reducing unwanted heat absorption by the container itself [27]. This ensures that the primary heat transfer interactions occur between the radiation source, the contaminants, and the ice, rather than being influenced by the container material.

The container geometry was designed using SolidWorks 2025 and fabricated using a Bambu Lab X1-E 3D printer. The design incorporates four vertical through-holes spaced at 0.5-inch intervals along the height of the container. These holes are replicated at 90-degree intervals around the circumference, enabling uniform radial placement of thermocouples. This configuration ensures consistent measurement of temperature gradients at multiple depths within the ice while maintaining symmetry in the experimental setup.

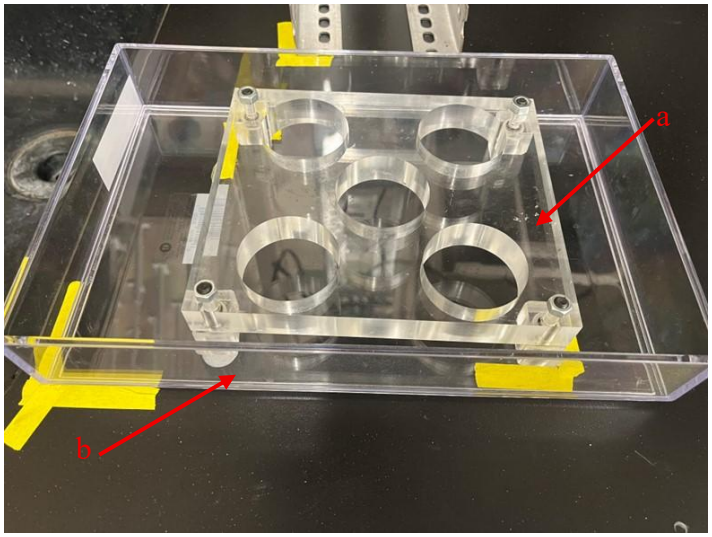

Figure 21: Acrylic base assembly used in the experimental setup, showing (a) the container holder for secure placement of the sample container and (b) the water collection compartment for capturing meltwater generated during ice melting experiments.

The base of the container was designed with a reduced diameter, forming a raised support interface. This feature allows the container to rest securely on a custom-fabricated acrylic platform, produced in the AME machine shop. The use of this raised acrylic stand serves an important thermal purpose: it minimizes conductive heat transfer between the container and the laboratory bench surface.

Since the bench surface is typically dark (black), it can absorb and retain heat, potentially introducing unwanted conduction effects into the system. By elevating the container and using a low-conductivity acrylic interface, these external heat transfer pathways are significantly reduced, ensuring that the measured thermal behavior is primarily driven by the intended experimental variables.

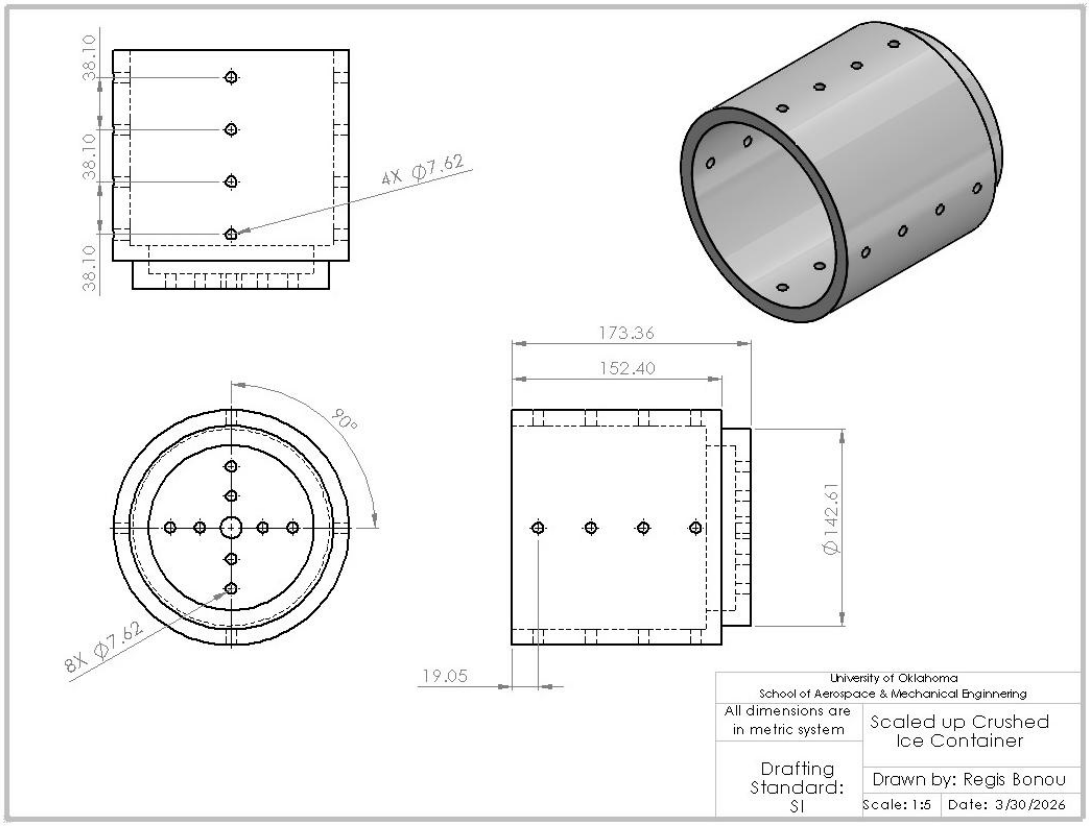

Figure 22:Engineering drawing of Scaled up Crushed Ice Container

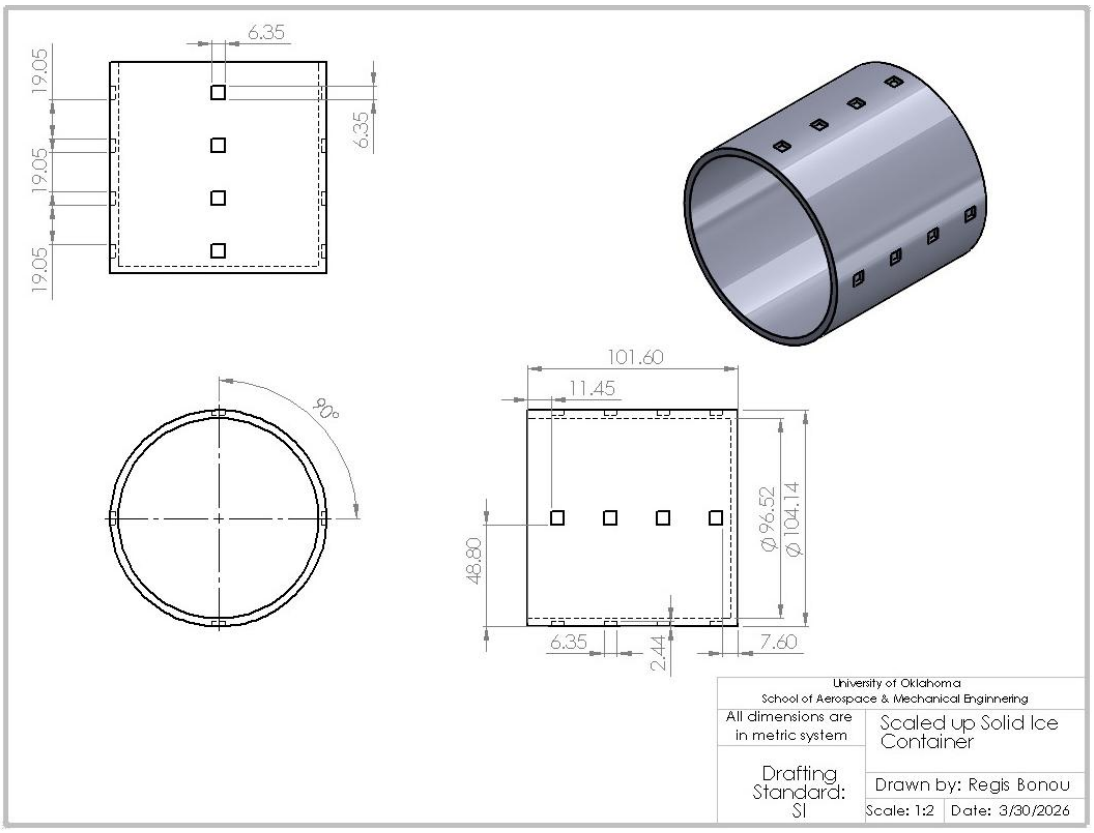

Figure 23: Engineering drawing of Scaled up Solid Ice Container

The primary container was designed to hold crushed ice, simulating the structure of snow-like ice commonly found in polar environments. This allows for the study of porous ice systems and their interaction with contaminants and radiation. To expand the scope of the study, additional container variations were developed. A scaled-up version of the original design was fabricated to investigate how increasing the ice volume and contaminant mass affects the photothermal melting response, while maintaining similar thermal conditions. Furthermore, a separate cylindrical mold was designed for solid ice experiments. This container enabled the formation of uniform ice blocks, after which thermocouple holes were drilled directly into the solid ice. This configuration better represents dense ice structures, such as glacier or iceberg conditions, allowing for comparison between porous and solid ice systems.

Overall, the design and manufacturing of these custom containers were critical to ensuring experimental consistency, minimizing external thermal interference, and enabling precise spatial temperature measurements. This approach allowed for a controlled investigation of heat transfer mechanisms in both snow-like and solid ice conditions.

Figure 24: Picture Showing All Three Containers Used in This Experiment: a refers to Figure 20, b refers to Figure 22 and c refers to Figure 23

4.2.2 Crushed vs Compacted Ice

To investigate the influence of ice structure on heat transfer and melting behavior, two distinct types of ice were used in this study: crushed (snow-like) ice and solid (bulk) ice. The use of these two forms was intentional, as ice structure significantly affects thermophysical properties such as thermal conductivity, porosity, and heat penetration depth, all of which influence melting dynamics [28].

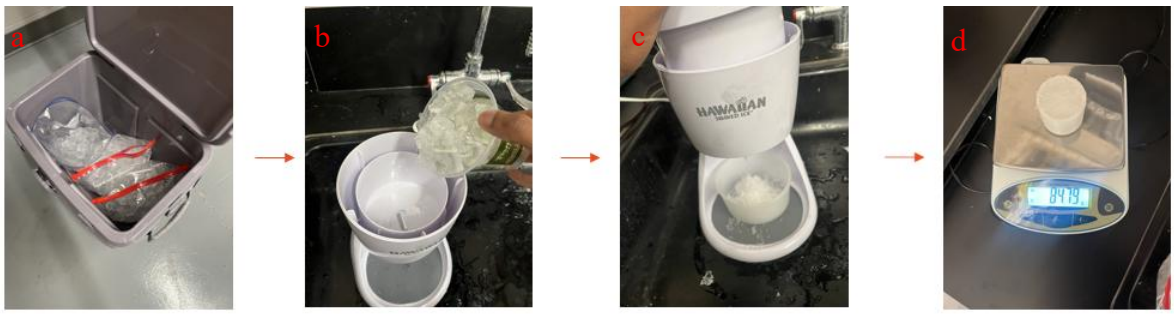

Figure 25: Preparation and processing of crushed ice for experimental use: (a) transport of ice samples from freezer to laboratory within an insulated cooler; (b) placement of ice into the Hawaiian shaved ice machine; (c) the mechanical crushing process; and (d) collection of crushed ice in a container for mass measurement on a digital scale

The first type consisted of crushed ice, obtained from the University machine shop ice maker and subsequently processed using a Hawaiian shaved ice machine to achieve a snow-like structure. This process created a highly porous and loosely packed ice matrix, similar to natural snow found in polar environments. The crushed ice was then placed into the custom 3D-printed container (Figure 20) and carefully measured using a digital scale to ensure consistent mass and packing density across all experiments. The porous nature of this ice type introduces air gaps within the structure, which reduce effective thermal conductivity and alter radiative absorption behavior, making it highly relevant for studying surface-driven melting processes.

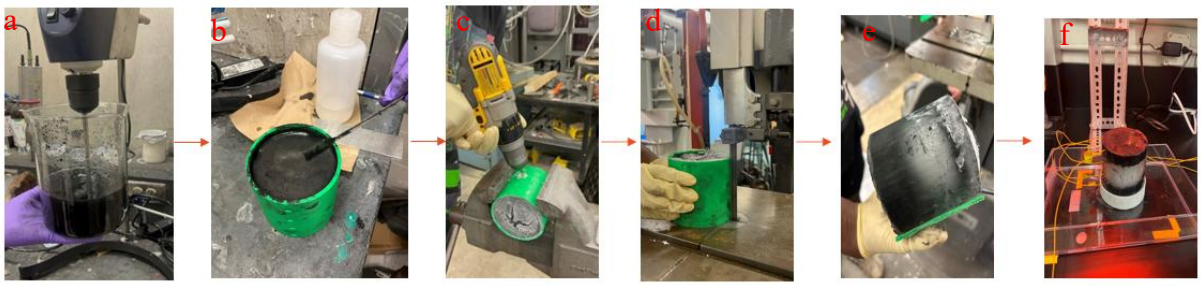

Figure 26: Step-by-step preparation of contaminated ice samples: (a) mixing of water and contaminants using a high-shear laboratory mixer; (b) casting of the mixture into a custom mold for freezing; (c) drilling of the frozen specimen to accommodate thermocouples; (d) removal of the mold casing using a band saw; (e) secondary freezing phase to stabilize the specimen post-machining; and (f) extraction of the final ice sample for experimental testing.

The second type of ice was designed to mimic the structure of dense ice formations such as glaciers or icebergs. In this case, deionized water was poured into the cylindrical container (Figure 23) and

allowed to freeze under controlled conditions for approximately one week to ensure complete solidification. Once frozen, precision-drilled holes were introduced into the ice block to accommodate thermocouples at specified depths. This approach allowed for accurate internal temperature measurements while preserving the integrity of the solid ice structure. After drilling, the container was opened using a saw and exposing the ice cylinder. This cylinder was then put back in the freezer to allow the ice to freeze after the drilling and sawing. Unlike crushed ice, solid ice exhibits significantly higher thermal conductivity and lower porosity, enabling more efficient heat transfer through conduction [28].

The comparison between crushed and solid ice is critical for understanding how structural differences influence heat absorption and melting. Porous ice tends to trap radiation near the surface and exhibit localized heating, while solid ice allows for deeper heat penetration and more uniform temperature distribution. By incorporating both ice types into the experimental design, this study captures a broader range of real-world conditions and provides insight into how anthropogenic contaminants interact with different cryospheric structures.

4.2.3 Thermocouple Placement and temperature measurement

Thermocouples were a critical component of this experimental setup, as they enabled continuous monitoring of the internal temperature of the ice during exposure to the radiative heat source. K-type thermocouples were selected for this study due to their wide operating temperature range, durability, and fast response time, making them well-suited for capturing transient thermal behavior in phase-change systems such as ice melting.

To ensure precision and repeatability, the placement of the thermocouples was integrated directly into the design of the custom 3D-printed container, as described in Section 4.2. This approach

eliminated inconsistencies associated with manual placement and ensured uniform positioning across all experimental runs.

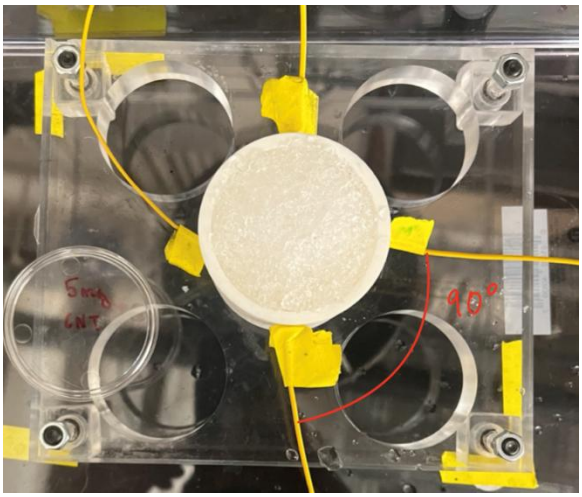

Figure 27: Thermocouple Radial Orientation

The thermocouples were arranged in a full 360° orientation around the container, with insertion points distributed at 90° intervals along the circumference. This configuration ensured that temperature measurements were not influenced by localized variations such as uneven contaminant deposition or directional heating effects. All thermocouples were positioned at a consistent radial distance toward the center of the ice volume, ensuring comparable measurement conditions. To further enforce this consistency, a physical stopper was implemented on each thermocouple by placing tape at a fixed distance of 26.7millimeters from the tip (center of container; see Figure 27). This acted as a positional blocker, preventing the thermocouples from being inserted too far into or pulled out of the container, thereby maintaining a uniform radial length across all measurement points.

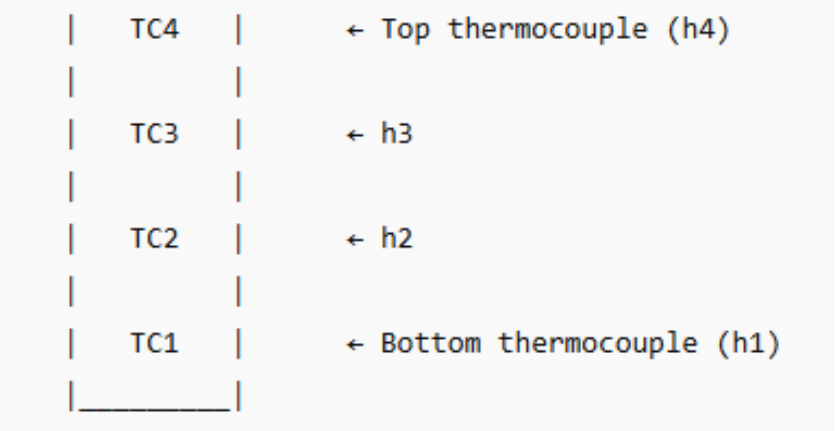

Figure 28: Vertical Thermocouple placement

In addition to radial consistency, the thermocouples were placed at multiple vertical heights within the ice, with uniform spacing between each level. This vertical arrangement allowed for the measurement of temperature gradients from the top surface, where radiative heating is most intense to the lower regions of the ice. As a result, the setup enabled detailed tracking of heat penetration, internal conduction, and melting progression over time.

Temperature data acquisition was performed using a DT9829 data acquisition (DAQ) system, which was directly connected to the thermocouples. The DAQ system was interfaced with a computer running QuickDAQ software, allowing for real-time data logging and visualization. This setup enabled simultaneous monitoring of all thermocouple channels with high temporal resolution, ensuring accurate capture of transient temperature changes throughout each experiment.

The integration of the DAQ system with the thermocouples provided synchronized, high-fidelity temperature measurements across multiple spatial locations. This capability was essential for analyzing temperature evolution, identifying melting onset, and quantifying heat transfer

mechanisms within the ice. Overall, the combination of precise thermocouple placement, controlled insertion depth, and reliable data acquisition ensured a robust and repeatable temperature measurement system, forming the foundation for subsequent thermal analysis in this study.

4.3 Contaminant Deposition Parameters

This section focuses on the preparation, measurement, and deposition of contaminants, as well as the different configurations used to analyze their impact on ice reflectivity and heat absorption. The methodology was designed to ensure consistency, repeatability, and the ability to isolate the effects of contaminant type, concentration, and spatial distribution.

Figure 29: Picture Showing Measurement Of 15mg of CNT

The contaminants (soot and carbon nanotubes) were first measured using the same procedure described in Section 3.2. Three different masses—5 mg, 15 mg, and 25 mg—were weighed using a Veritas ES422 analytical balance (±0.01 g precision) and placed into labeled petri dishes prior

to deposition. The use of petri dishes allowed for controlled handling and uniform transfer of the contaminants onto or into the ice.

Figure 30: Picture Displaying A 3:1 Ratio of Soot to CNT

In addition to single-contaminant cases, mixed contaminant configurations were also prepared to investigate the combined effects of soot and CNTs. Specific mass ratios were created while maintaining a constant total mass. These included 1:1, 2:1, and 3:1 ratio of CNT to soot, as well as the inverse configurations. For example, in a 3:1 soot-to-CNT ratio with a total mass of 25 mg, 18.75 mg of soot and 6.25 mg of CNT were used. This approach ensured that any observed differences in thermal behavior were due to composition rather than total contaminant loading.

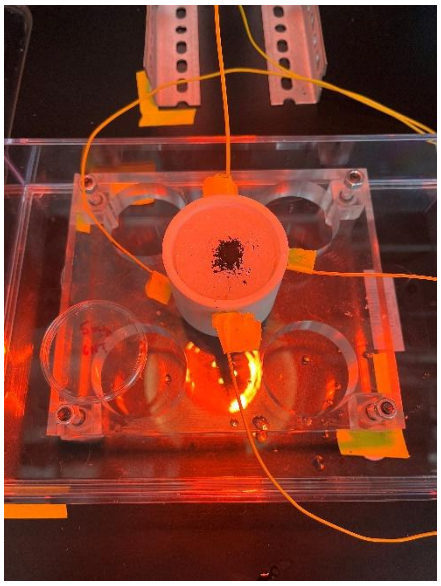

Figure 31: Picture Displaying a Deposit of 5mg of CNT On Top of Ice Surface

The primary focus of this section is the deposition process, which varies depending on the experimental objective. In most experiments, contaminants were deposited directly onto the surface of the ice. This surface deposition method was selected to simulate real-world conditions, where airborne particles settle on ice surfaces and primarily affect albedo and surface-driven heat absorption. The contaminants were carefully distributed across the ice surface to achieve as uniform a layer as possible, allowing for consistent comparison across different concentrations and materials.

In addition to surface deposition, alternative configurations were explored to better understand the role of contaminant location within the ice. In one approach, contaminants were mixed with deionized water and then frozen, resulting in embedded contaminants distributed throughout the ice matrix. This configuration simulates scenarios where particles become incorporated into ice through snowfall or melt–refreeze cycles, allowing investigation of subsurface heat absorption and internal thermal behavior.

A third configuration involved layered deposition, where contaminants were placed at specific vertical intervals corresponding to thermocouple heights within the container. In this setup, contaminants were deposited incrementally at each level during the ice preparation process. This method enabled the study of how contaminant positioning within the ice affects vertical heat transfer, temperature gradients, and melting progression. It also provided insight into how albedo effects evolve when contaminants are not limited to the surface but are distributed throughout the ice depth.

By incorporating surface, embedded, and layered deposition methods, this study captures a wide range of realistic and controlled scenarios. This systematic approach allows for a deeper understanding of how contaminated concentration, composition, and spatial distribution influence radiative absorption and heat transfer mechanisms in ice.

4.4 Environmental Control Parameters

Maintaining consistent and reproducible environmental conditions across all experimental runs was essential to isolating the effects of contaminant type and concentration from extraneous thermal and radiative variables. The following subsections describe the characterization of the radiation source, the method of controlling angle of incidence and the ambient temperature regime, employed throughout the experimental campaign.

4.4.1 Radiation Source Characterization

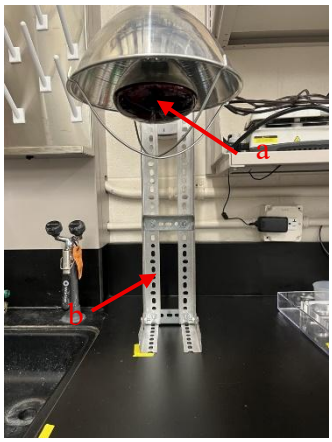

Figure 32: Infrared (IR) heating assembly: (a) the IR lamp utilized as the primary heat source for the experiment; and (b) the adjustable support stand used to control the height and proximity of the lamp to the ice specimen.

The primary heat source used in all experiments was a YU XING Adjustable Brooder Lamp, equipped with a 10.5″ aluminum reflector and bulb guard, rated at 250 V and 660 W [29]. This infrared (IR) heat lamp was selected for its ability to deliver a stable, high-intensity radiative flux over the ice sample surface, replicating the role of solar irradiance as the dominant energy input in polar melting scenarios. The aluminum reflector concentrates and directs the emitted radiation downward toward the sample, improving spatial uniformity of the incident flux and minimizing lateral energy losses. The adjustable mounting allowed the lamp height above the sample surface to be fixed consistently across all trials, ensuring that the irradiance intensity at the sample plane remained constant throughout the experimental series. By operating in the infrared spectrum, the lamp is particularly well-suited to investigating surface heat absorption, as the thermal response of contaminant-laden ice depends directly on the absorption of radiative energy across the infrared and near-infrared wavelength range.

4.4.2 Heat source Placement

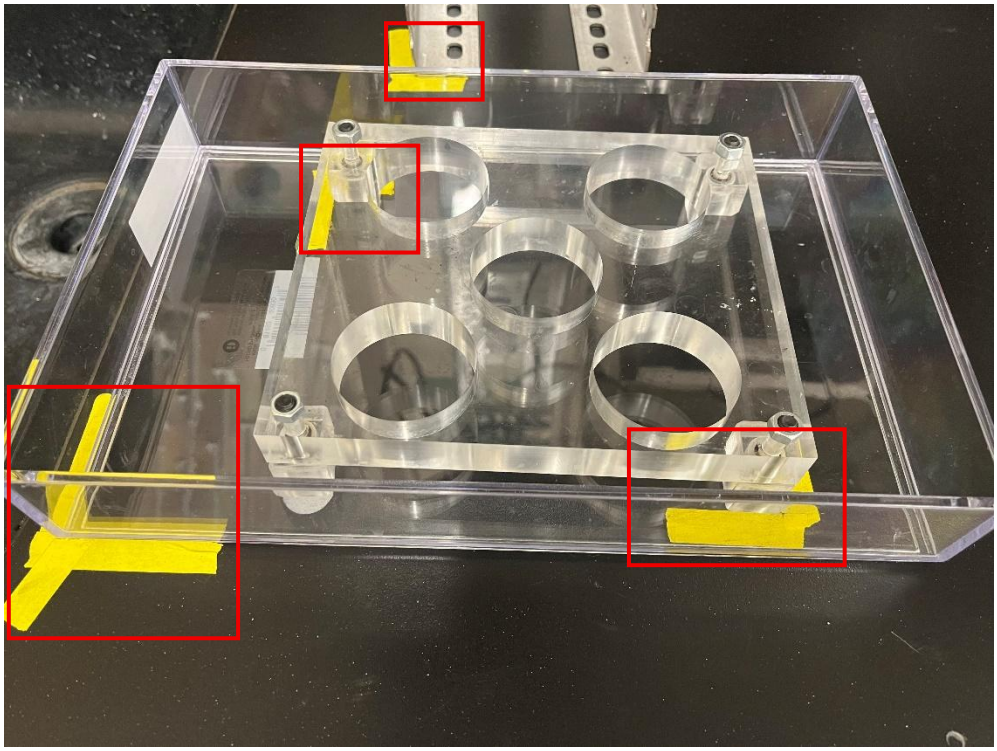

Figure 33: Picture Showing Tape Placement for Angle of Incidence

To ensure that the radiation struck the ice surface perpendicularly and consistently across all experiments, the sample was positioned directly beneath the center of the lamp in a normal-incidence configuration. Precise lateral positioning was achieved using tape markings applied to both the acrylic base supporting the ice sample and the laboratory table surface. These reference marks defined a fixed target location that could be reproduced exactly between trials, eliminating any run-to-run positional drift that might otherwise introduce variability in the effective irradiance received by the sample. Normal incidence was selected because it represents the condition of maximum radiative flux delivery to the horizontal surface, analogous to high solar elevation angles in polar summer, and because it simplifies the interpretation of results by removing the

angular cosine factor from the energy balance. This approach also ensures that comparisons between different contaminant types and concentrations are not confounded by differences in effective illuminated area or path length through the sample.

4.4.3 Ambient Temperature Control

All experiments were conducted in a temperature-controlled laboratory room maintained at a fixed ambient temperature of 18.5 °C. This condition was held constant throughout the experimental campaign to ensure that convective heat exchange between the air and the ice sample remained consistent across trials. A stable ambient temperature is critical in melting experiments of this kind because the rate of convective heat transfer to the ice surface is sensitive to the air-to-surface temperature differential; any drift in room temperature would alter this driving force and introduce systematic error into measured melt rates. By fixing the ambient condition at 18.5 °C, all observed differences in thermal response and melting behavior between sample types can be attributed with confidence to the properties of the deposited contaminants rather than to fluctuations in the surrounding thermal environment.

4.5 Experimental run

The diagram presented in Figure 21 details the data collection process, illustrating the complete sequence of steps from initial thermocouple connection to the DT9829 data acquisition module through to final temperature logging via the QuickDAQ software. It further depicts the physical experimental setup, showing the spatial arrangement of the infrared heat lamp, contaminant layer, instrumented ice sample, and acrylic base, alongside the signal pathway through which thermocouple measurements are transmitted to the computer for continuous recording throughout each 30-minute run.

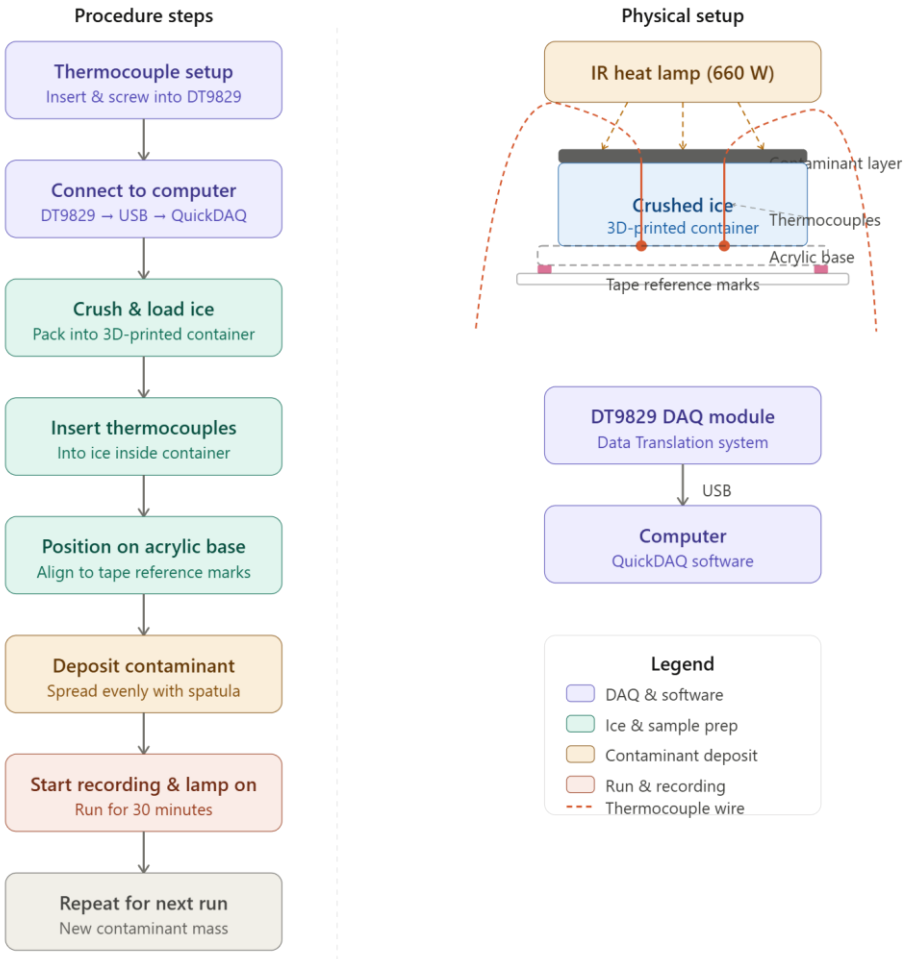

Figure 34: Diagram Detailing the Experimental Set Up

4.5.1 Data Acquisition System Setup

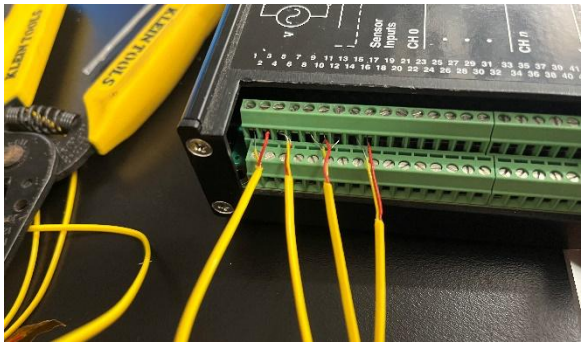

Figure 35: Connection Between Thermocouple and DT9829

Prior to each experimental run, the thermal measurement system was assembled and verified. Type-K thermocouples were inserted into the designated ports of the Data Translation DT9829

data acquisition module and secured by tightening the terminal screws to ensure stable electrical contact and minimal measurement noise. The DT9829 module was then connected to the laboratory computer via USB, and the QuickDAQ software was launched to establish communication with the device. Channel assignments, sampling frequency, and logging parameters were configured within QuickDAQ before any ice sample was prepared, ensuring that the data acquisition system was fully operational and recording a stable baseline signal prior to the introduction of the heat source.

4.5.2 Ice Preparation and Sample Loading

Once the data acquisition system was confirmed to be functioning correctly, the ice sample was prepared. The ice was crushed to a consistent particle size distribution and packed into the 3D-printed sample container, ensuring uniform fill height and density across all experimental runs (see Figure 19). The thermocouples were then carefully inserted into the ice within the container at their designated positions, allowing subsurface temperature evolution to be captured throughout the melting process alongside any surface measurements.

The loaded container, with thermocouples in place, was positioned on the acrylic base at the tape-marked reference location established during the angle-of-incidence calibration described in Section 4.4.2. This ensured that the sample was returned to the identical position beneath the lamp for every experimental run, guaranteeing a consistent angle of incidence and irradiance level at the ice surface across all trials.

4.5.3 Contaminant Deposition

With the ice sample correctly positioned, the contaminant was carefully deposited onto the exposed upper surface of the ice. The weighed quantity of contaminants, either soot or carbon

nanotubes, at the prescribed mass for that experimental run was distributed as uniformly as possible across the surface using a laboratory spatula. Care was taken to achieve even spatial coverage, minimizing localized concentration hotspots that could produce non-representative thermal responses (see Figure 24). The deposition step was completed immediately before initiating the run to prevent any pre-exposure to ambient heat or air currents from altering the initial surface condition.

4.5.4 Data Recording and Heat Lamp Activation

Once the contaminant deposition was complete and all components were confirmed to be in their correct positions, data recording was initiated in QuickDAQ. The infrared heat lamp was then switched on, beginning the controlled irradiation of the sample surface. Each experimental run was maintained for a fixed duration of 30 minutes, during which the QuickDAQ software logged thermocouple readings continuously. At the conclusion of each run, the lamp was switched off and the recording was stopped. The container and thermocouples were cleaned, and the procedure was repeated in full for each subsequent experimental condition, with the contaminant mass varied systematically between runs in accordance with the experimental matrix.

4.6 Summary of Experimental Configurations

Table 3 below summarizes all experimental configurations carried out in Chapter 5.

Table 3: Summary of experimental configurations investigated in Chapter 5

Ice type	#	Configuration	Contaminant	Mass loading	Notes	Section
Crushed ice	1	Control	None	—	Pure ice baseline; TC4 onset 27.5 min	§ 5.1.1
	2	Surface deposition	Soot, CNT (separate)	5 mg, 15 mg, 25 mg	Deposit applied uniformly to top ice surface	§ 5.1.2
	3	Layered deposition	Soot, CNT (separate)	5 mg, 25 mg	Contaminant deposited at each TC height, covered with ice	§ 5.1.3
	4	Mixed ratio	Soot + CNT (combined)	25 mg total (5 ratios)	CNT:Soot ratios: 3:1, 2:1, 1:1, 1:2, 1:3	§ 5.1.4
	5	Scaled-up surface	Soot, CNT (separate)	1 g each	~3× volume container; same surface deposition method	§ 5.1.5
Solid ice	6	Control	None	—	Dense frozen block; starts at ~−5 °C; TC4 onset 46.4 min	§ 5.2.1
	7	Surface deposition	Soot, CNT (separate)	1 g each	Same surface method; conductive warming before melt event	§ 5.2.2

4.7 Data Volume and Measurement Uncertainty

All temperature data in this study were recorded at a sampling rate of 240 Hz using a DT9829 data acquisition system connected to four Type-K thermocouples simultaneously. At this rate, each thermocouple channel generates 240 data points per second, meaning that a 30-minute experiment alone yields 432,000 measurements per channel, or 1,728,000 measurements across the four-channel array. Experiment durations in this study ranged from 21.5 minutes (CNT 25 mg surface deposition) to 69.6 minutes (scaled-up control), resulting in per-channel data volumes between 309,600 and 1,002,240 points depending on the configuration. Summing across all 18 experimental runs and all four thermocouple channels, the experiments generated approximately 47.4 million temperature measurements in total.

This data volume has a direct and quantifiable consequence for statistical measurement uncertainty. The standard error of the mean temperature at any point in time is given by:

$$SE = \frac{\sigma}{\sqrt{n}} \tag{7}$$

where σ is the standard deviation of the raw signal and n is the number of data points contributing to the smoothed estimate. Applying a 5-second moving-average window at 240 Hz yields n = 1,200 data points per smoothed value. Taking a conservative noise standard deviation of σ = 0.3 °C, representative of Type-K thermocouple signal noise under the experimental conditions, the standard error on any smoothed temperature reading is:

$$SE = \frac{0.3}{\sqrt{1200}} = \frac{0.3}{34.6} \approx 0.009\ ℃$$

If instead the full per-channel record of a single experiment is considered (n = 432,000 for a 30-minute run), the standard error on the overall mean temperature reduces further to:

$$SE = \frac{0.3}{\sqrt{432{,}000}} = \frac{0.3}{657.3} \approx 0.00046\ ℃$$

In both cases, the statistical uncertainty on the temperature measurements is below 0.01 °C, negligible relative to the thermal departures of interest in this study, which range from 1.7 °C (suppressed experiments) to 25.1 °C (Soot 25 mg peak TC4 temperature). Error bars are therefore not plotted on any temperature profile in Chapter 5, as they would be invisible at the scale of the figures.

The dominant source of measurement uncertainty in this study is not statistical but instrumental. Type-K thermocouples carry a manufacturer-specified accuracy of ±1.1 °C or ±0.4% of the reading, whichever is greater, across the measurement range. This instrument tolerance is fixed and independent of the number of data points collected. However, since the primary metric used for comparison across experiments is the TC4 onset time, defined as the moment TC4 first rises above 1.0 °C above baseline, rather than absolute temperature, the ±1.1 °C instrument tolerance does not threaten the validity of any comparison in this study. The smallest onset time difference reported between two configurations is 1.4 minutes (layered CNT 5 mg vs surface CNT 5 mg), which corresponds to a physically distinct and reproducible difference in surface melting behavior rather than an artefact of instrument noise.

Finally, each experimental configuration was conducted once. The consistency of the surface-localization finding across all 22 configurations, and the agreement between qualitatively similar configurations (for example, both 15 mg cases suppressed and both 25 mg cases active), provides indirect evidence of experimental reproducibility within the scope of this paper.

Chapter 5: Results and Analysis

5.1 Crushed Ice Experiment

This section covers the Result and analysis obtained from experiment with crushed ice. The containers used here are shown in Figure 20and Figure 22.

5.1.1 Control experiment

Before examining the effect of contaminants on ice melting behavior, a control experiment was conducted using pure crushed ice, with no additives or dissolved substances. The purpose of this baseline test was to establish a reference thermal profile against which the contaminated-ice experiments could be directly compared, thereby isolating the influence of the contaminants from the inherent thermal dynamics of the ice itself.

Four Type-K thermocouples (TC1 through TC4) were embedded at increasing heights within the crushed-ice sample. Temperature data were recorded continuously at a sampling rate of 240 Hz using a QuickDAQ data acquisition system, yielding approximately 400,000 data points over the course of the experiment.

Because ice melting in this context is primarily a surface phenomenon with the melt front progressing downward from the exposed top surface, the experiment was deliberately stopped at the moment the ice covering TC4, the highest thermocouple, had fully melted. This criterion ensured that the recorded data captured the complete thermal evolution from the initial frozen state through to the point at which the uppermost measurement location became fully submerged in meltwater, providing a consistent and physically meaningful endpoint for comparison across all experimental runs.

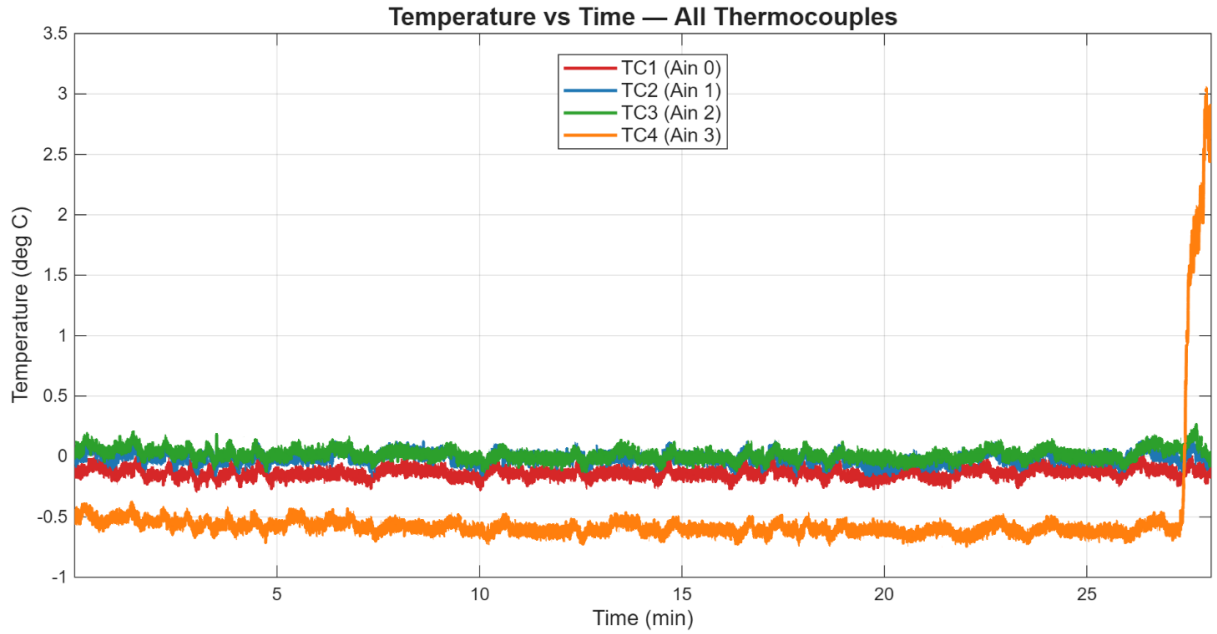

Figure 36: Temperature vs. time recorded at all four thermocouple heights (TC1–TC4) during the pure-ice control experiment. All channels maintain a near-0 °C plateau throughout the ~27-minute test, with a sharp temperature rise at TC4 marking the complete melting

Throughout the experiment, all thermocouples registered temperatures tightly clustered near 0 °C, consistent with the latent-heat plateau characteristic of a melting pure substance. Minor offsets between channels reflect small differences in local thermal contact and the natural temperature gradient within the ice column: TC1 and TC2 remained slightly below 0 °C (approximately −0.2 °C on average), TC3 fluctuated about 0 °C, and TC4 exhibited a consistent negative offset of approximately −0.5 °C, indicating that the higher thermocouple position remained in closer thermal equilibrium with the bulk ice mass for the duration of the test.

The plateau phase lasted approximately 27 minutes, after which a sharp and simultaneous rise in temperature was recorded across all channels, most prominently at TC4, which reached values approaching 3 °C within seconds. This abrupt increase marks the instant at which the last ice layer covering TC4 melted completely, exposing the thermocouple directly to the ambient environment and signaling the defined endpoint of the experiment. The rapidity of this transition underscores

the thermally stable nature of the melting plateau and confirms that the sample remained in a quasi-steady frozen state up until that point.

The control experiment confirms that, in the absence of any contaminants, the pure crushed ice exhibits a well-defined and thermally stable melting behavior dominated by the latent heat of fusion. The near-uniform temperature across all heights during the plateau phase indicates that the thermal gradient within the sample was minimal, and that the thermocouple array successfully captured the bulk thermal state of the ice. These results serve as the reference baseline for evaluating the degree to which dissolved or suspended contaminants alter the melting rate, melt onset temperature, and spatial temperature distribution in subsequent experiments.

5.1.2 Impact of Surface Contaminant

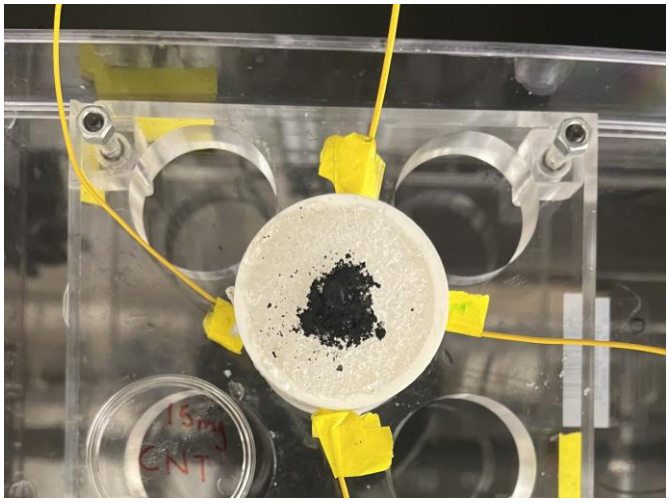

Figure 37:Picture Showing 15mg Of CNT Applied to the Top Surface of Crushed Ice

To investigate the influence of surface-deposited contaminants on the thermal behavior of melting crushed ice, two carbonaceous particles were selected: carbon nanotubes (CNT) and soot. Both materials are known for their strong light-absorbing properties and are relevant to real-world scenarios involving particulate deposition on ice and snow surfaces. Each contaminant was tested

at three mass loadings — 5 mg, 15 mg, and 25 mg — applied uniformly to the top surface of the crushed ice, consistent with the surface-phenomenon framework established in the control experiment

5.1.2.1 Carbon nanotube

CNT 5 mg

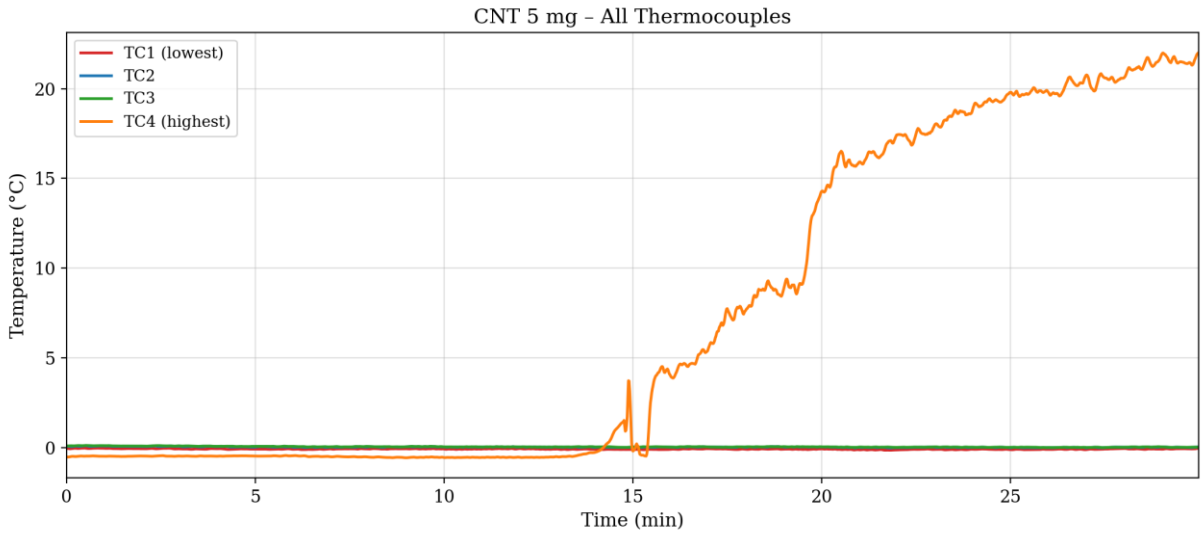

Figure 38:Temperature vs. time at all four thermocouple heights for CNT 5 mg. TC1–TC3 remain near 0 °C throughout, while TC4 rises sharply from approximately t = 14.5 min, indicating accelerated surface melting driven by CNT photothermal absorption

At the lowest CNT loading (5 mg), the three lower thermocouples (TC1–TC3) maintained a stable near-0 °C plateau throughout the 30-minute experiment, with mean temperatures of −0.08, +0.03, and +0.05 °C respectively, virtually indistinguishable from the control. However, TC4 the highest thermocouple, located at the surface recorded a pronounced and sustained temperature rise beginning at approximately 14.5 minutes, ultimately reaching a peak of 22.2 °C. This sharp divergence between TC4 and the lower channels is a direct manifestation of the surface-localized photothermal effect: the CNT layer absorbed incident radiation, rapidly heating the ice surface

while the bulk ice beneath remained at the melting plateau. The experiment confirms that even a small 5 mg CNT deposit is sufficient to significantly accelerate surface melting.

CNT 15 mg

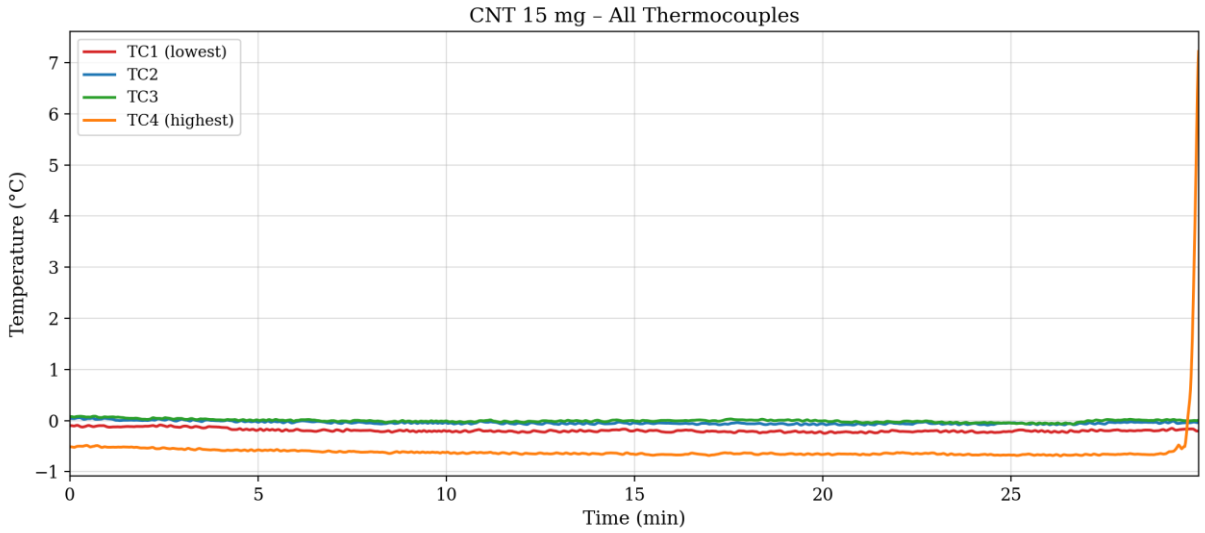

Figure 39:Temperature vs. time at all four thermocouple heights for CNT 15 mg. All channels remain near 0 °C throughout the experiment, with TC4 exhibiting only a marginal rise near the end of the recording period

The 15 mg CNT experiment produced a markedly different result. All four thermocouples maintained near-0 °C temperatures for the full 30-minute recording period, with TC4 recording a mean of −0.59 °C and a maximum of only 8.25 °C reached only at the very end of the test ($t \approx 29.8$ min). This counterintuitive behavior, where a higher mass loading produced less surface heating than the 5 mg case, suggests that at 15 mg the CNT layer may have formed a sufficiently thick, insulating particulate blanket that impeded direct solar coupling or reduced convective heat transfer to the underlying ice. The lower channels (TC1–TC3) showed no departure from the melting plateau, confirming that subsurface conditions remained thermally stable.

CNT 25 mg

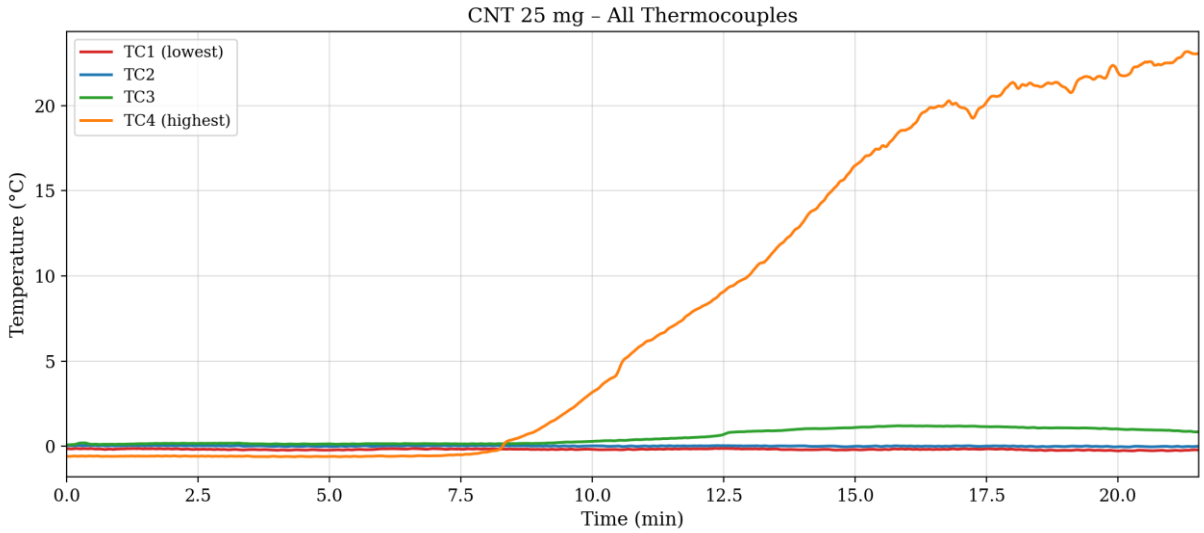

Figure 40: Temperature vs. time at all four thermocouple heights for CNT 25 mg. TC4 begins rising at approximately t = 8.9 min and TC3 also shows a measurable departure from the melting plateau, indicating deeper thermal penetration compared to the lower loading

At the highest CNT loading (25 mg), the experiment exhibited the most rapid surface heating of all CNT trials. TC4 rose above ambient as early as t = 8.9 minutes, peaking at 23.4 °C, and TC3 also departed from the melting plateau (mean +0.57 °C, max 1.35 °C), indicating that thermal penetration extended below the top thermocouple layer. The total experiment duration was 21.5 minutes, the shortest of all CNT runs, consistent with the accelerated melt front driven by the heavier CNT deposit. TC1 and TC2 remained near 0 °C, confirming that the bulk of the ice column was still undergoing latent-heat-dominated melting while the surface had transitioned well above freezing. The 25 mg loading therefore produced the most aggressive surface response, though the non-monotonic behavior across loading levels (5 mg > 15 mg in terms of early TC4 rise) highlights the complex interplay between deposit thickness, optical depth, and surface-energy coupling.

CNT – Average Temperature Comparison

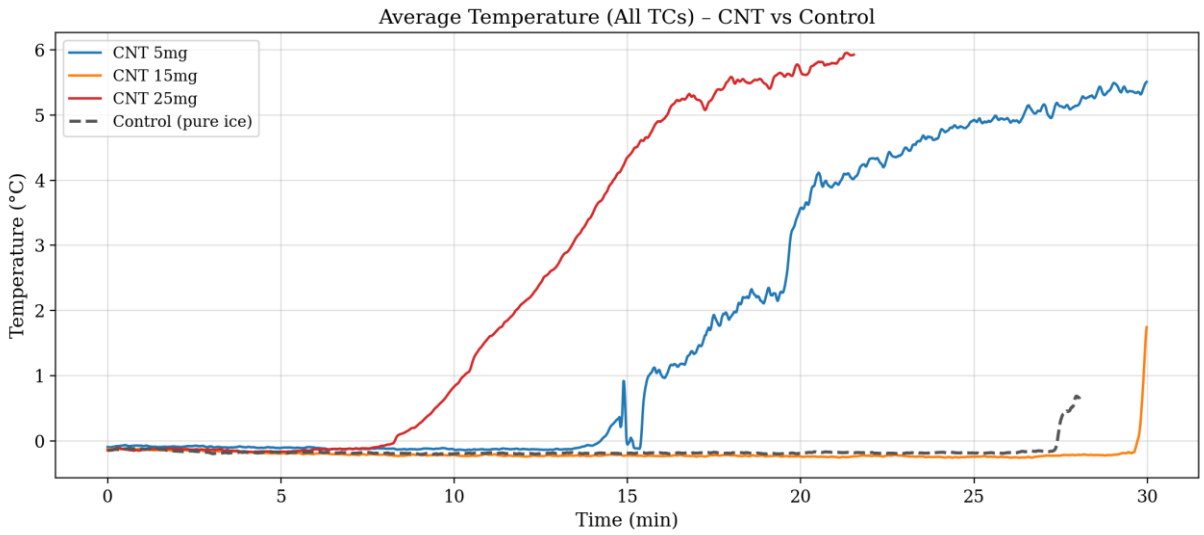

Figure 41:Average temperature of all four thermocouples combined for CNT 5 mg, 15 mg, and 25 mg loadings, compared to the pure-ice control. The 5 mg and 25 mg cases show marked elevation above the control, while 15 mg tracks the control baseline closely

*Figure 41*presents the average temperature of all four thermocouples combined for each CNT loading, alongside the control baseline. The average metric integrates both the stable subsurface channels and the rapidly rising surface channel, providing a single indicator of overall sample heating. The 5 mg and 25 mg curves rise substantially above control, driven primarily by the TC4 response, while the 15 mg curve tracks closely to the control average throughout. This reinforces the non-monotonic loading dependence observed in the individual TC profiles and suggests an optimal CNT coverage thickness for photothermal enhancement.

CNT – Temperature by Thermocouple Height

Figure 42 to *Figure 45* show the temperature evolution at each individual thermocouple height across all three CNT loadings and the control. At TC1 and TC2 (lowest heights), all CNT loading remain indistinguishable from the control, confirming that subsurface ice is unaffected by the surface

contaminant during the plateau phase. At TC3, the 25 mg case shows a slight positive offset, indicating early thermal penetration from the heavily loaded surface. The most dramatic separation occurs at TC4, where the 5 mg and 25 mg curves diverge sharply from the control and 15 mg traces, visually confirming the surface-dominated nature of the photothermal heating mechanism.

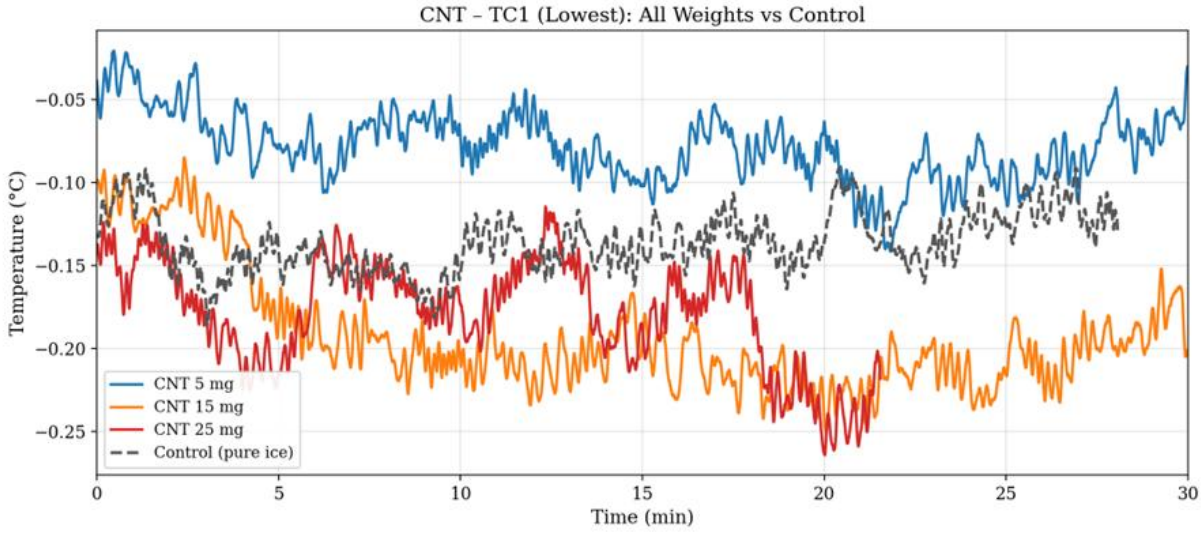

Figure 42: TC1 (lowest height) temperature vs. time for all CNT loadings and the control. All curves remain near 0 °C, confirming no thermal influence of the CNT surface deposit at the lowest measurement point

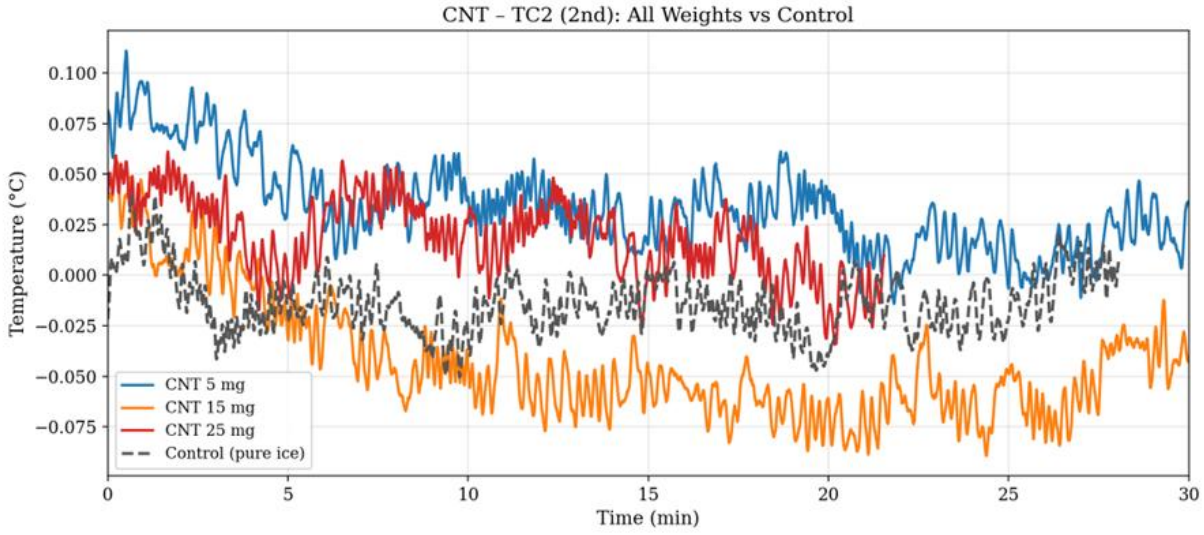

Figure 43: TC2 temperature vs. time for all CNT loadings and the control. As with TC1, no departure from the melting plateau is observed at this height for any loading

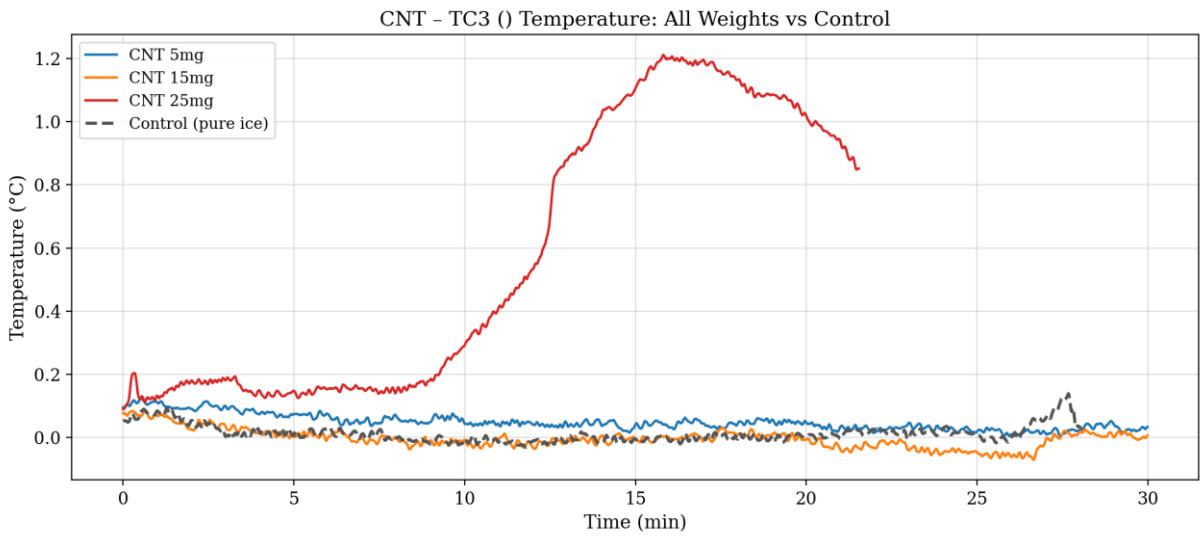

Figure 44: TC3 temperature vs. time for all CNT loadings and the control. A slight positive deviation is visible for the 25 mg loading, suggesting early thermal penetration from the surface layer

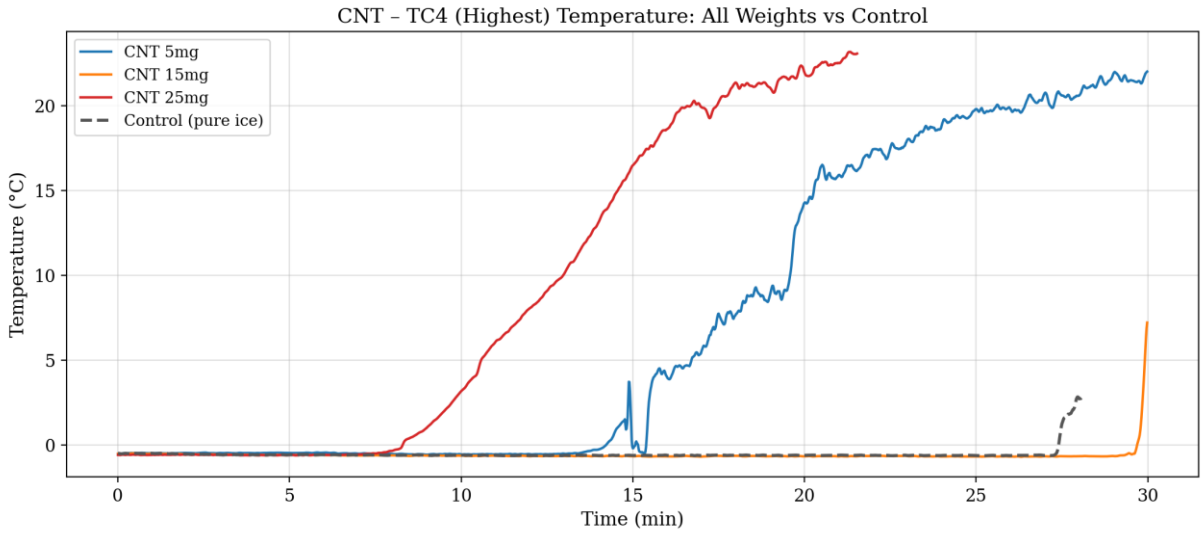

Figure 45: TC4 (highest height, at the ice surface) temperature vs. time for all CNT loadings and the control. The 5 mg and 25 mg loadings produce strong early temperature rises, while 15 mg closely follows the control until near the end of the experiment

5.1.2.2 Soot

Soot 5 mg

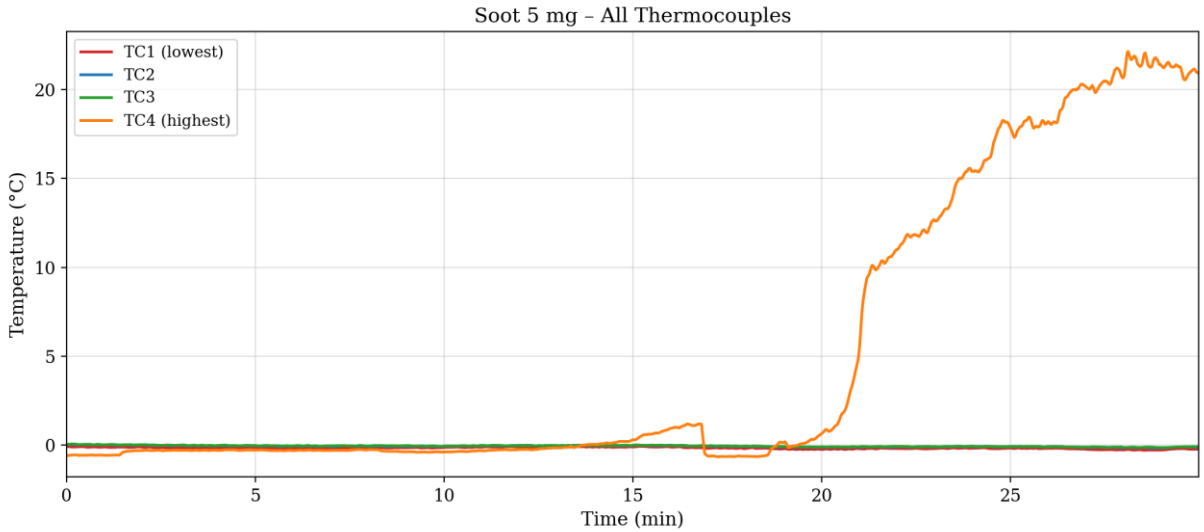

Figure 46: Temperature vs. time at all four thermocouple heights for soot 5 mg. TC1–TC3 maintain the near-0 °C melting plateau while TC4 rises sharply from approximately t = 16 min, consistent with surface-localized photothermal heating by the soot deposit

The 5 mg soot experiment exhibited behavior broadly similar to CNT 5 mg, with TC1–TC3 remaining near 0 °C throughout and TC4 recording a pronounced surface temperature rise. The TC4 ascent began at approximately t = 16.0 minutes, approximately 1.5 minutes later than the equivalent CNT loading, and peaked at 22.5 °C. The mean TC4 temperature of +5.05 °C reflects the sustained high-temperature episode at the surface. The slightly delayed onset relative to CNT 5 mg may reflect differences in particle optical properties, packing, or surface coverage between the two materials at this low loading. Lower channels remained thermally indistinguishable from the control, confirming that the soot-driven heating is equally surface-confined at 5 mg.

Soot 15 mg

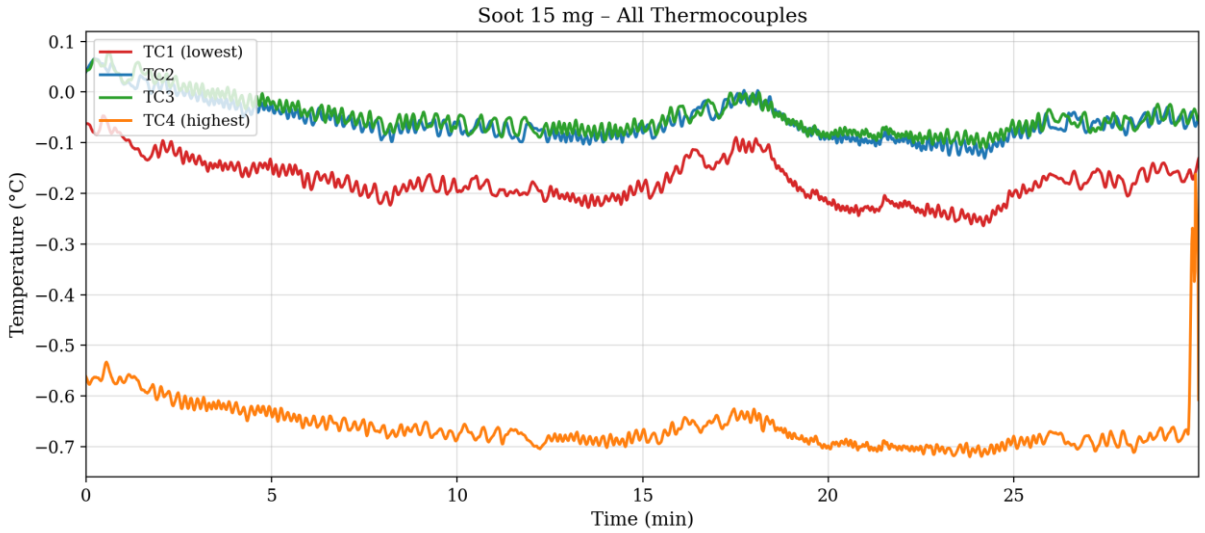

Figure 47:. Temperature vs. time at all four thermocouple heights for soot 15 mg. All thermocouples remain near 0 °C throughout the experiment, with TC4 showing only a minimal temperature rise near the end

The 15 mg soot experiment produced the most thermally stable result of all contaminated runs. All four thermocouples remained at or below 0 °C for the entire 30-minute recording period, with TC4 reaching a maximum of only 1.70 °C near the very end ($t \approx 29.9$ min) and a mean of −0.66 °C. This near-control behavior mirrors that of CNT 15 mg and reinforces the hypothesis that an intermediate contaminant loading (regardless of material) may form a layer that does not efficiently couple incident energy to the ice surface. For soot specifically, this could be attributed to particle agglomeration at 15 mg forming a loosely packed, low-thermal-conductivity deposit that acts as a partial insulator rather than a photothermal absorber.

Soot 25 mg

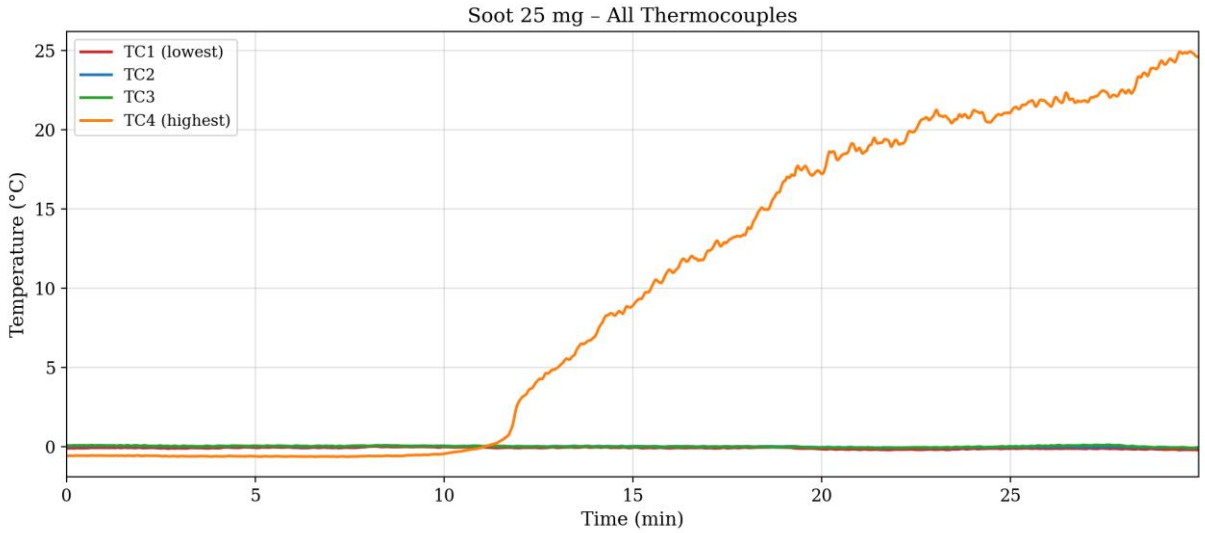

Figure 48:Temperature vs. time at all four thermocouple heights for soot 25 mg. TC4 rises sharply from approximately t = 11.8 min, reaching the highest peak temperature (25.1 °C) recorded across all experiments. TC1–TC3 remain near 0 °C throughout

The 25 mg soot loading produced the most extreme surface response of all experiments, with TC4 recording a mean temperature of +9.76 °C and a peak of 25.1 °C, which was the highest of any single trial. The TC4 rise initiated at approximately t = 11.8 minutes, earlier than soot 5 mg but later than CNT 25 mg, and sustained elevated temperatures for the remainder of the 30-minute test. TC1–TC3 remained at the melting plateau, indicating that despite the extreme TC4 response the photothermal heating remained confined to the surface zone. The high mean TC4 temperature relative to all other experiments indicates that a dense soot deposit at 25 mg maintains efficient solar absorption and heat retention at the surface throughout the melt period.

Soot – Average Temperature Comparison

The average four-TC temperature profiles for all soot loadings are compared against the control baseline in *Figure 49*. The pattern mirrors the CNT results: the 5 mg and 25 mg loadings both produce notable average temperature elevations driven by the TC4 surface response, while the 15 mg loading tracks the control closely. The 25 mg soot average is the highest of all soot cases,

consistent with its dominant TC4 response. The tight grouping of the 15 mg and control curves in both CNT and soot experiments suggests a loading-dependent transition in contaminant behavior that warrants further investigation.

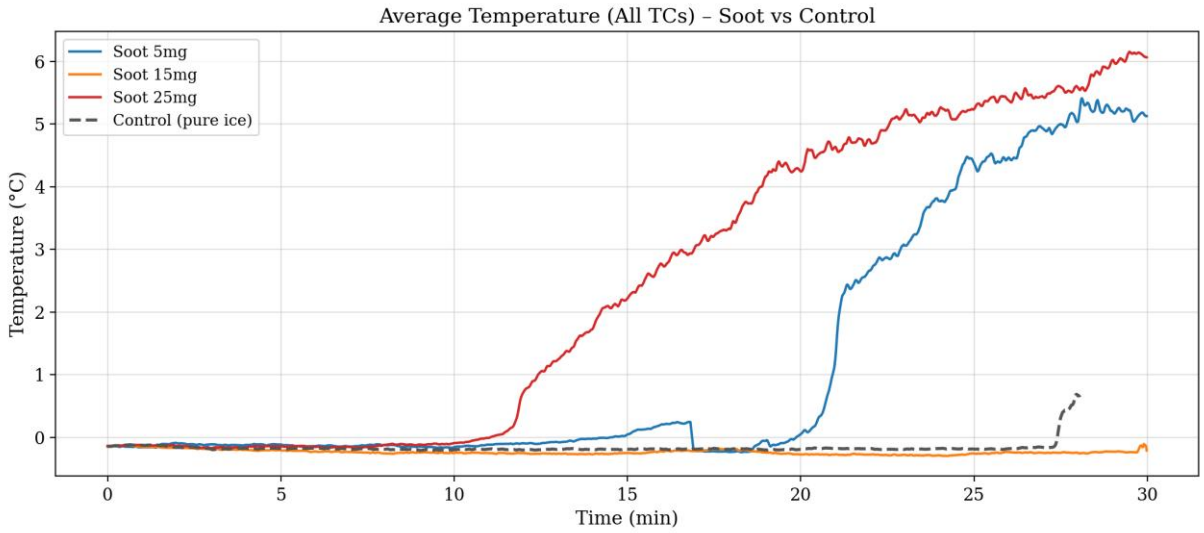

Figure 49:Average temperature of all four thermocouples combined for soot 5 mg, 15 mg, and 25 mg loadings, compared to the pure-ice control. The 5 mg and 25 mg loadings produce elevated averages driven by TC4 surface heating, while 15 mg tracks the control closely

Soot – Temperature by Thermocouple Height

Figures 34 to 37 present the per-height temperature comparison for all soot loadings against the control. The results are structurally analogous to the CNT height analysis: TC1 and TC2 are thermally inert across all loadings, TC3 shows negligible deviation from the control for all soot runs, and TC4 is the primary indicator of surface-driven heating. Notably, the soot 25 mg TC4 profile rises earlier and higher than soot 5 mg, in contrast to the CNT results where 5 mg and 25 mg produced more comparable TC4 responses. This suggests that soot exhibits a more monotonic loading dependence in its photothermal efficiency compared to CNT at these mass scales.

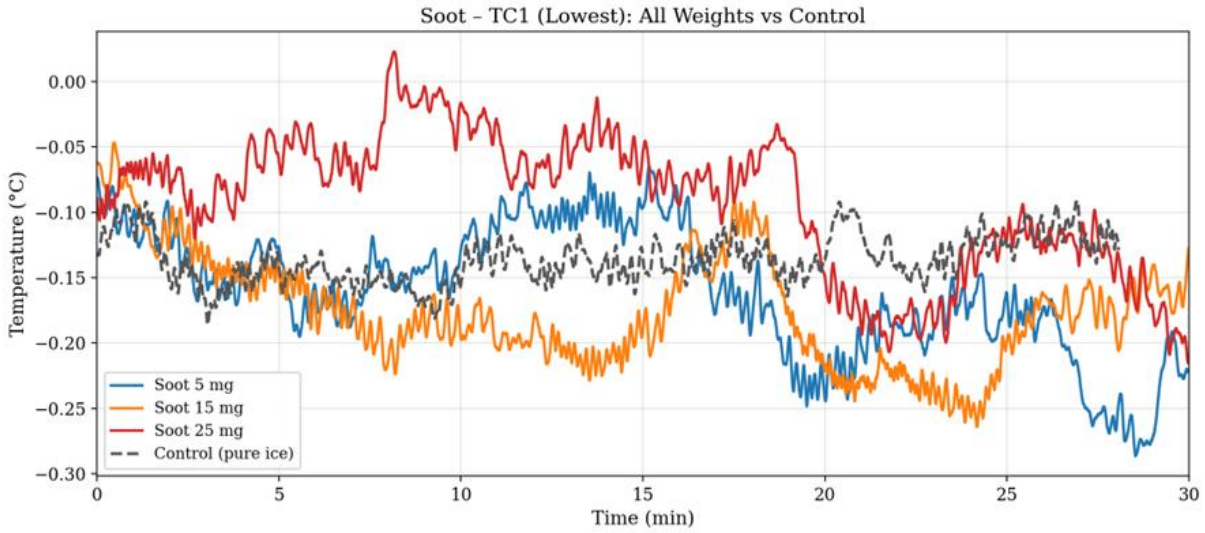

Figure 50:TC1 (lowest height) temperature vs. time for all soot loadings and the control. No thermal deviation is observed at this height for any loading

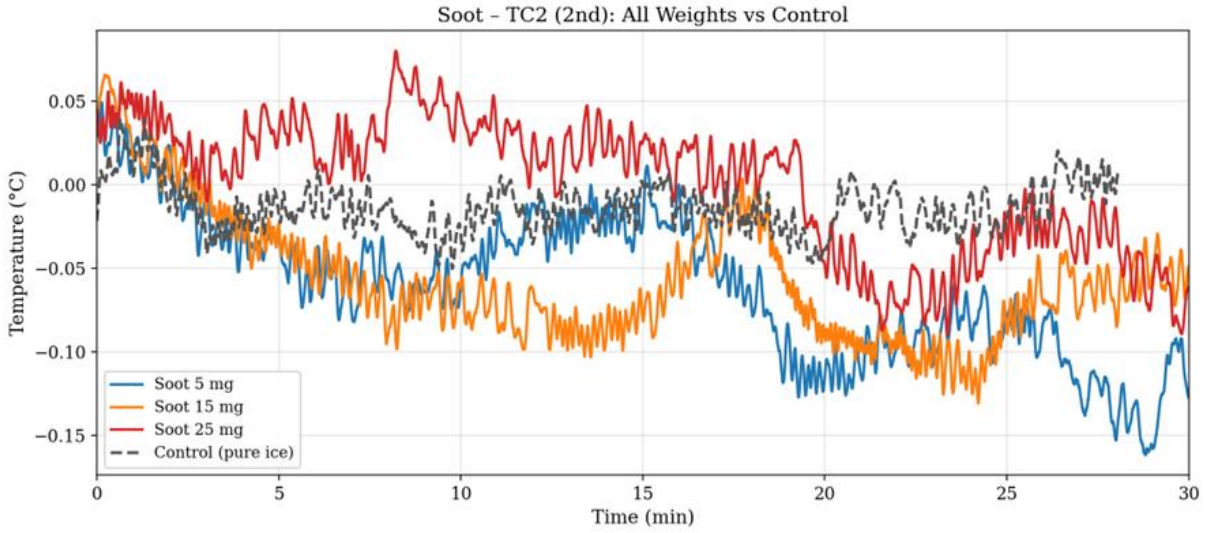

Figure 51: TC2 temperature vs. time for all soot loadings and the control. All curves remain near the 0 °C melting plateau throughout the experiment

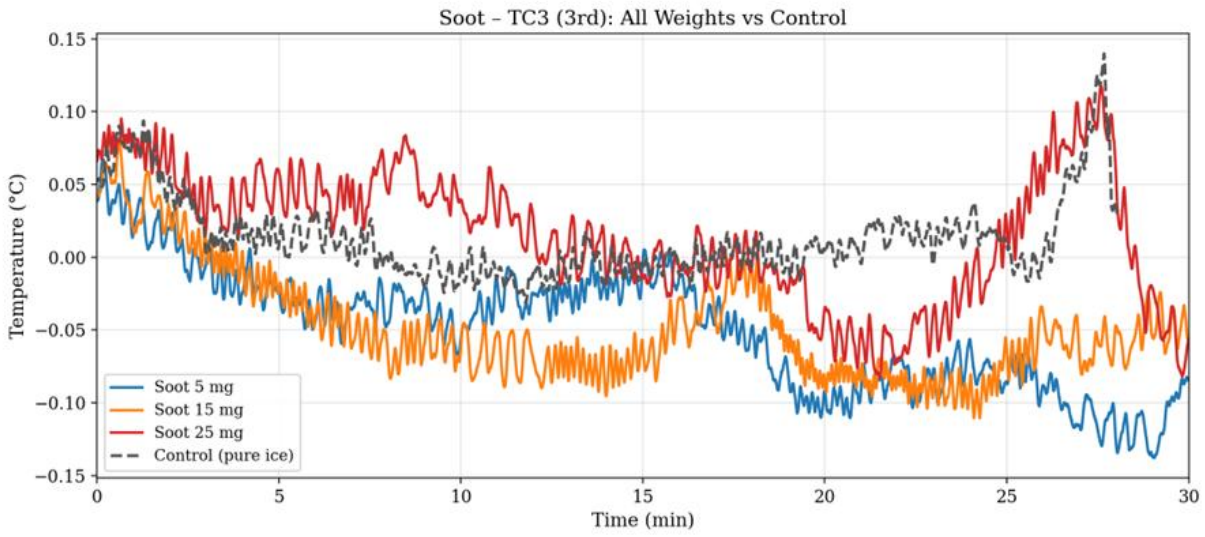

Figure 52: TC3 temperature vs. time for all soot loadings and the control. No significant deviation is observed at this intermediate height for any soot loading

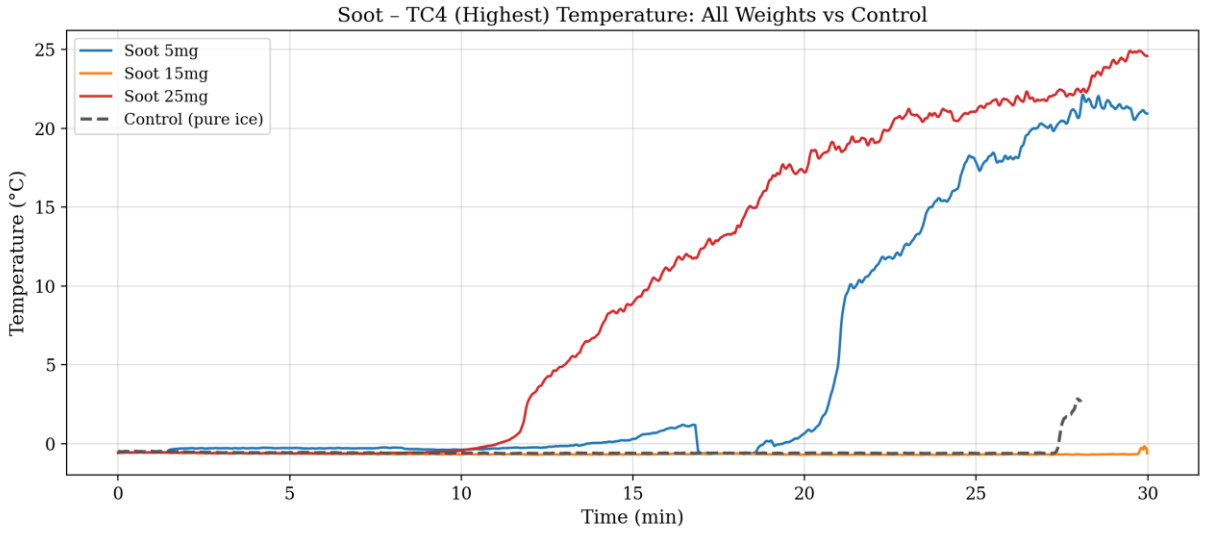

Figure 53: TC4 (highest height, at the ice surface) temperature vs. time for all soot loadings and the control. The 5 mg and 25 mg cases show pronounced surface temperature rises, while 15 mg remains near the control baseline

5.1.2.3 Comparing Control vs CNT vs Soot

This section brings together the CNT and soot results for a direct cross-material comparison at each mass loading and at each thermocouple height, with the pure-ice control as the common

reference. The comparison isolates the influence of material type on photothermal melting behavior while holding loading mass and experimental conditions constant.

Average Temperature: CNT vs Soot vs Control by Loading

Figures 53 to 55 show the combined four-TC average temperature for CNT, soot, and the control at 5 mg, 15 mg, and 25 mg respectively.

At 5 mg (Figure 54), both CNT and soot produce elevated averages relative to the control, with CNT showing a slightly earlier rise onset (14.5 min vs 16.0 min for soot). The similar magnitude of response at this loading suggests that both materials reach a comparable photothermal efficiency per unit mass at low concentrations.

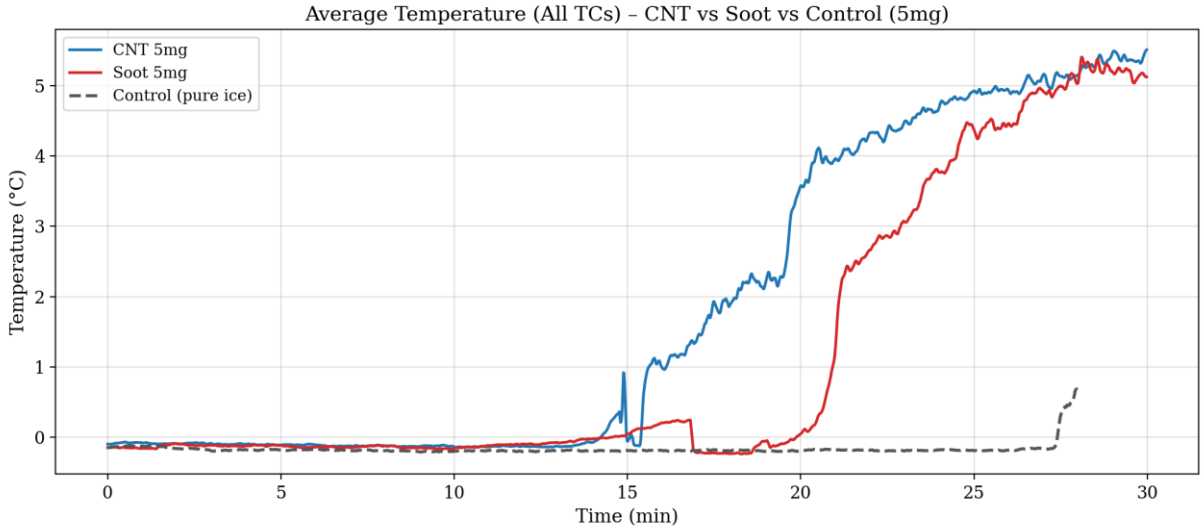

Figure 54: Average temperature (all four TCs) for CNT 5 mg, soot 5 mg, and the pure-ice control. Both contaminants produce elevated average temperatures relative to the control, with CNT exhibiting a marginally earlier onset of surface heating

At 15 mg *(Figure 55)*, both CNT and soot produce results that are virtually identical to the control, with all three curves overlapping closely throughout the experiment. This convergence at 15 mg for two chemically distinct materials strongly suggests that the intermediate loading produces a structural deposit configuration, likely a partially agglomerated or poorly coupled particle layer,

that suppresses photothermal heat transfer regardless of material composition.

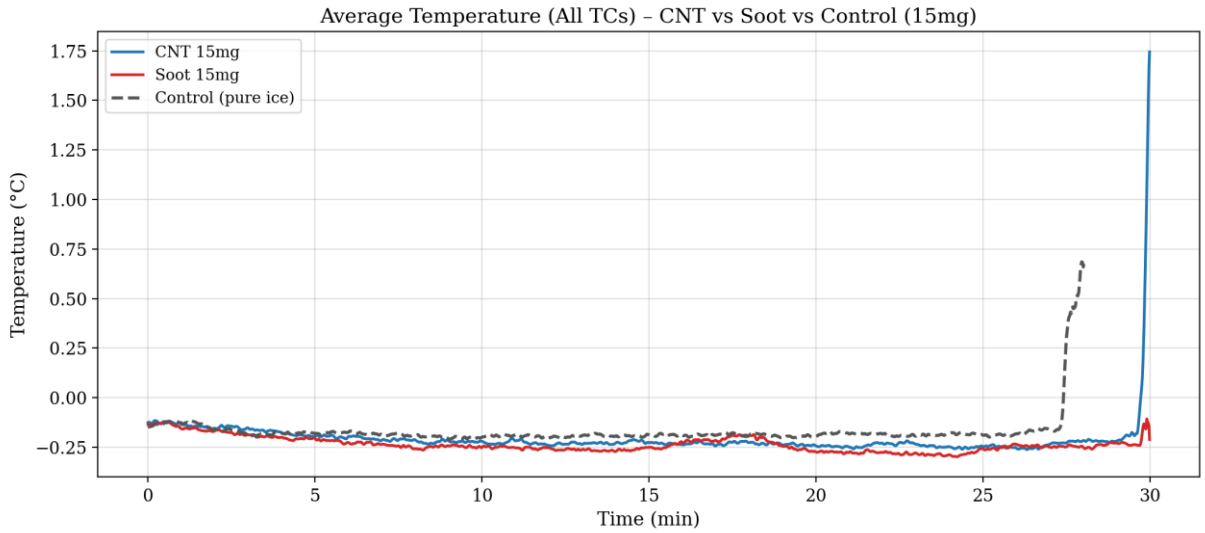

Figure 55:Average temperature (all four TCs) for CNT 15 mg, soot 15 mg, and the pure-ice control. All three curves track closely together, indicating minimal photothermal enhancement at the intermediate loading for both contaminants

At 25 mg (Figure 56), both contaminants generate substantial surface heating above the control, with soot 25 mg producing the higher of the two averages (mean TC4 of +9.76 °C vs +8.36 °C for CNT 25 mg). Despite this, both curves diverge strongly from the control well before the midpoint of the experiment, and both suppress the experiment duration (CNT 25 mg ending at 21.5 min; soot running the full 30 min but with a prolonged high-temperature TC4 episode).

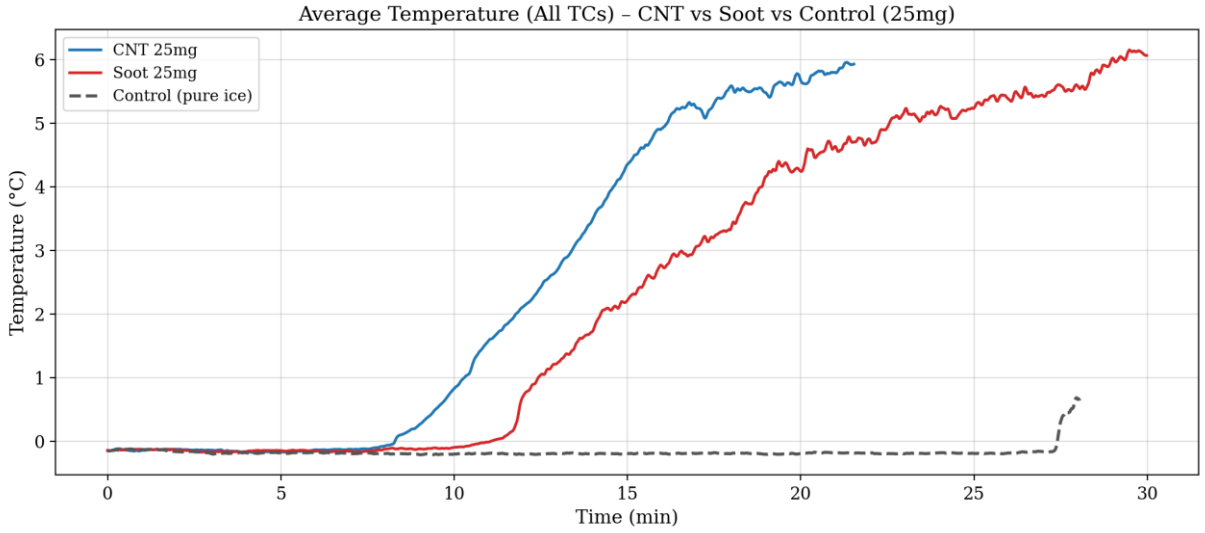

Figure 56:Average temperature (all four TCs) for CNT 25 mg, soot 25 mg, and the pure-ice control. Both contaminants produce strong surface heating; Soot 25 mg generates a slightly higher average driven by its sustained and intense TC4 response.

Temperature by Height: CNT vs Soot vs Control, all Loadings

Figures 56 to 59 present all six contaminated experiments (CNT 5/15/25 mg and soot 5/15/25 mg) alongside the control at each individual thermocouple height. These plots provide the most comprehensive view of the spatial and temporal evolution of photothermal heating across both materials and all loading levels.

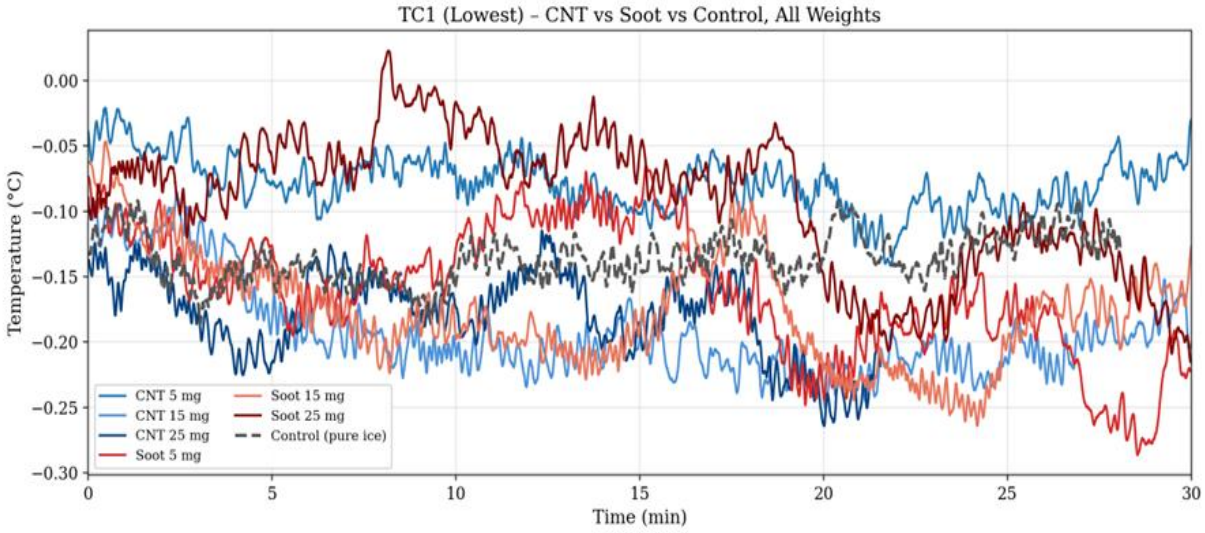

Figure 57: TC1 (lowest height) temperature vs. time for all CNT and soot loadings and the control. All curves remain near the 0 °C melting plateau, confirming no thermal influence of surface contaminants at the lowest measurement point

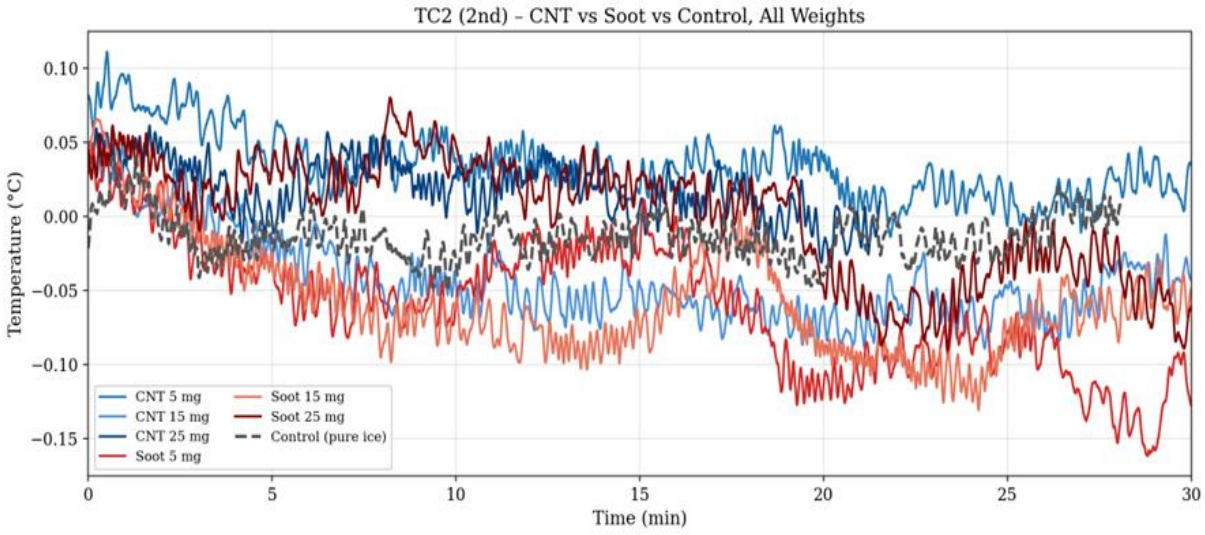

Figure 58:TC2 temperature vs. time for all CNT and soot loadings and the control. No departure from the melting plateau is observed for any loading or material at this height

At TC1 and TC2 (Figures 56 and 57), all contaminated runs are indistinguishable from the control, confirming that the ice bulk is thermally isolated from the surface contaminant effect at these lower heights. At TC3 (Figure 43), only CNT 25 mg shows a slight positive offset, suggesting marginal thermal penetration into the middle of the ice column for the heaviest CNT loading. The control and all other runs remain at the melting plateau at TC3.

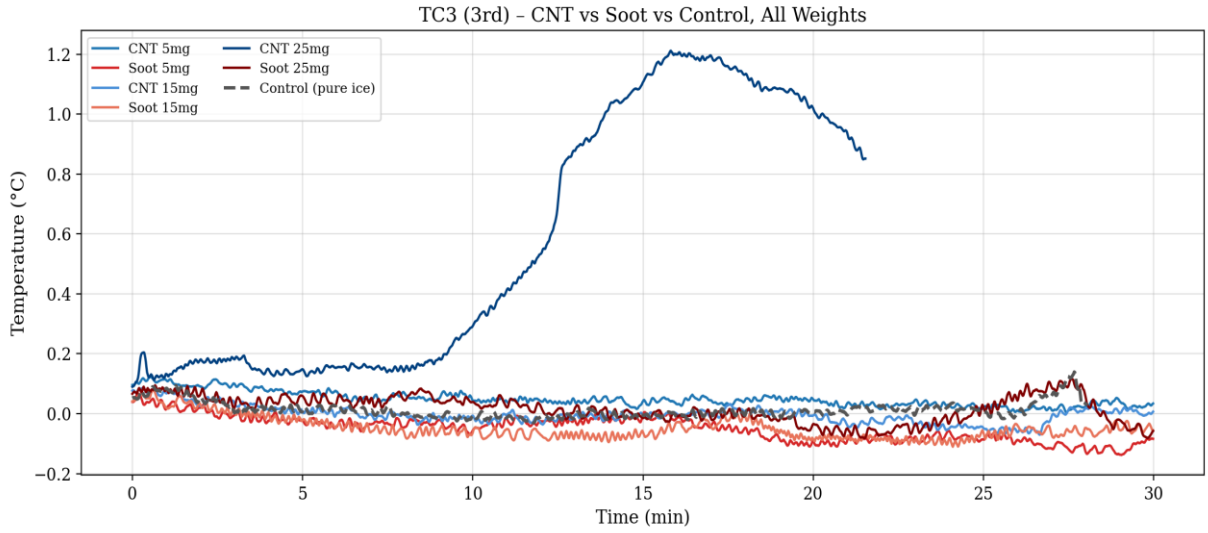

Figure 59: . TC3 temperature vs. time for all CNT and soot loadings and the control. A minor positive deviation is visible for CNT 25 mg, indicating limited thermal penetration; all other runs track the control

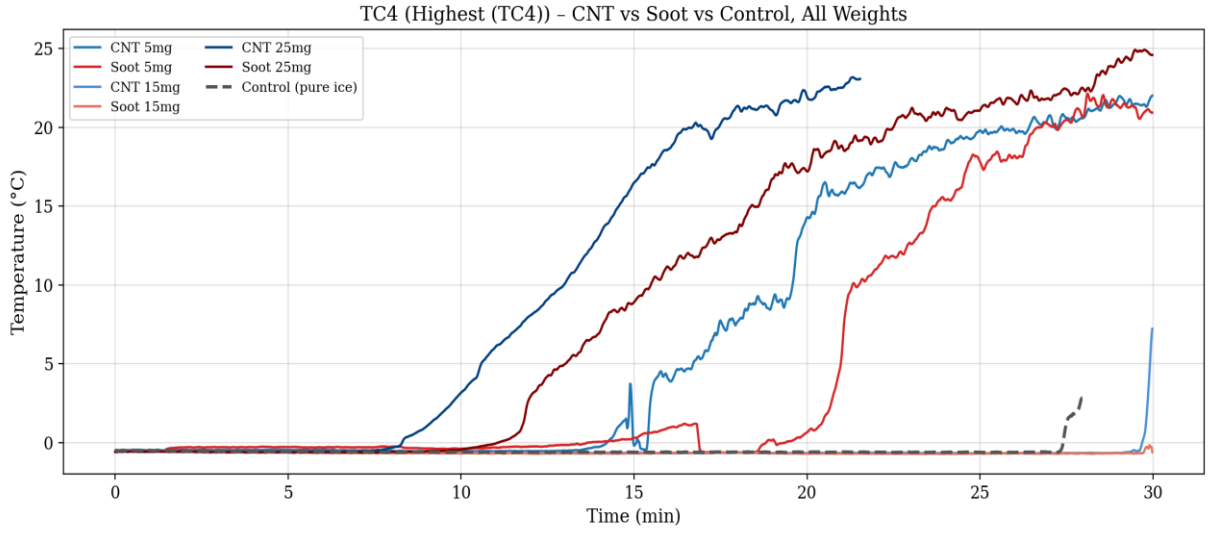

Figure 60: TC4 (highest height, at the ice surface) temperature vs. time for all CNT and soot loadings and the control. Onset times and peak temperatures vary significantly with material and loading, while both 15 mg cases and the control remain clustered near 0

The TC4 plot (Figure 44) is the most information-rich of the four: it shows all six contaminated curves diverging from the control at different times and to different extents. The ordering of onset times, CNT 25 mg (8.9 min) < CNT 5 mg (14.5 min) < soot 25 mg (11.8 min) < soot 5 mg (16.0 min), while the 15 mg cases for both materials track near the control, clearly demonstrates that mass loading and material type jointly determine the photothermal response at the surface. The control and both 15 mg cases form a tight cluster near 0 °C throughout, providing a visual confirmation of the anomalous suppression at this intermediate loading.

5.1.2.4 Summary

Across both CNT and soot experiments, a consistent set of observations emerge. First, photothermal heating is strictly surface-localized: TC1 and TC2 remain thermally unaffected in all contaminated runs, demonstrating that the bulk ice column is governed by latent-heat melting regardless of surface loading. Second, the TC4 thermocouple is the primary indicator of contaminant-driven heating, and its onset time is a reliable proxy for the photothermal effectiveness of a given deposit. Third, an anomalous suppression of heating occurs at 15 mg for both materials, pointing to a loading-dependent transition in deposit morphology or optical coupling efficiency that deserves further characterization. Finally, at equal mass loadings, soot 25 mg produces marginally higher surface temperatures than CNT 25 mg, while CNT 5 mg initiates surface heating slightly earlier than soot 5 mg, suggesting subtle material-level differences in photothermal efficiency that become more pronounced at the extremes of the loading range tested..

5.1.3 Impact of Layered Contaminant

The layered configuration represents a fundamentally different deposition strategy from the surface experiments of Section 5.1.2. Rather than applying the contaminant exclusively to the top ice surface, in this experiment the contaminant mass was distributed at each thermocouple height, deposited at each level and then covered with fresh crushed ice until the next layer was reached, and so on up to the surface. This creates a volumetrically distributed contaminant arrangement embedded throughout the ice column, with particles present at TC1, TC2, TC3, and TC4 positions simultaneously. The two mass loadings selected for this study (5 mg and 25 mg) correspond to the doses that produced the most significant departures from the control in the surface experiment, providing a consistent basis for comparing the two deposition geometries. Both CNT and soot were tested at each loading, again using the same four-thermocouple array, 240 Hz QuickDAQ acquisition, and the same end-point criterion of full melting of the ice layer at TC4.

The key physical distinction of the layered configuration is that heat generation is no longer confined to a single boundary layer at the top surface. Instead, each embedded contaminant layer acts as a localized heat source within the ice column, with the potential to accelerate internal melting and alter the thermal gradient across all four measurement heights simultaneously. This section examines how this changed geometry affects the temperature evolution at each thermocouple, the overall average sample temperature, and the relative performance of CNT versus soot under volumetric loading conditions.

5.1.3.1 Carbon Nanotubes (CNT) – Layered

CNT 5 mg – Layered

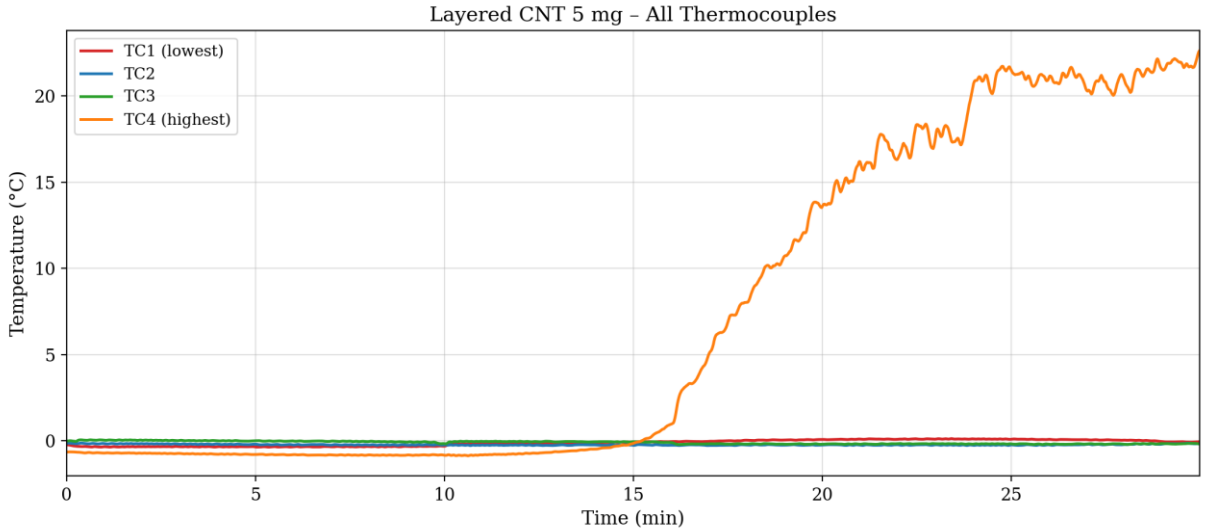

Figure 61: Temperature vs. time at all four thermocouple heights for Layered CNT 5 mg. TC1–TC3 remain near 0 °C throughout the 30-minute test, while TC4 rises sharply from approximately t = 15.9 min, reaching a peak of 22.9 °C consistent with photothermal heating

With 5 mg of CNT deposited at each thermocouple height (total layered distribution), the temperature profiles reveal a markedly different pattern from the surface-only CNT 5 mg case. TC1, TC2, and TC3 continued to register near-0 °C temperatures throughout the 30-minute test, with means of −0.13, −0.24, and −0.11 °C respectively, consistent with sustained latent-heat melting in the lower and middle ice column. However, TC4 rose sharply above the melting plateau beginning at approximately t = 15.9 minutes, reaching a peak of 22.9 °C, comparable in magnitude to the surface CNT 5 mg experiment (22.2 °C, onset 14.5 min). The similarity in TC4 peak temperature but slight delay in onset time (15.9 vs 14.5 min) suggests that in the layered configuration, the CNT particle layer immediately below TC4 acts as the primary heat source for the surface zone, while the lower embedded layers do not produce sufficient localized heating to measurably raise TC1–TC3 above the melting plateau during the observation window.

Notably, TC2 and TC3 show slightly larger negative offsets (means of −0.24 and −0.11 °C) compared to the control and the surface experiment, which may reflect a localized cooling effect from the CNT particles acting as thermal mass sinks within the ice column before the melt front reaches them. This subtle subzero suppression at interior heights is a feature unique to the layered configuration and absent in the surface-only results.

CNT 25 mg – Layered

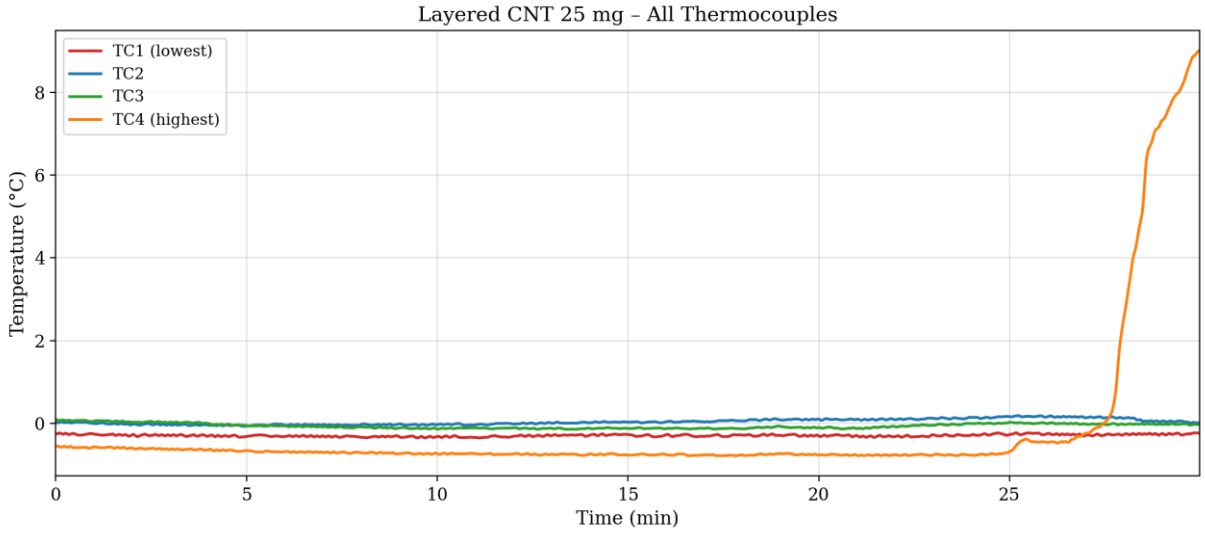

Figure 62: Temperature vs. time at all four thermocouple heights for Layered CNT 25 mg. All channels remain near 0 °C for the majority of the 30-minute experiment, with TC4 exhibiting only a late and modest rise beginning at approximately t = 27.8 min

The layered CNT 25 mg experiment produced a strikingly different result from its surface counterpart. In the surface experiment, CNT 25 mg was the most aggressive case with TC4 rising at t = 8.9 min and a peak of 23.4 °C. In the layered configuration, TC4 did not rise meaningfully until approximately **t = 27.8 minutes** (nearly the full duration of the experiment) reaching a modest maximum of only 9.2 °C. TC1 showed a persistent negative mean of −0.29 °C (the most negative of any TC in this experiment), and TC2 and TC3 also remained slightly below zero throughout, with means of +0.04 and −0.06 °C respectively.

This pronounced suppression relative to both the control and the surface CNT 25 mg result is the most notable finding of the layered CNT experiments. The higher mass loading distributed throughout the column appears to impede rather than accelerate surface melting: the dense CNT layers embedded within the ice may act as thermal barriers or insulating zones, reducing the effective thermal conductivity of the ice column and slowing heat transfer to the surface. Alternatively, the thicker embedded deposits may absorb and re-radiate energy laterally or downward rather than upward to the surface thermocouple. The result is a near-control thermal profile at TC4 for nearly the entire experiment, with only a late and modest temperature rise, in sharp contrast to the rapid and intense TC4 response seen in the surface configuration.

CNT – Layered Average Temperature Comparison

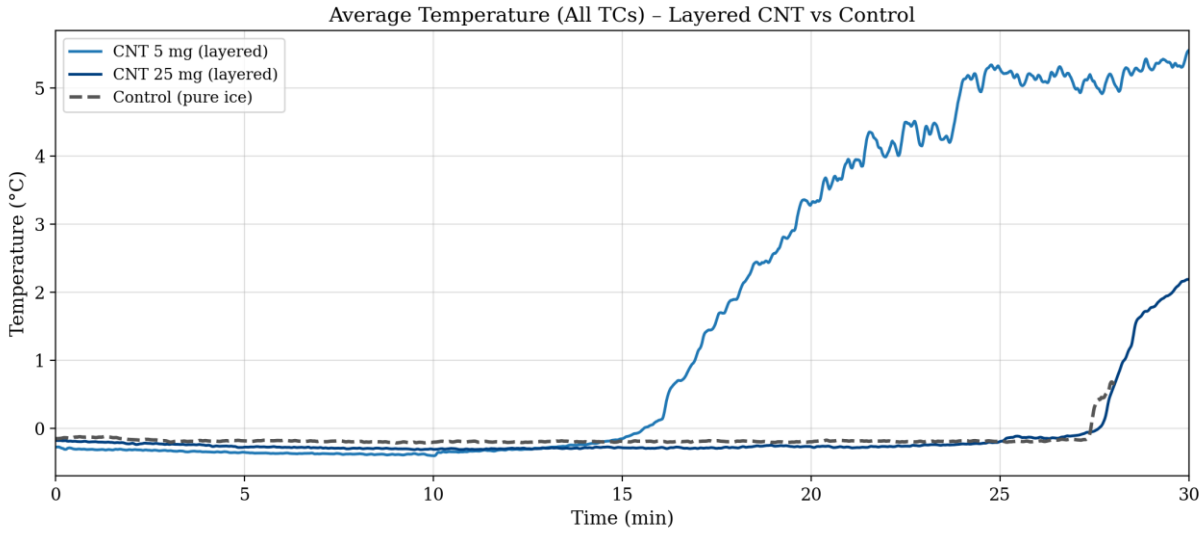

Figure 63: Average temperature of all four thermocouples combined for Layered CNT 5 mg and 25 mg, compared to the pure-ice control. The 5 mg case produces a moderate elevation above the control in the latter half of the experiment, while the 25 mg case tracks the control closely throughout — a reversal of the loading-dependent trend observed in the surface configuration

The averaged four-TC temperature profiles for layered CNT 5 mg and 25 mg, compared against the control, are presented in the figure below. The 5 mg average is elevated above the control in the second half of the experiment due to the TC4 response, while the 25 mg average tracks the control almost exactly throughout. This reversal from the surface experiment where 25 mg

produced the earlier and larger TC4 shows how distributing a higher contaminant mass throughout the ice column fundamentally changes, and in this case suppresses, the photothermal behavior.

CNT – Temperature by Thermocouple Height (Layered)

The per-height comparison figures below show the temperature at each TC for both CNT loadings against the control. TC1 and TC2 are thermally inert for both loadings, confirming that embedded CNT at the lower heights does not locally raise the temperature above the melting plateau. TC3 shows a marginal positive deviation for 5 mg near the end of the experiment, and a slight negative suppression for 25 mg throughout. TC4 is where the two loading cases diverge decisively: 5 mg produces a strong late-experiment rise while 25 mg remains near zero.

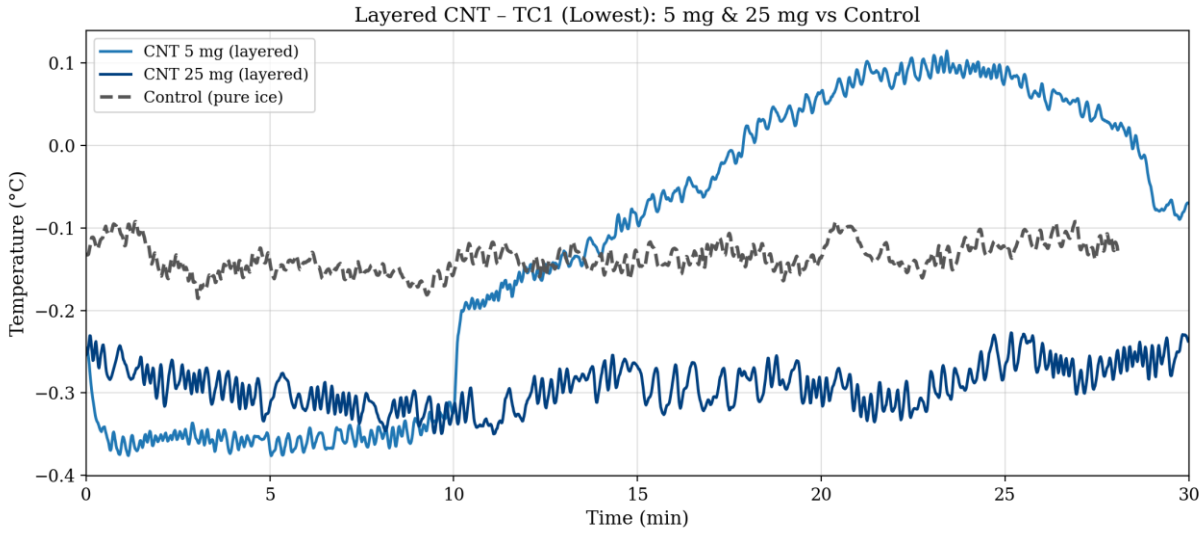

Figure 64: TC1 (lowest height) temperature vs. time for Layered CNT 5 mg and 25 mg vs. Control. Both loadings remain indistinguishable from the control at the lowest thermocouple position.

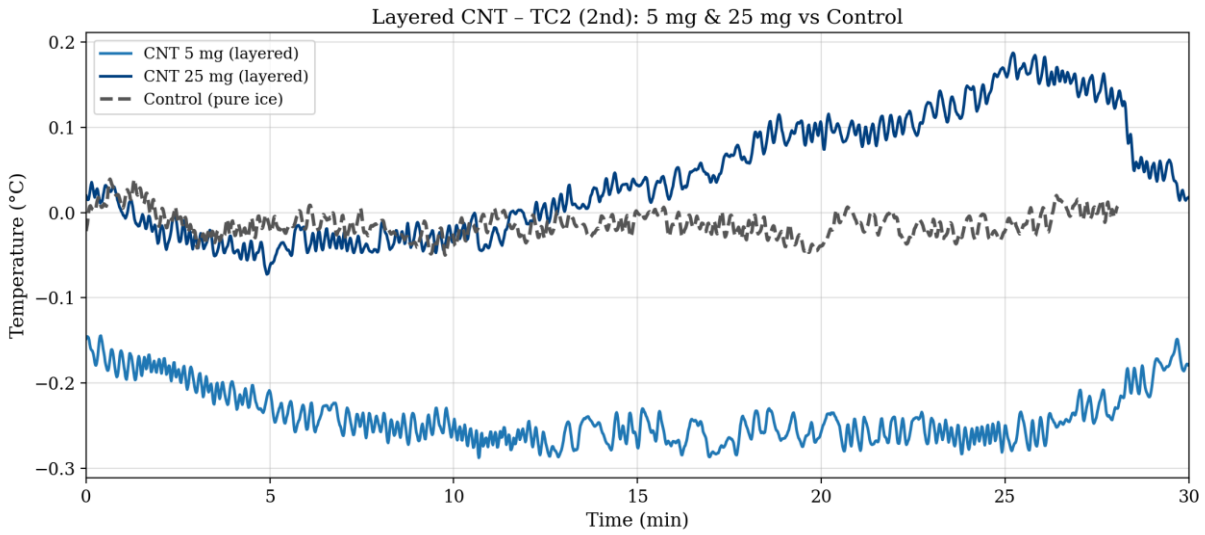

Figure 65: TC2 temperature vs. time for Layered CNT 5 mg and 25 mg vs. Control. No significant departure from the melting plateau is observed for either loading at this height

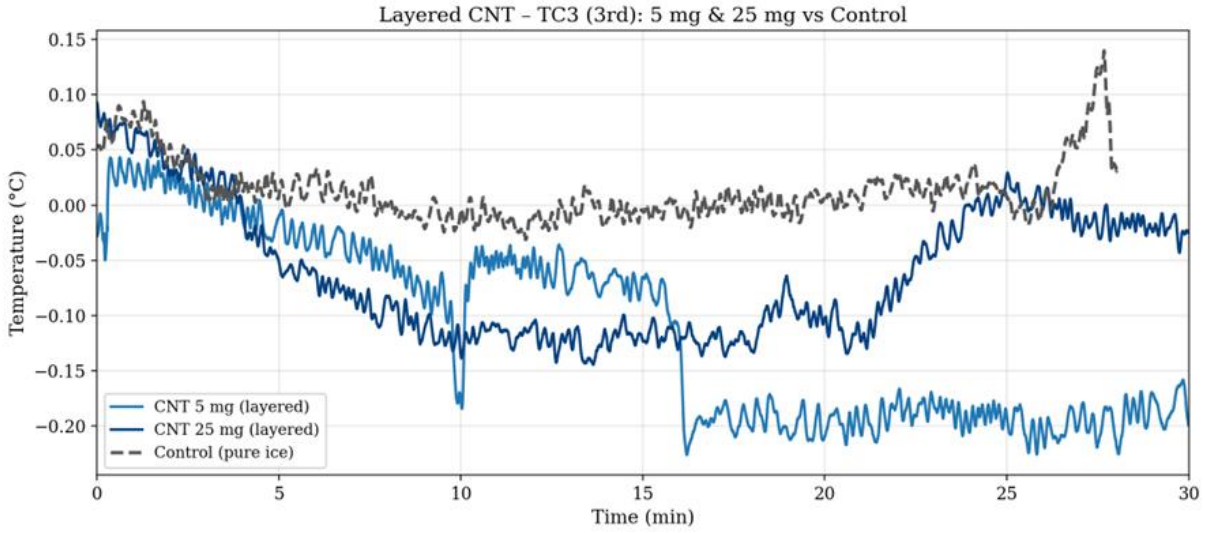

Figure 66: TC3 temperature vs. time for Layered CNT 5 mg and 25 mg vs. Control. Minor deviations are visible in the second half of the experiment; the 25 mg case shows a slight negative offset consistent with localized thermal suppression by the embedded CNT layer

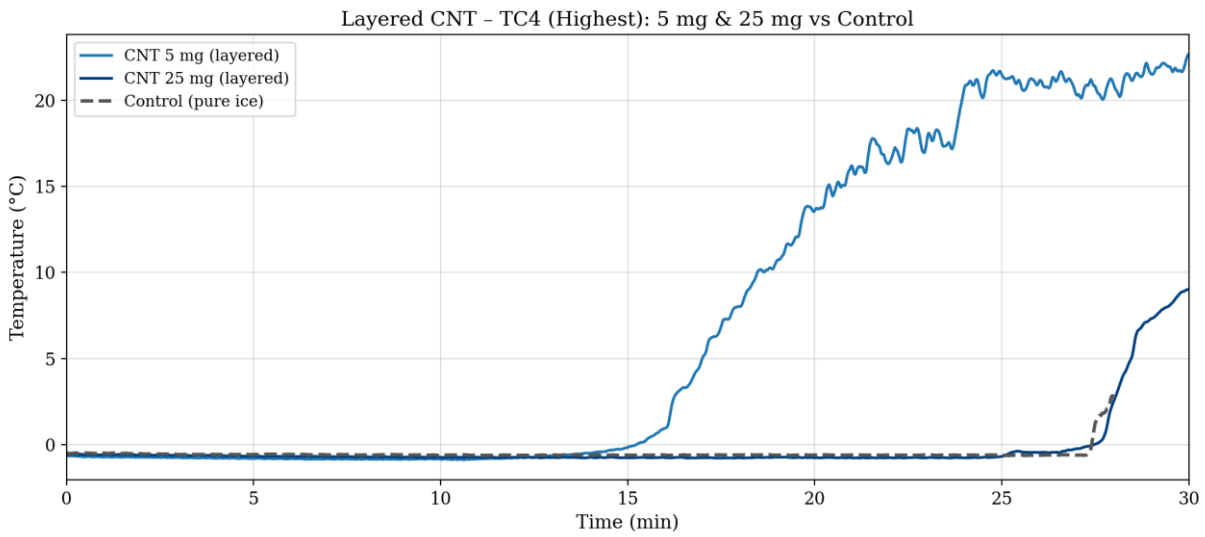

Figure 67: TC4 (highest height) temperature vs. time for Layered CNT 5 mg and 25 mg vs. Control. The 5 mg case produces a pronounced late-experiment rise (onset ≈ 15.9 min, peak 22.9 °C), while the 25 mg case remains near the control baseline until t ≈ 27.8 min, illustrating the suppressive effect of the higher layered loading on surface temperature

5.1.3.2 Soot – Layered

Soot 5 mg – Layered

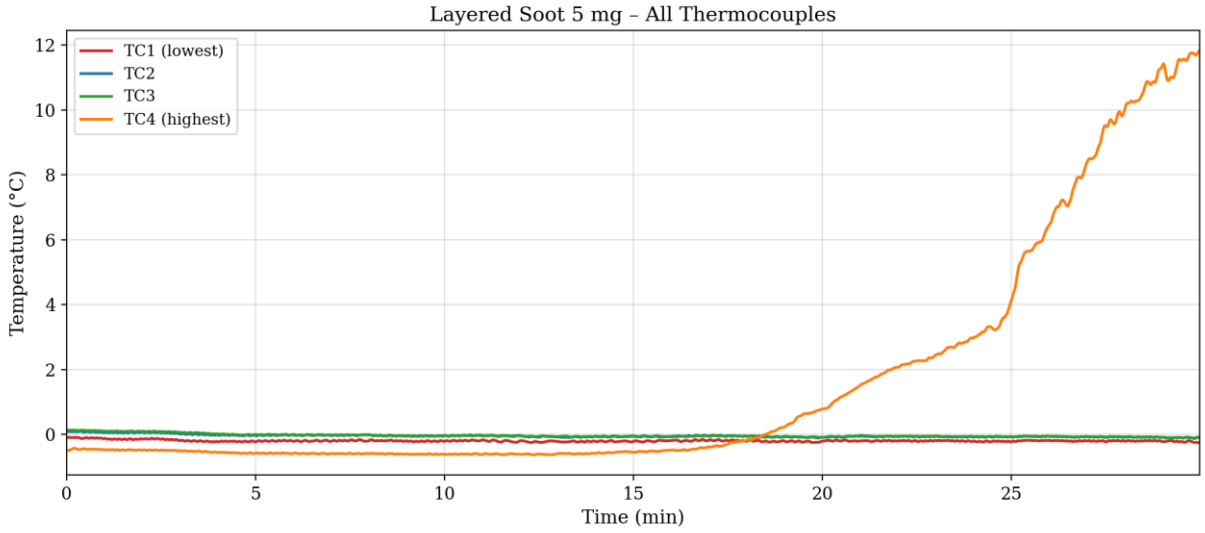

Figure 68: Temperature vs. time at all four thermocouple heights for Layered soot 5 mg. TC1–TC3 remain near 0 °C throughout. TC4 rises from approximately t = 20.2 min, reaching a peak of 12.3 °C — a delayed and lower response compared to the surface soot 5 mg case, consistent with reduced surface concentration in the layered geometry

The layered soot 5 mg experiment produced a moderate surface response. TC1, TC2, and TC3 remained at or near the melting plateau throughout, with means of −0.20, −0.04, and −0.04 °C respectively. TC4 began rising above 1 °C at approximately t = 20.2 minutes, later than both the

surface soot 5 mg onset (16.0 min) and the layered CNT 5 mg onset (15.9 min), and reached a peak of 12.3 °C. The mean TC4 temperature of +1.54 °C reflects the sustained but moderate nature of the heating episode. The delay relative to the surface configuration suggests that distributing the soot mass through the column reduces the effective surface concentration and therefore slows the photothermal heating of the topmost thermocouple. The peak of 12.3 °C, lower than the surface soot 5 mg peak of 22.5 °C, further supports this interpretation: the surface layer in the layered configuration receives only a fraction (one quarter) of the total mass applied in the surface experiment at the same nominal loading.

Soot 25 mg – Layered

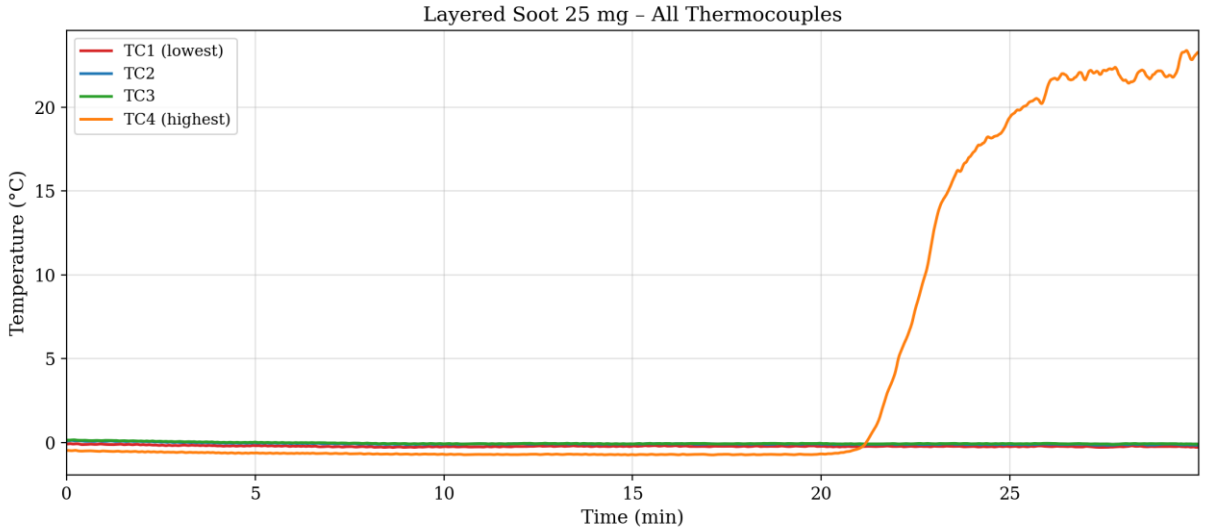

Figure 69: Temperature vs. time at all four thermocouple heights for Layered soot 25 mg. TC1–TC3 maintain the near-0 °C melting plateau throughout. TC4 rises from approximately t = 21.4 min, reaching a peak of 24.6 °C — the highest surface temperature of all layered experiments

Layered soot 25 mg produced the strongest thermal response of all layered experiments. TC4 began rising at approximately t = 21.4 minutes and reached a peak of 24.6 °C, the highest peak of any layered experiment and comparable to surface soot 25 mg (25.1 °C, onset 11.8 min). TC1, TC2, and TC3 remained at or below zero throughout, with means of −0.23, −0.09, and −0.05 °C, indicating that the lower-height soot layers did not produce measurable local heating above the

melting plateau in the observation window. The delay in TC4 onset relative to the surface case (21.4 vs 11.8 min) again reflects the reduced surface-layer concentration in the layered geometry. However, the comparable peak temperature suggests that once the melt front reaches the TC4-level soot layer, the heat release is of similar magnitude to the surface case, as the same total mass (25 mg worth per layer) is locally available.

Compared to layered soot 5 mg, the 25 mg case shows a similar onset time (21.4 vs 20.2 min) but substantially higher peak TC4 temperature (24.6 vs 12.3 °C) and higher mean TC4 temperature (4.60 vs 1.54 °C), confirming a monotonically increasing mass-loading dependence for soot in the layered configuration, in contrast to the non-monotonic behavior observed in the layered CNT results.

Soot – Layered Average Temperature Comparison

The averaged four-TC profiles for layered soot 5 mg and 25 mg against the control show a clear separation between the two loading cases in the second half of the experiment, driven by the differing TC4 responses. The 25 mg average climbs well above both the 5 mg average and the control after approximately t = 21 min, while the 5 mg average shows a more modest elevation. This monotonic loading dependence for soot stands in contrast to the nearly flat 25 mg CNT curve and reflects the different sensitivity of the two materials to increased mass in the layered configuration.

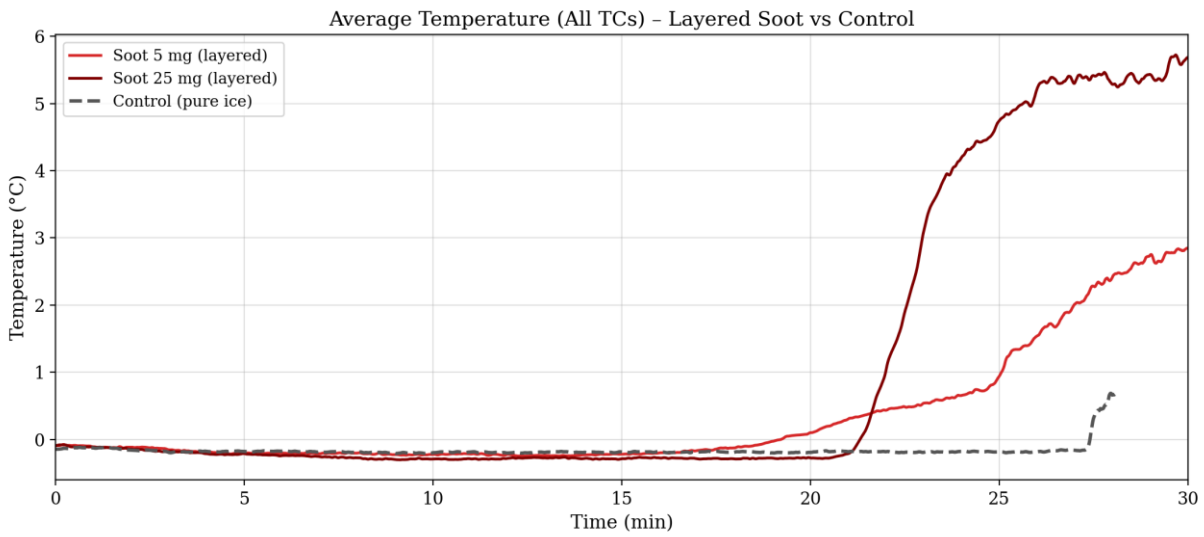

Figure 70: Average temperature of all four thermocouples for layered soot 5 mg and 25 mg vs. control. The 25 mg case shows a pronounced elevation in the latter portion of the experiment driven by TC4, while the 5 mg case produces a more moderate response

Soot – Temperature by Thermocouple Height (Layered)

The per-height figures for soot show a consistent pattern across TC1–TC3: all loadings remain near the control baseline throughout, confirming that the embedded soot layers at the lower heights do not produce measurable local heating during the experiment duration. TC4 is again the sole indicator of contaminant-driven heating, with the 25 mg case showing a substantially higher and more sustained rise than the 5 mg case.

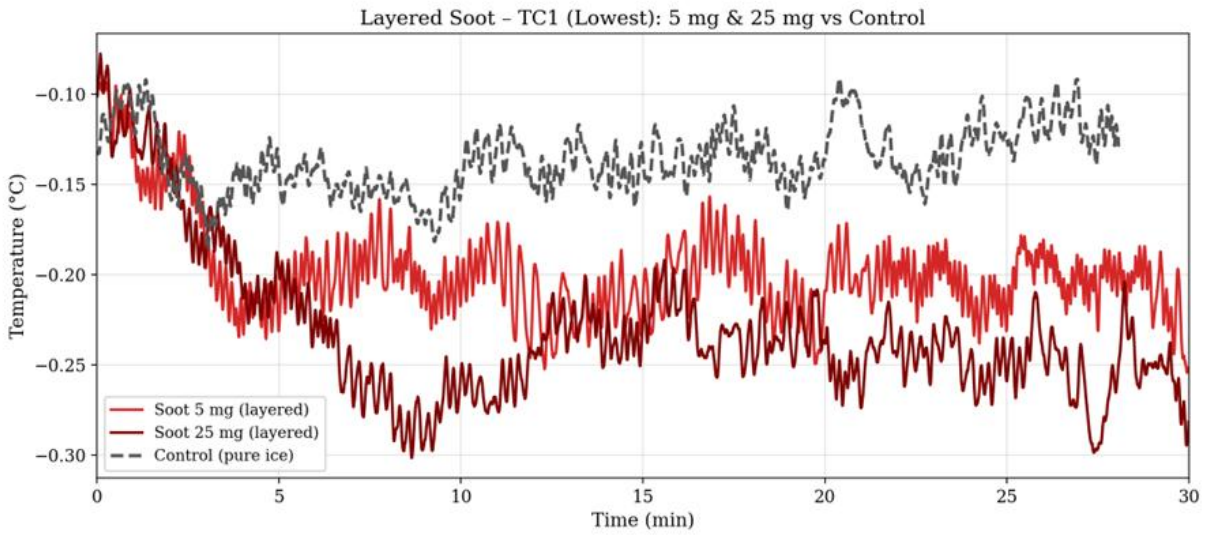

Figure 71: TC1 (lowest height) temperature vs. time for layered soot 5 mg and 25 mg vs. control. No thermal departure is observed at this height for either loading

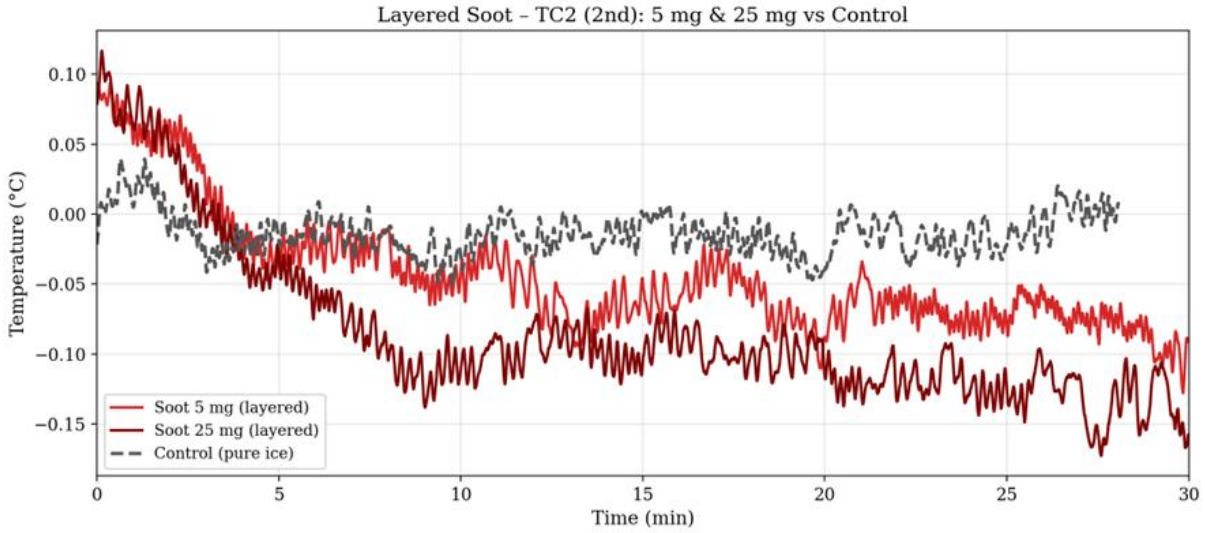

Figure 72: TC2 temperature vs. time for layered soot 5 mg and 25 mg vs. control. Both loadings remain at the near-0 °C melting plateau throughout the experiment

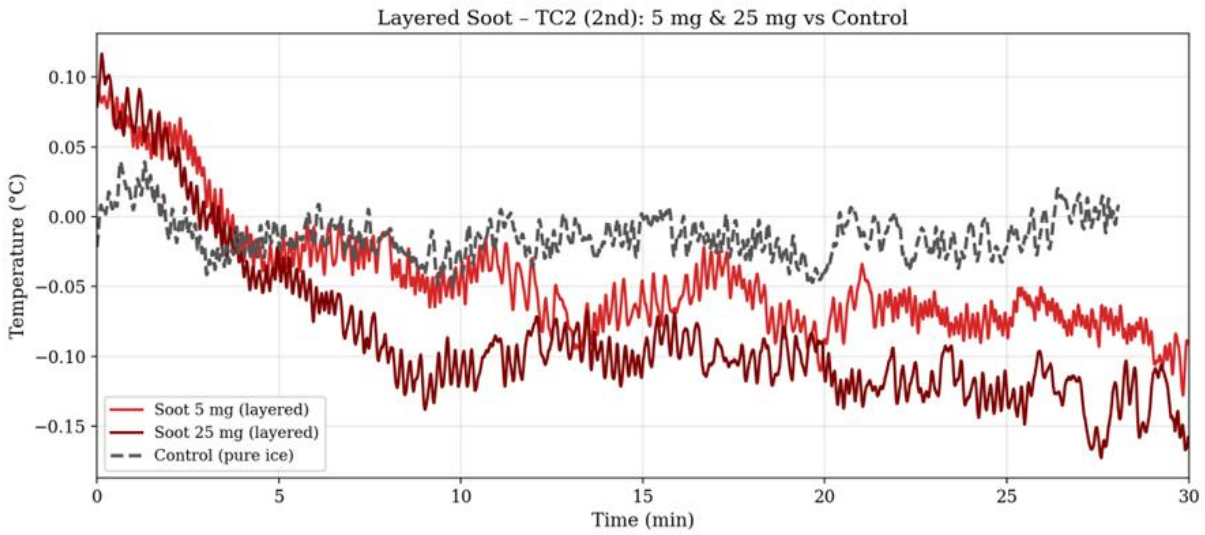

Figure 73: TC3 temperature vs. time for layered soot 5 mg and 25 mg vs. control. No significant departure from the melting plateau is observed at this intermediate height for either Soot loading

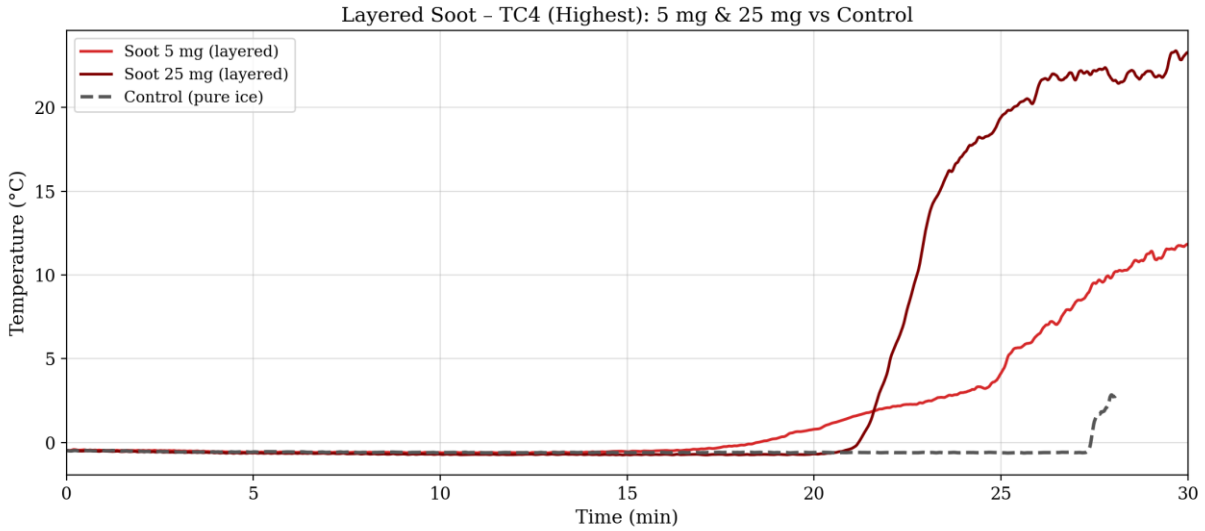

Figure 74: TC4 (highest height) temperature vs. time for layered soot 5 mg and 25 mg vs. control. The 25 mg case produces a substantially higher peak (24.6 °C) than the 5 mg case (12.3 °C), with both showing delayed onsets relative to the equivalent surface experiment

5.1.3.3 Comparing CNT vs Soot – Layered Configuration

This section compares the CNT and soot results directly within the layered configuration, examining both the per-weight averaged temperature response and the per-height profiles across all four experiments.

Average Temperature: CNT vs Soot vs Control by Loading

At 5 mg (*Figure 75*), CNT and soot produce similar average temperature elevations above the control in the second half of the experiment, both driven by TC4. CNT 5 mg shows an earlier TC4 onset (15.9 vs 20.2 min for soot) and higher peak (22.9 vs 12.3 °C), resulting in a higher average temperature overall. This suggests that in the layered geometry, CNT is a more efficient photothermal agent than soot at the 5 mg loading, a reversal from the surface experiment where soot 5 mg produced a slightly later but comparable TC4 response.

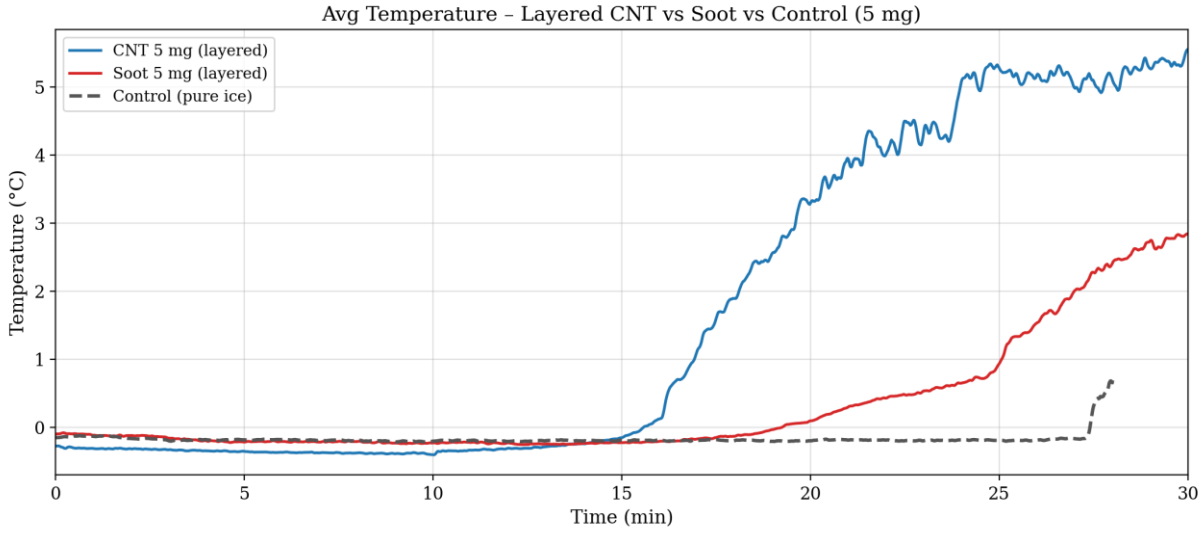

Figure 75:Average temperature (all four TCs) for Layered CNT 5 mg, layered soot 5 mg, and the pure-ice control. CNT 5 mg produces an earlier and higher average elevation than soot 5 mg, both driven by TC4 responses in the second half of the experiment

At 25 mg (Figure 76), the comparison inverts. Layered soot 25 mg generates a substantial average temperature rise above the control (driven by TC4 peak of 24.6 °C), while Layered CNT 25 mg

tracks the control almost exactly throughout the 30-minute test (TC4 peak only 9.2 °C, onset 27.8 min). This produces the largest material-dependent divergence of any comparison in this study: at the same mass and geometry, soot 25 mg delivers nearly three times the TC4 peak temperature of CNT 25 mg in the layered configuration. This may reflect differences in how the two materials disperse and pack within the ice matrix, if CNT particles at high mass form interconnected networks that increase local thermal conductivity and dissipate absorbed heat more rapidly throughout the ice rather than concentrating it at the surface, this could suppress the localized high-temperature response observed for soot.

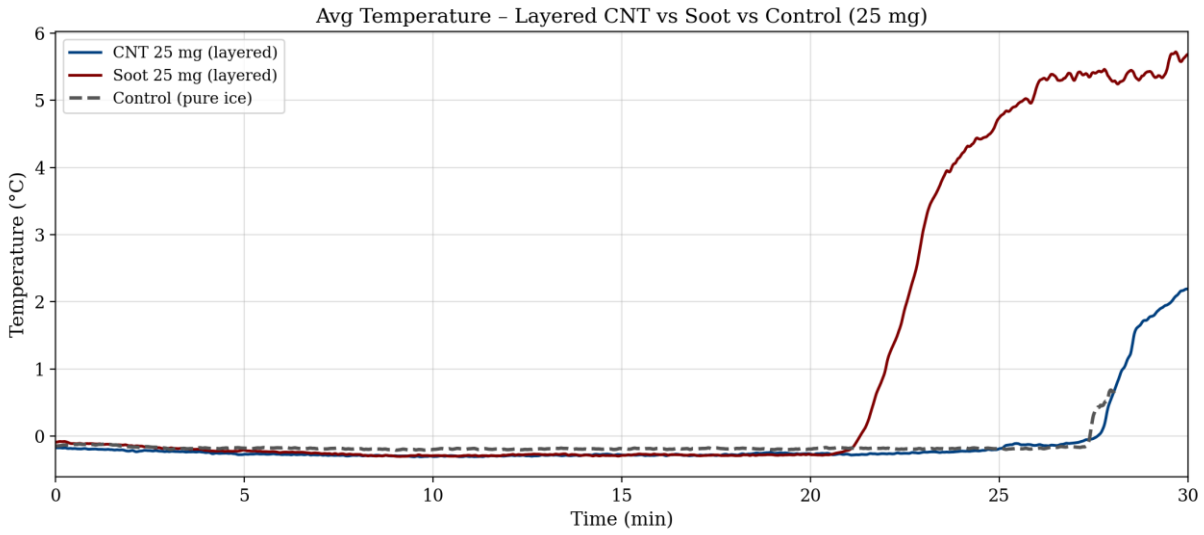

Figure 76: Average temperature (all four TCs) for Layered CNT 25 mg, layered soot 25 mg, and the pure-ice control. The two materials produce dramatically different responses: Soot 25 mg generates a strong average temperature elevation while CNT 25 mg remains near the control baseline throughout

Temperature by Height: All Layered Experiments vs Control

Figures below present the per-TC-height comparison across all four layered experiments and the control. These plots provide the most complete view of how the layered geometry distributes thermal effects across the ice column.

At TC1 and TC2, all four contaminated runs are indistinguishable from the control, confirming that the embedded contaminant layers at the lower heights remain thermally inert throughout the experiment regardless of material or loading. At TC3, minor deviations are visible for layered CNT 25 mg (slight negative offset) and layered soot 25 mg (slight positive offset late in the experiment), but all runs remain near zero. The TC4 plot is the most diagnostic: the four curves separate clearly, with CNT 5 mg and soot 25 mg showing the strongest responses, soot 5 mg a moderate intermediate response, and CNT 25 mg remaining near the control, a non-intuitive ordering that underscores the complex interplay between material type, mass loading, and deposition geometry in governing photothermal ice melting.

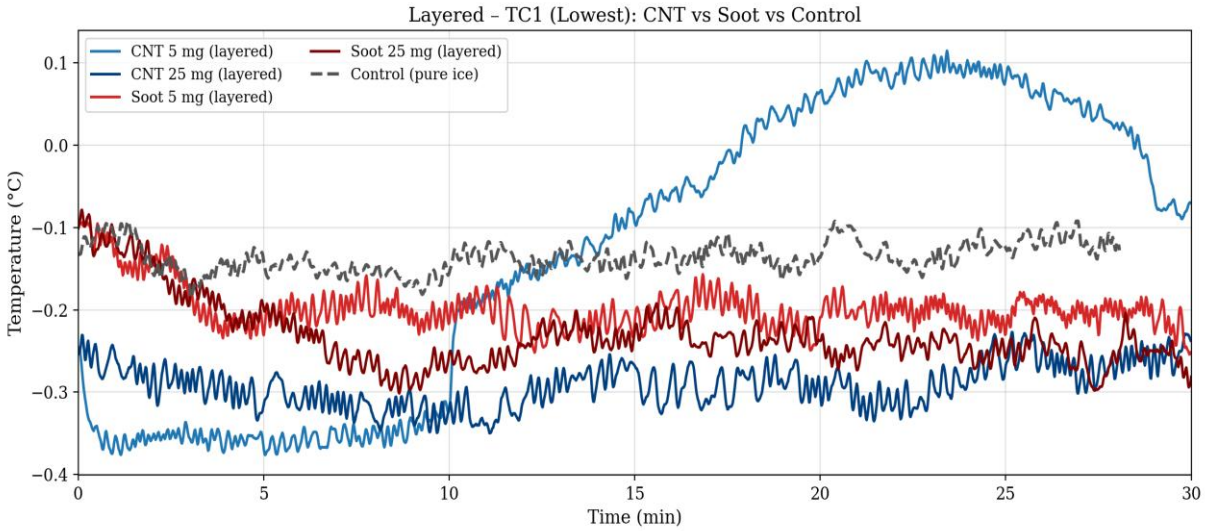

Figure 77: TC1 (lowest height) temperature vs. time for all layered experiments and the control. All runs remain near 0 °C throughout, confirming no thermal effect at the lowest thermocouple position regardless of contaminant type or loading

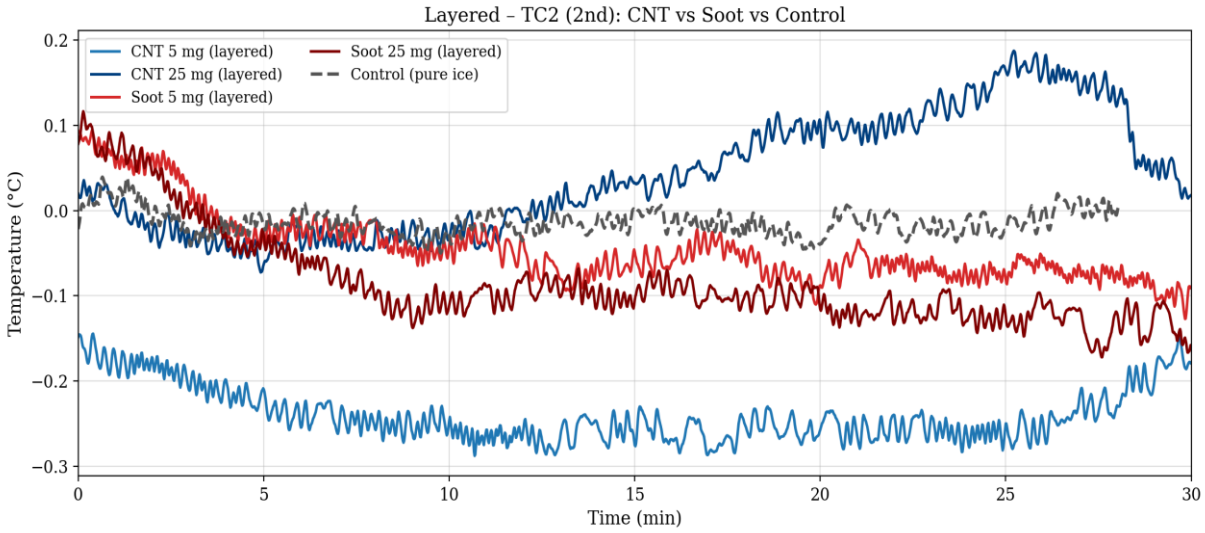

Figure 78: TC2 temperature vs. time for all layered experiments and the control. No measurable departure from the melting plateau is observed for any experiment at this height

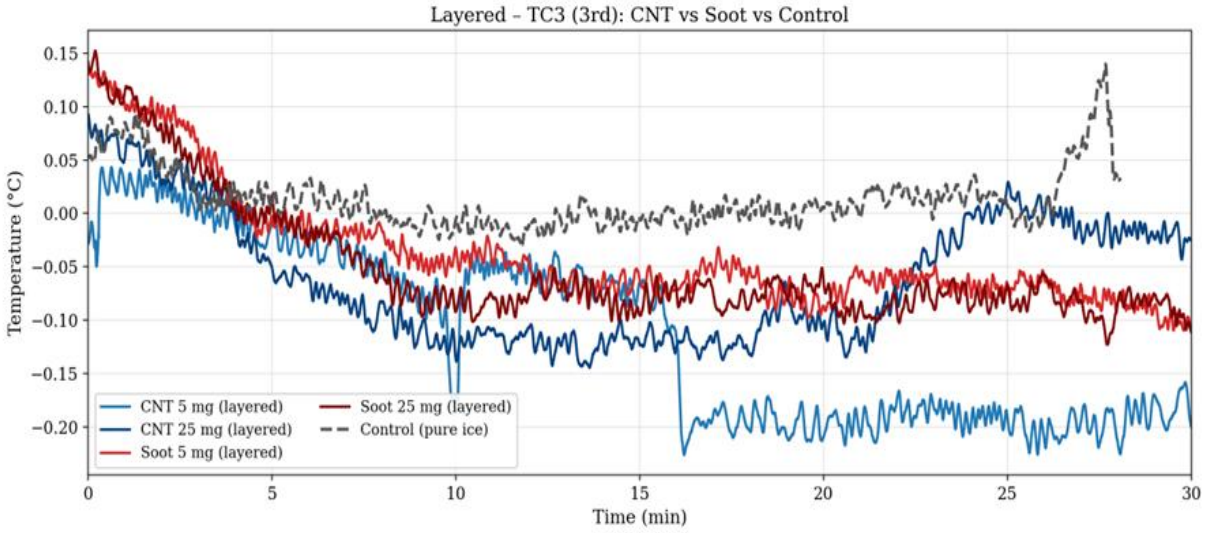

Figure 79: TC3 temperature vs. time for all layered experiments and the control. Minor deviations are visible for CNT 25 mg (slight negative offset) and soot 25 mg (marginal late positive rise), but all runs remain near the 0 °C plateau

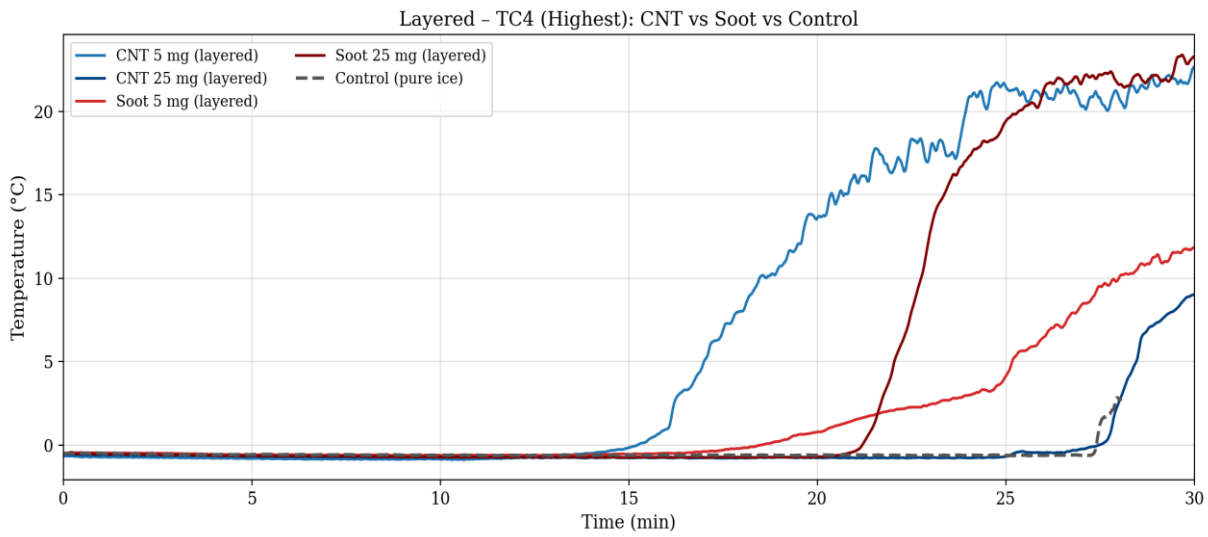

Figure 80: TC4 (highest height) temperature vs. time for all layered experiments and the control. CNT 5 mg and soot 25 mg produce the strongest responses; soot 5 mg a moderate rise; and CNT 25 mg remains near the control throughout

5.1.3.4 Summary and Comparison with Surface Configuration

The layered contaminant experiments reveal several key findings that distinguish volumetric deposition from the surface-only configuration of Section 5.1.2. First, the dominant heat-generation zone remains TC4 in all layered experiments; despite the contaminant being present at all heights, only the top thermocouple position consistently records elevated temperatures. This confirms that the photothermal effect is primarily driven by solar radiation incident on the uppermost exposed layer of the ice column, not by internal heat generation from the embedded lower layers, at least within the 30-minute experimental window.

Second, the onset times for TC4 heating are systematically delayed in the layered configuration relative to the surface experiments at the same nominal loading. This is consistent with the reduced surface-layer concentration: in the layered geometry, each individual layer receives a mass equal

to the total loading divided by the number of layers, resulting in a lower local contaminant density at the surface and a reduced photothermal effect per unit area.

Third, and most strikingly, the high-loading cases diverge dramatically between CNT and soot: Layered CNT 25 mg produced the weakest response of all layered experiments (TC4 peak 9.2 °C, onset 27.8 min), while Layered soot 25 mg produced the strongest (TC4 peak 24.6 °C, onset 21.4 min). No such divergence was observed in the surface experiments, where both materials at 25 mg produced comparable TC4 peaks (~23–25 °C). This suggests a fundamental difference in how CNT and soot particles interact with the ice matrix at high volumetric concentrations, with CNT potentially forming thermally conductive networks that redistribute absorbed heat diffusely rather than concentrating it at the surface.

These findings carry important implications for real-world scenarios: contaminants that are well-mixed throughout a snowpack or ice layer may behave very differently from surface deposits, and the relationship between total contaminant mass and melting acceleration is highly sensitive to both the spatial distribution of the material and its intrinsic physical properties at the relevant concentration.

5.1.4 Mixed ratio

The experiments described in this section extend the surface deposition methodology of Section 5.1.2 by investigating what happens when CNT and soot are combined in varying mass ratios before being deposited on the ice surface (see Figure 30). In all previous experiments, the two materials were tested individually. Here, the total deposited mass is held constant at 25 mg while the CNT-to-soot ratio is systematically varied across five combinations, spanning the full range

from CNT-dominant to soot-dominant mixtures. This approach isolates the effect of material composition from the effect of total mass and allows the photothermal contributions of each component to be disentangled through their interaction in a binary mixture.

The five mixtures tested are summarized in Table 1 below. The ratio notation "xCNT:ySoot" denotes the proportion of each component, and the corresponding masses (CNT mass / Soot mass) are calculated from the 25 mg total.

Table 4: Mixed-ratio experiment summary (total surface deposit = 25 mg)

Ratio	CNT mass	Soot mass
3CNT:1Soot	18.75 mg	6.25 mg
2CNT:1Soot	16.67 mg	8.33 mg
1CNT:1Soot	12.50 mg	12.50 mg
1CNT:2Soot	8.33 mg	16.67 mg
1CNT:3Soot	6.25 mg	18.75 mg

5.1.4.1 Individual Mixture Results

3CNT:1Soot (18.75 mg CNT / 6.25 mg Soot)

The CNT-dominant mixture at a 3:1 ratio produced the most striking result of the entire mixed-ratio series: TC4 showed no measurable surface heating throughout the full 30-minute experiment, with a maximum temperature of only −0.43 °C and a mean of −0.71 °C, values that are more negative than even the pure-ice control (TC4 mean −0.53 °C). TC1, TC2, and TC3 similarly remained below zero, with means of −0.29, −0.15, and −0.09 °C respectively. This complete absence of photothermal heating is unexpected given that CNT alone at 25 mg (Section 5.1.2) produced a TC4 rise at t = 8.9 min. The addition of even a small amount of soot (6.25 mg, 25%

of total mass) appears to fundamentally suppress the CNT photothermal response at this ratio, resulting in a deposit that behaves as if it were thermally inert.

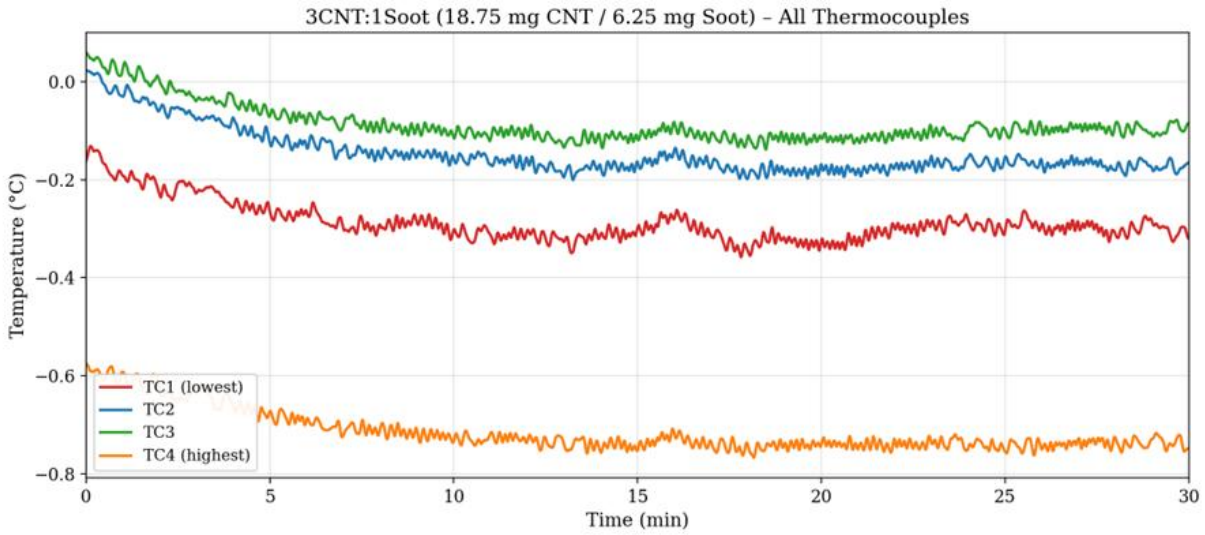

Figure 81: Temperature vs. time at all four thermocouple heights for the 3CNT:1Soot mixture (18.75 mg CNT + 6.25 mg Soot). All channels remain below 0 °C throughout the 30-minute experiment — no photothermal surface heating is observed at this CNT-dominant ratio

2CNT:1Soot (16.67 mg CNT / 8.33 mg Soot)

Reducing the CNT fraction to 2:1 (67% CNT) produced a dramatically different result. TC4 began rising above 1 °C at approximately t = 8.8 minutes, the earliest onset of any mixed-ratio experiment, reaching a peak of 18.5 °C and a mean of +3.90 °C. TC1, TC2, and TC3 remained near the melting plateau (means of −0.21, −0.10, and −0.05 °C), confirming that the heating was strictly surface-localized. The abrupt change in behavior between the 3:1 and 2:1 CNT:Soot ratios (from complete suppression to one of the strongest surface responses) suggests a sharp transition in the deposit's optical and thermal properties near this compositional threshold.

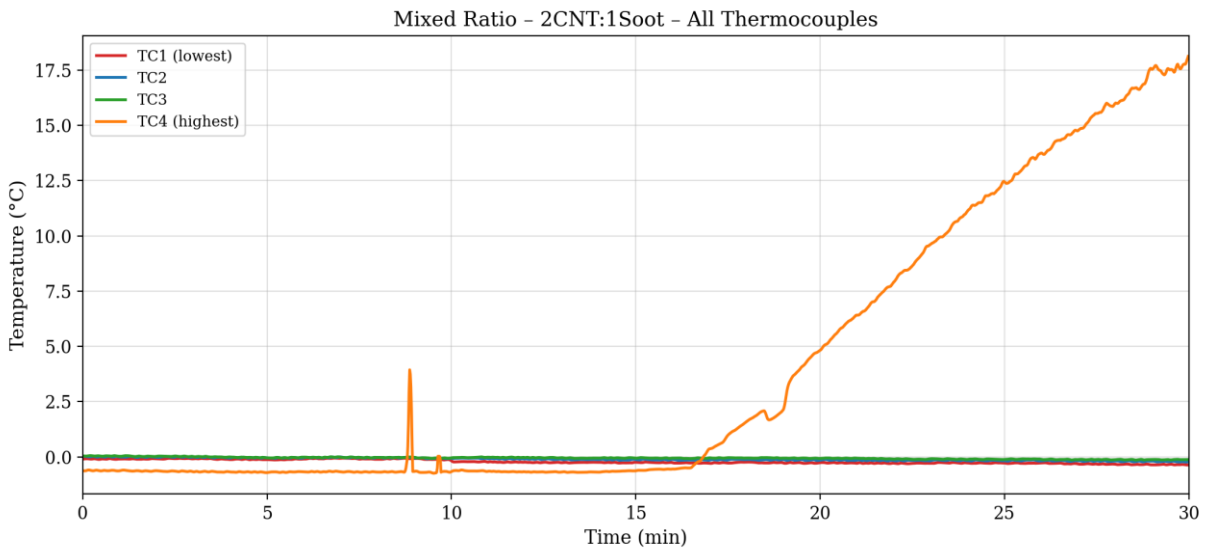

Figure 82: Temperature vs. time at all four thermocouple heights for the 2CNT:1Soot mixture (16.67 mg CNT + 8.33 mg Soot). TC4 rises sharply from t ≈ 8.8 min, reaching a peak of 18.5 °C. Lower thermocouples remain at the melting plateau, confirming surface-localized photothermal heating

1CNT:1Soot (12.5 mg CNT / 12.5 mg Soot)

The equal-mass mixture (50% CNT, 50% Soot) produced a TC4 rise beginning at approximately t = 16.1 minutes and reaching a peak of 23.6 °C, the highest peak temperature of the mixed-ratio series. The mean TC4 temperature of +6.35 °C reflects a sustained and intense surface-heating episode in the second half of the experiment. TC1–TC3 remained near 0 °C throughout (means of −0.17, −0.08, and −0.09 °C). The later onset relative to 2CNT:1Soot (16.1 vs 8.8 min) but higher peak temperature suggests that the equal-ratio mixture generates a different type of surface interaction, possibly a more uniform mixed particle layer that, once optically activated, sustains a higher peak temperature than the CNT-dominant 2:1 mixture.

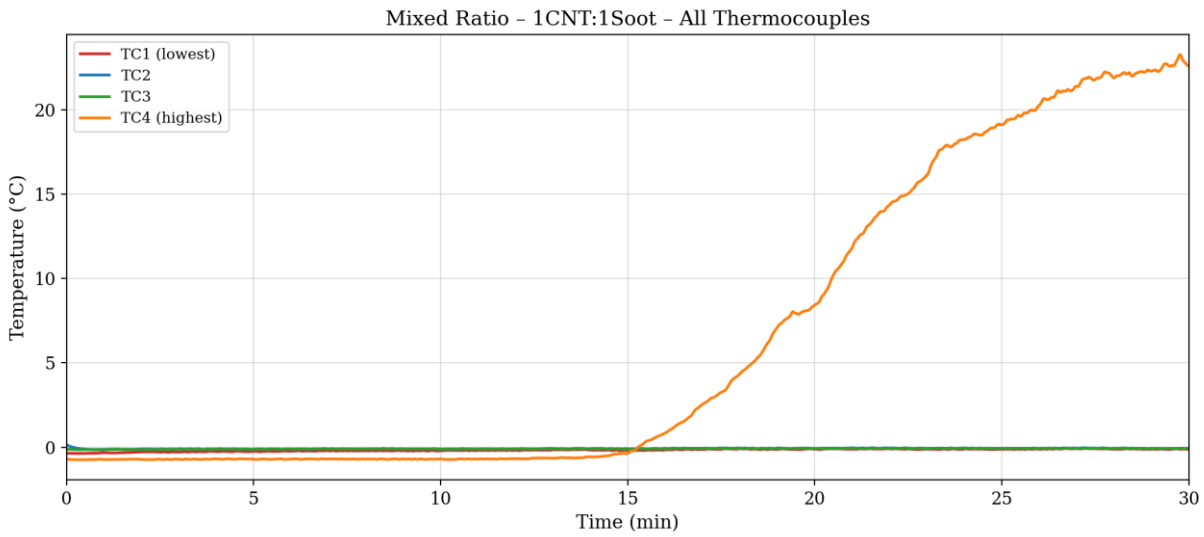

Figure 83: Temperature vs. time at all four thermocouple heights for the 1CNT:1Soot mixture (12.5 mg each). TC4 rises from t ≈ 16.1 min, reaching the highest peak temperature of the mixed-ratio series at 23.6 °C. Lower thermocouples remain near the melting plateau

1CNT:2Soot (8.33 mg CNT / 16.67 mg Soot)

The soot-dominant 1:2 mixture (33% CNT, 67% Soot) mirrors the 3CNT:1Soot result in a strikingly symmetric way: TC4 again showed no significant surface heating throughout the 30-minute test, with a maximum of only 0.009 °C and a mean of −0.82 °C, the most negative TC4 mean of any experiment in this study. All lower thermocouples also remained at or below zero. The fact that both the most CNT-heavy (3:1) and most soot-heavy (2:1 Soot) mixtures produce zero surface response, while the intermediate ratios generate strong TC4 rises, points strongly to a compositional window effect: photothermal heating requires a specific range of CNT-to-soot proportions. Outside this window, in either direction, the mixture appears to form an inert deposit.

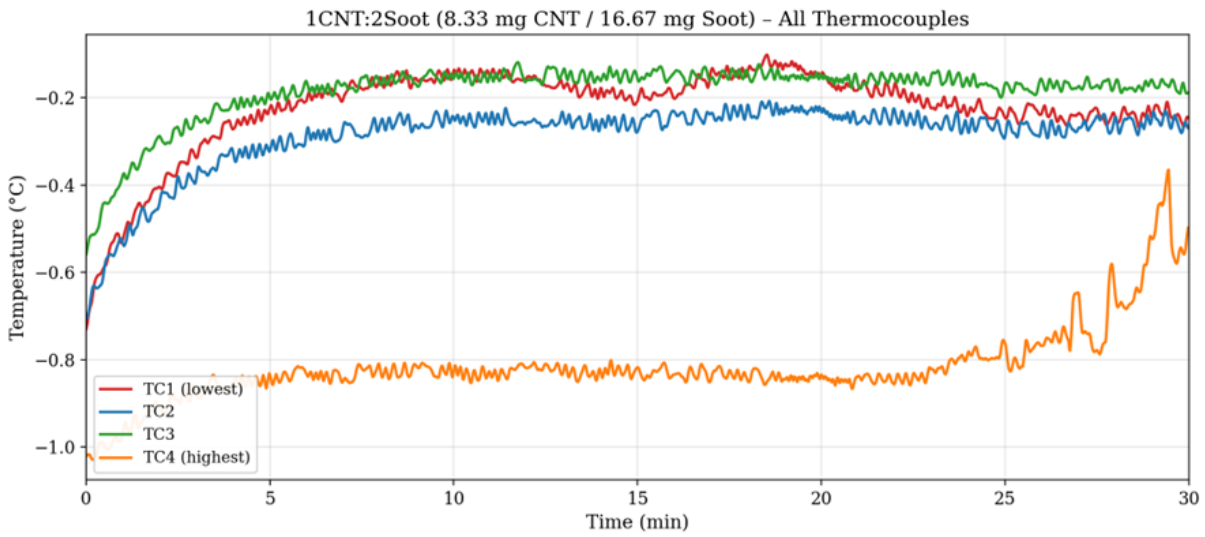

Figure 84: Temperature vs. time at all four thermocouple heights for the 1CNT:2Soot mixture (8.33 mg CNT + 16.67 mg Soot). All channels remain at or below 0 °C throughout — no photothermal surface heating is observed, mirroring the suppression seen at the CNT-dominant 3:1 ratio

1CNT:3Soot (6.25 mg CNT / 18.75 mg Soot)

The most Soot-rich mixture (75% Soot, 25% CNT) recovered a surface heating response, with TC4 rising above 1 °C at approximately t = 23.6 minutes and reaching a peak of 24.2 °C, comparable in magnitude to the 1CNT:1Soot peak (23.6 °C) but with a substantially later onset. TC1–TC3 remained near the melting plateau throughout (means of −0.10, −0.15, and −0.08 °C). The late onset but high peak suggests that the Soot-dominant mixture requires a longer thermal activation period before the surface layer reaches the threshold for rapid photothermal heating, after which the response is intense and comparable to the equal-ratio case. The mean TC4 of +2.75 °C (lower than the 1:1 case (+6.35 °C)) reflects the shorter duration of the high-temperature episode within the 30-minute window.

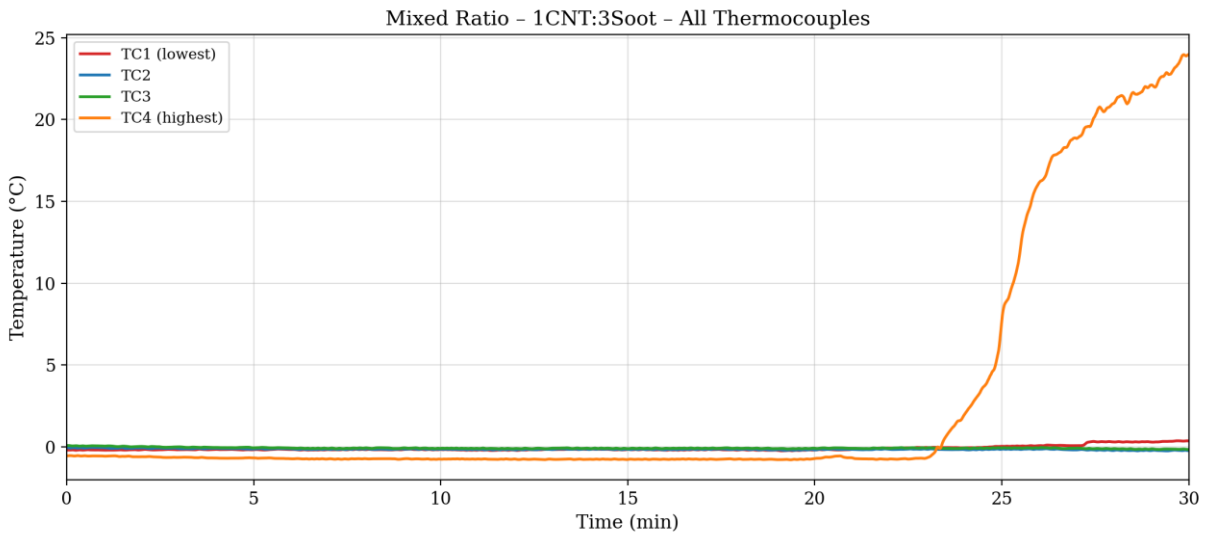

Figure 85: Temperature vs. time at all four thermocouple heights for the 1CNT:3Soot mixture (6.25 mg CNT + 18.75 mg Soot). TC4 rises from t ≈ 23.6 min, reaching 24.2 °C, demonstrating that surface heating recovers at the Soot-dominant extreme despite the complete suppression observed at the 1CNT:2Soot ratio

5.1.4.2 Average Temperature – All Ratios vs Control

The averaged four-TC temperature profiles for all five mixed ratios and the control are presented together in the figure below, providing an overview of how the mixture composition governs the overall sample thermal response.

The plot reveals a non-monotonic and asymmetric dependence on ratio: two ratios (3CNT:1Soot and 1CNT:2Soot) produce curves that track the control baseline throughout, while three ratios (2CNT:1Soot, 1CNT:1Soot, and 1CNT:3Soot) generate increasingly elevated averages driven by their respective TC4 responses. The 2CNT:1Soot curve rises earliest and sustains a moderate elevation, the 1CNT:1Soot curve rises later but reaches a higher sustained average, and the 1CNT:3Soot curve rises latest but ultimately climbs steeply toward the end of the experiment. The two non-responding ratios flatten the average entirely, creating a bimodal distribution of behaviors (responding and non-responding) within the five-mixture series.

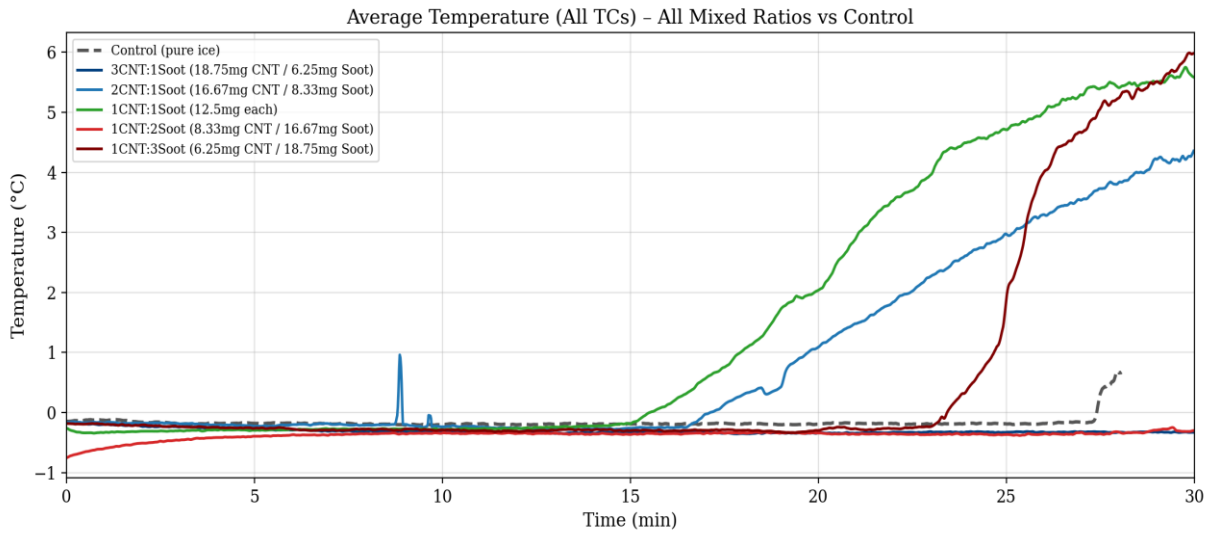

Figure 86: Average temperature of all four thermocouples for all five CNT: Soot mixed ratios and the pure-ice control. Three ratios (2CNT:1Soot, 1CNT:1Soot, 1CNT:3Soot) produce elevated averages driven by TC4 surface heating. Two ratios (3CNT:1Soot and 1CNT:2Soot) remain indistinguishable from the control throughout the experiment

5.1.4.3 Temperature by Thermocouple Height – All Ratios

Figures below present the temperature at each individual thermocouple height across all mixed ratios and the control. These per-height plots decompose the average response and confirm the spatial extent of photothermal heating across the ice column.

At TC1 and TC2 (lowest heights), all five mixed ratios remain indistinguishable from pure-ice control throughout the 30-minute experiment. No mixture, regardless of composition, produces any measurable heating at the lower thermocouple positions. At TC3, all ratios similarly track the control, with only minor noise-level fluctuations. This confirms that the mixed-ratio surface deposit, like the individual surface deposits in Section 5.1.2, produces strictly surface-localized photothermal heating, the thermal influence does not penetrate below the uppermost thermocouple layer.

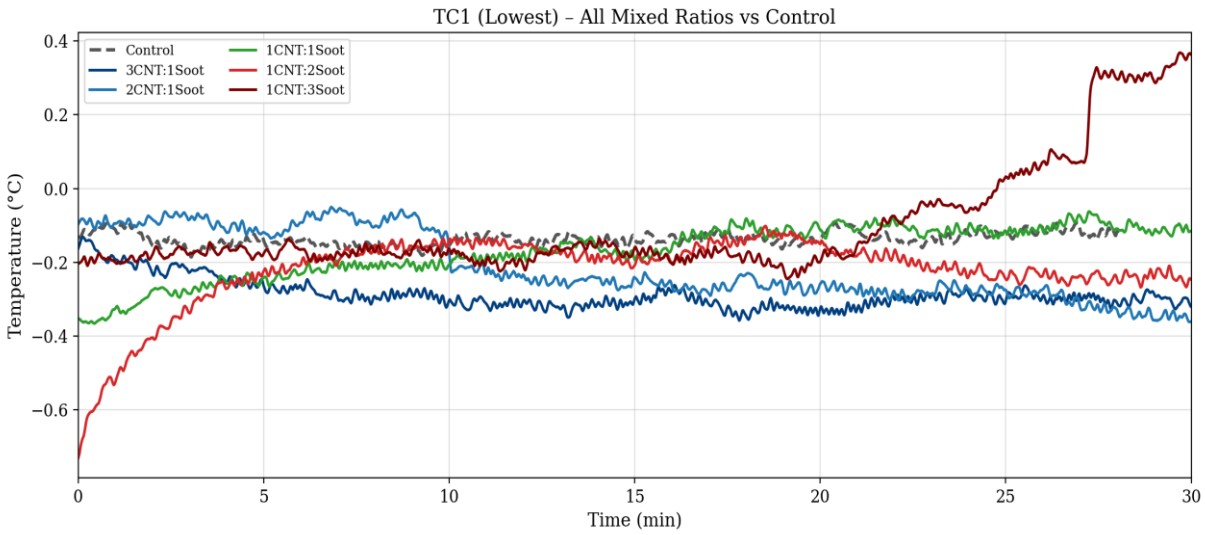

Figure 87: TC1 (lowest height) temperature vs. time for all mixed ratios and the control. All curves remain near 0 °C throughout, confirming no photothermal influence at the lowest thermocouple position for any mixture

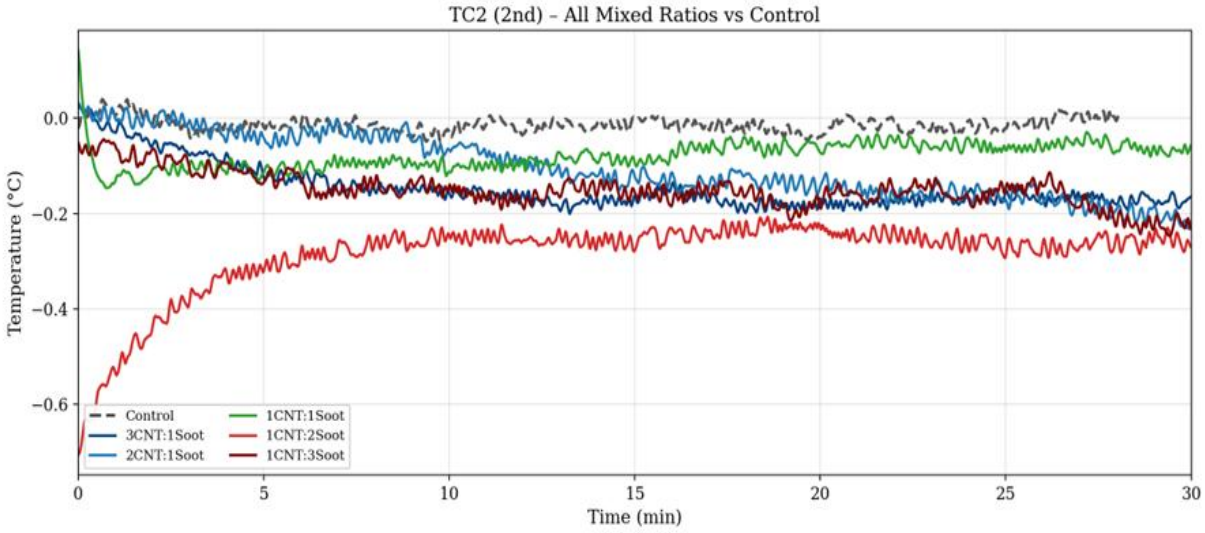

Figure 88: TC2 temperature vs. time for all mixed ratios and the control. All curves remain at the near-0 °C melting plateau, consistent with the surface-localized nature of photothermal heating in all mixed-ratio experiments

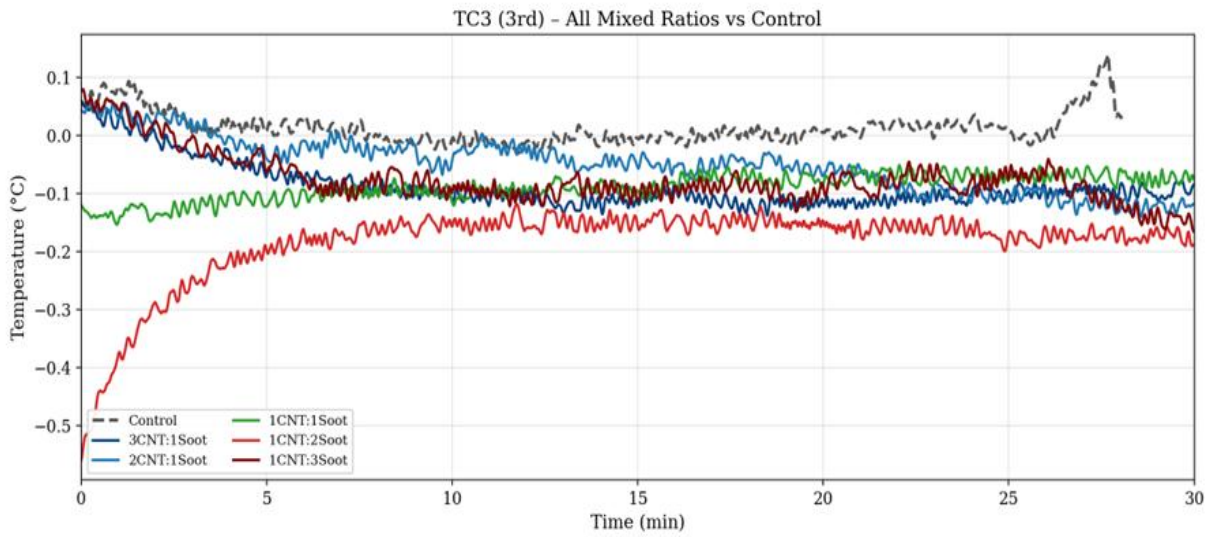

Figure 89: TC3 temperature vs. time for all mixed ratios and the control. No significant departure from the melting plateau is observed at this intermediate height for any mixed ratio

The TC4 per-height plot is the most information-dense of the four and is presented separately as a dedicated surface summary plot in Section 5.1.4.4.

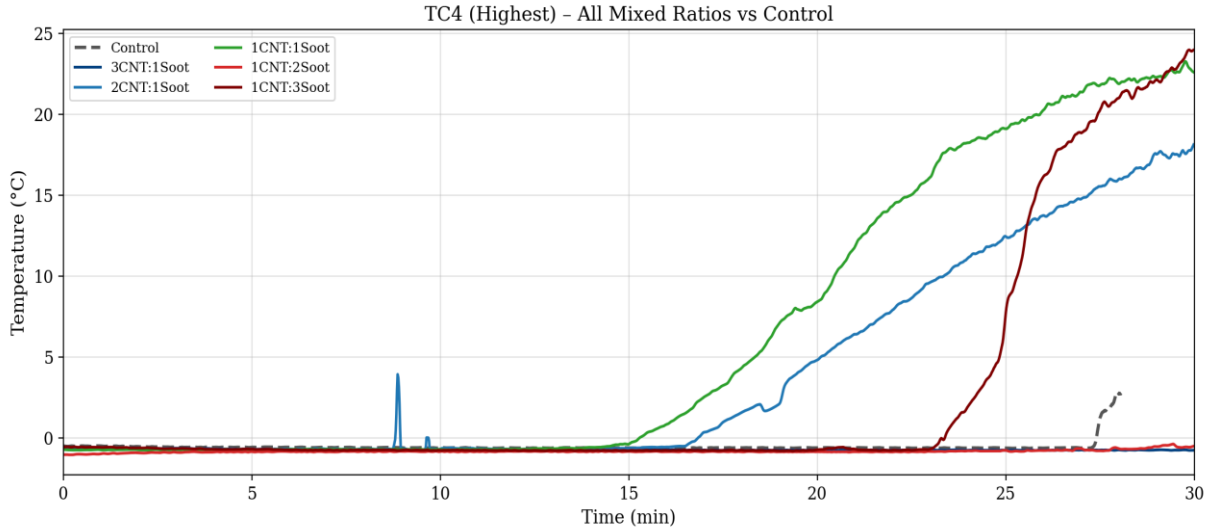

Figure 90: . TC4 (highest height, at the ice surface) temperature vs. time for all mixed ratios and the control. Three ratios (2CNT:1Soot, 1CNT:1Soot, 1CNT:3Soot) produce marked surface temperature rises at different onset times and peak magnitudes. The 3CNT:1Soot 1Soot and 1CNT:2Soot ratios remain near the control baseline throughout

5.1.4.4 TC4 Surface Response – Compositional Window Analysis

The TC4 temperature profiles for all mixed ratios, overlaid on a single axis with the control, are presented in the figure below. This is the most diagnostic plot of the section, as TC4 is the direct sensor of surface photothermal activity.

The plot makes the compositional window effect immediately apparent. Reading from CNT-dominant to soot-dominant:

3CNT:1Soot — flat, tracking control throughout (onset: none, peak: −0.43 °C).

2CNT:1Soot — earliest onset (t ≈ 8.8 min), moderate peak (18.5 °C), sustained elevation.

1CNT:1Soot — intermediate onset (t ≈ 16.1 min), highest peak (23.6 °C), longest sustained high-temperature episode.

1CNT:2Soot — flat, tracking control throughout (onset: none, peak: 0.009 °C).

1CNT:3Soot — latest onset (t ≈ 23.6 min), high peak (24.2 °C), steep rise only in the final 6 minutes.

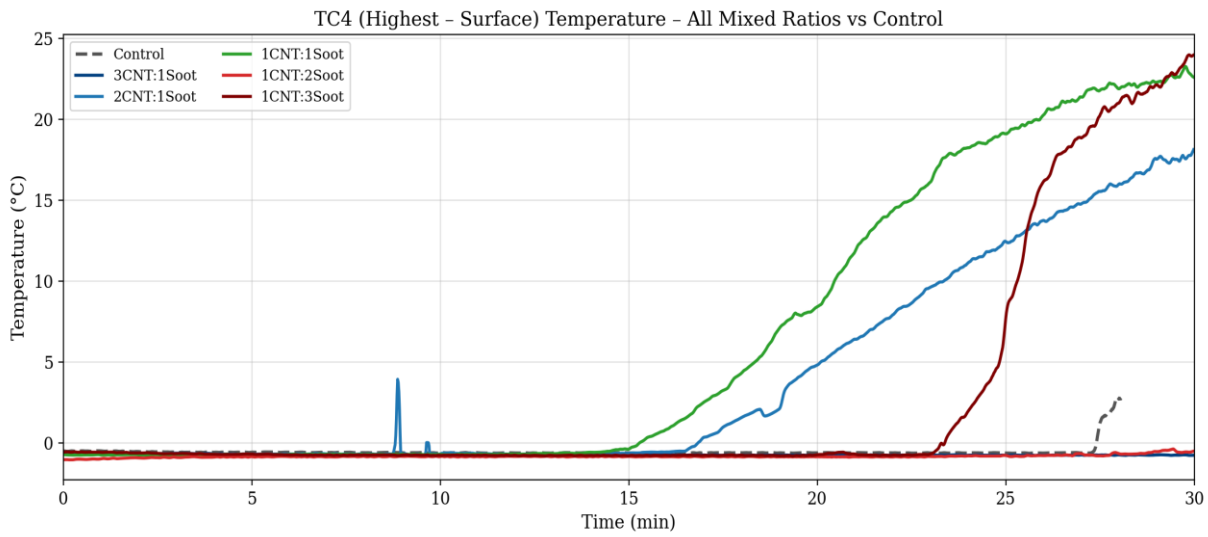

Figure 91: TC4 (surface) temperature vs. time for all five mixed ratios and the pure-ice control. The non-monotonic, asymmetric response reveals a compositional window: two ratios (3CNT:1Soot and 1CNT:2Soot) produce no surface heating, while three active ratios show onset times and peak temperatures that do not vary monotonically with CNT fraction

The non-monotonic pattern, with suppression at both 3:1 CNT and 2:1 Soot and active responses at the intermediate and extremes, suggests that the photothermal efficiency of the mixed deposit is governed by a complex interplay between the optical properties of the two components and how they interact when co-deposited. One possible mechanism is that at certain ratios, the CNT and Soot particles form aggregated clusters that increase effective light scattering and reduce absorption efficiency below the threshold needed to generate meaningful surface heating. At the 3CNT:1Soot ratio, CNT may dominate the surface optical properties but at a diluted Soot fraction, the combination loses the broadband absorptivity advantage that pure CNT 25 mg possesses. Similarly, at the 1CNT:2Soot ratio, the limited CNT content may disrupt the Soot particle packing in a way that reduces the effective absorptance of the Soot layer without compensating CNT-driven absorption.

The recovery of a strong response at 1CNT:3Soot, where soot dominates at 75% is consistent with the fact that soot 25 mg (pure) was one of the strongest surface-heating agents in Section 5.1.2. At this high soot fraction, the soot component dominates the optical behavior of the deposit, and

the small CNT addition does not suppress it. The 1CNT:1Soot and 2CNT:1Soot responses may reflect regimes where both components contribute constructively to broadband absorption, but with different activation kinetics.

5.1.4.5 Summary

The mixed-ratio experiments reveal that combining CNT and soot in a binary surface deposit does not produce a simple linear interpolation between the properties of the two pure materials. Instead, the photothermal behavior of the mixture is highly sensitive to the exact compositional ratio, exhibiting a non-monotonic response with two suppression ratios (3CNT:1Soot and 1CNT:2Soot) and three active ratios (2CNT:1Soot, 1CNT:1Soot, and 1CNT:3Soot), all at the same total mass of 25 mg.

Three key findings stand out from this series. First, TC1 through TC3 are thermally inert in all five mixtures, confirming that the surface deposition mechanism produces exclusively surface-localized photothermal heating regardless of mixture composition. Second, the onset time and peak temperature of TC4 are non-monotonic functions of the CNT fraction, with 2CNT:1Soot producing the earliest onset and 1CNT:3Soot producing the latest, while the peak temperatures for the three active mixtures span a relatively narrow range (18.5–24.2 °C). Third, two specific ratios completely suppress surface heating, a finding that has no precedent in the pure-material experiments and points to synergistic particle interactions in the mixed deposit that remain to be characterized.

These results suggest that the photophysical properties of carbonaceous particle mixtures on ice surfaces cannot be predicted from the properties of their individual components alone, and that real-world deposition scenarios involving mixed aerosol compositions may exhibit highly variable

albedo-reduction and ice-melting effects depending on the precise ratio of absorbing particle types present.

5.1.5 Scaled up Ice experiment

All experiments described in Sections 5.1.2 through 5.1.4 were conducted in the small crushed-ice container shown in Figure 20. To assess whether the photothermal melting behavior observed at the milligram scale is reproducible and consistent at a larger scale, the experiment was repeated using the scaled-up container shown in Figure 22, which has a volume approximately three times larger than the original. The surface deposition method from Section 5.1.2 was retained, with the contaminant applied uniformly to the top ice surface. Given the threefold increase in container cross-sectional area, the deposited mass was scaled accordingly: 1 g of CNT and 1 g of soot were used respectively, maintaining the same areal mass density as the 25 mg experiments on the small container. The same four-thermocouple array (TC1 at the lowest height through TC4 at the highest, at the ice surface), 240 Hz QuickDAQ acquisition, and the TC4 full-melt end-point criterion were maintained throughout.

This section provides an important check on dimensional scaling of the photothermal effect: if the mechanism is truly a surface phenomenon governed by areal contaminant density rather than total mass, the TC4 response should reproduce the qualitative features observed at the small scale, with the only expected difference being a longer absolute melt time due to the greater ice volume.

5.1.5.1 Scaled-Up Control Experiment

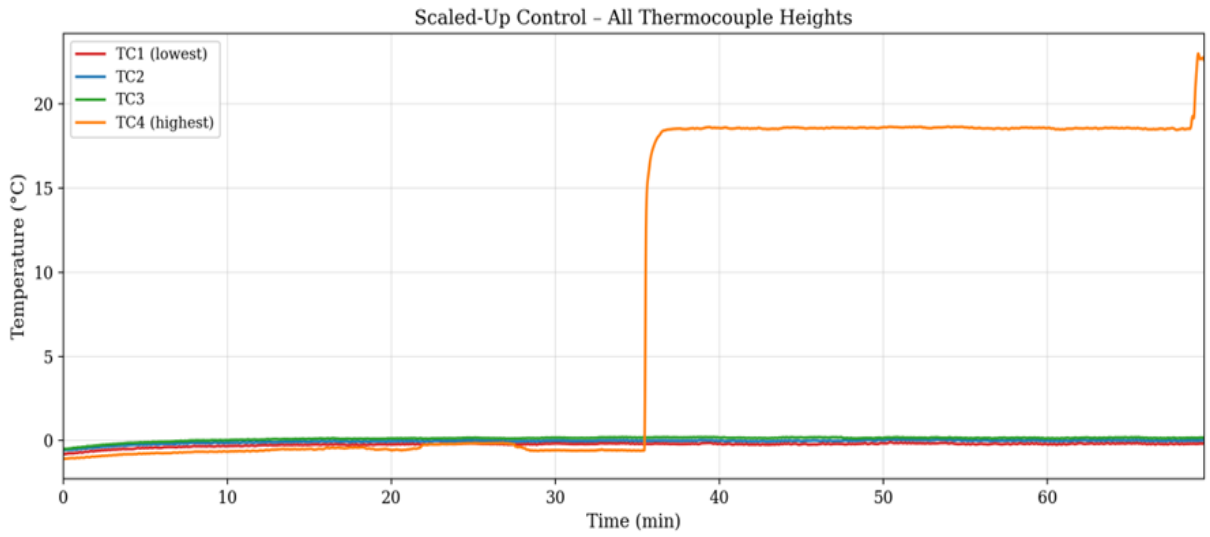

Figure 92: Temperature vs. time at all four thermocouple heights for the scaled-up pure-ice control. TC1–TC3 remain near 0 °C while TC4 rises from approximately t = 35.5 min, reaching 23.7 °C. Total experiment duration: 69.6 minutes

The scaled-up control experiment ran for 69.6 minutes, more than twice the 28.1-minute control duration for the small container, directly reflecting the greater thermal mass of the larger ice volume. TC1 showed occasional excursions (max +1.25 °C, mean −0.25 °C) attributable to sensitivity at the container base. TC2 and TC3 remained firmly at the melting plateau throughout (means of −0.06 and +0.10 °C respectively), consistent with bulk ice undergoing latent-heat-dominated melting.

TC4 began rising above 1 °C at approximately t = 35.5 minutes, reaching a peak of 23.7 °C, the defined endpoint of the scaled-up control. The 35.5-minute onset represents a 29% increase over the small-container control (27.5 min), broadly consistent with sub-linear scaling of melt-front velocity with container depth. The TC4 mean of +8.82 °C reflects the prolonged high-temperature episode following melt-front arrival at the surface thermocouple over the long experiment duration.

5.1.5.2 Soot 1 g – Scaled-Up Surface Deposit

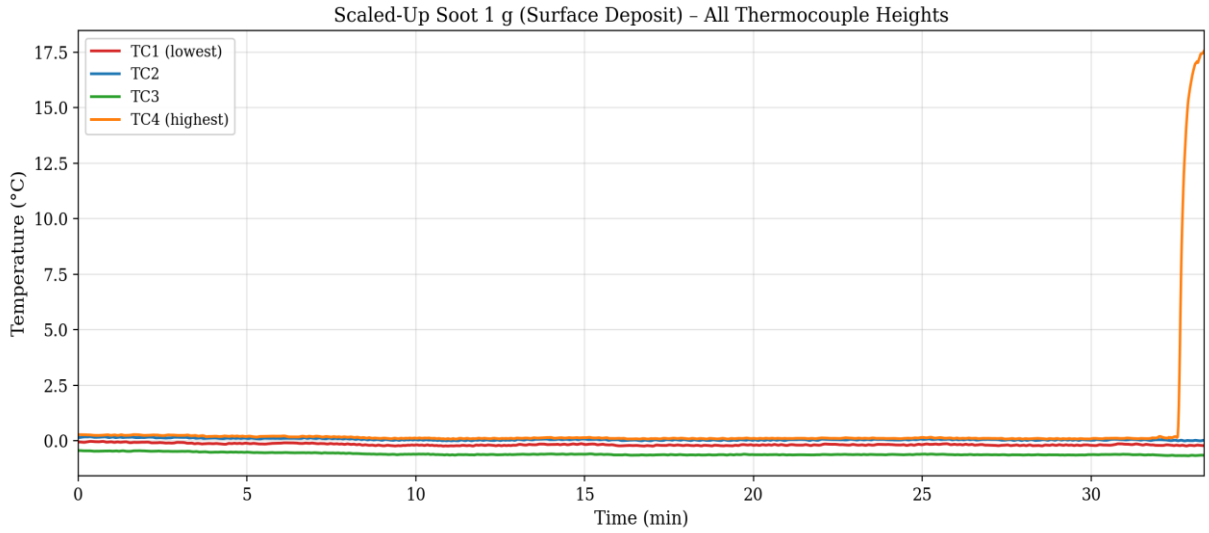

Figure 93:Temperature vs. time at all four thermocouple heights for Soot 1 g in the scaled-up container. TC1–TC3 remain near 0 °C throughout. TC4 rises from t ≈ 32.6 min, reaching a peak of 17.8 °C — 2.9 minutes earlier than the scaled-up control — confirming photothermal acceleration of surface melting at the gram scale

The Soot 1 g experiment ran for 33.4 minutes and produced the earliest surface response of the three scaled-up experiments.

TC1 remained near the melting plateau throughout (mean −0.17 °C, max +0.23 °C). TC2 similarly showed no meaningful departure (mean +0.07 °C, max +0.40 °C). TC3 showed a negative offset throughout (mean −0.59 °C, max −0.20 °C), reflecting a slight sub-plateau cooling effect from the soot deposit at that height.

TC4 began rising above 1 °C at approximately t = 32.6 minutes — 2.9 minutes earlier than the scaled-up control — reaching a peak of 17.8 °C (mean +0.47 °C). This confirms that photothermal acceleration of surface melting is preserved at the 1 g / scaled-up geometry, with TC4 remaining the sole active channel, consistent with all small-container surface experiments.

5.1.5.3 CNT 1 g – Scaled-Up Surface Deposit

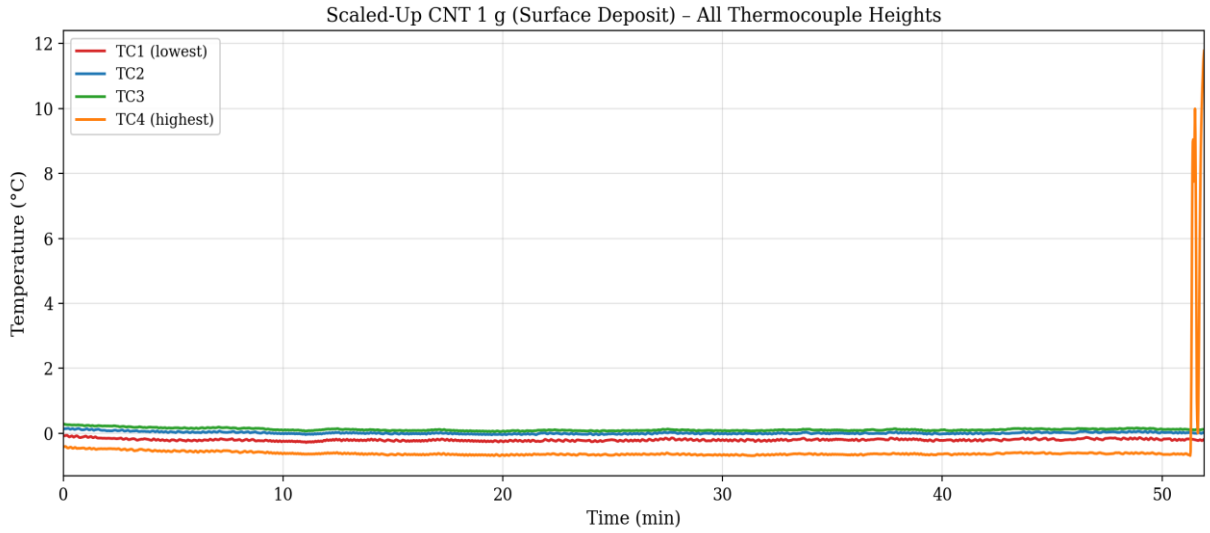

Figure 94:Temperature vs. time at all four thermocouple heights for CNT 1 g in the scaled-up container. TC1–TC3 remain near 0 °C throughout. TC4 rises at t ≈ 51.3 min, reaching 12.9 °C — 15.8 minutes later than the scaled-up control — indicating that the thick CNT surface deposit delays rather than accelerates the TC4 melt event in the larger geometry

The CNT 1 g experiment ran for 51.9 minutes — the longest of the three scaled-up runs — and produced the weakest surface response.

TC1 remained near the melting plateau throughout (mean −0.20 °C, max +0.29 °C). TC2 similarly showed no meaningful departure (mean +0.01 °C, max +0.32 °C). TC3 remained near zero (mean +0.12 °C, max +0.38 °C), with a slightly positive offset consistent with the melting plateau rather than photothermal activity.

TC4 rose above 1 °C at approximately t = 51.3 minutes — 15.8 minutes later than the scaled-up control — reaching a peak of 12.9 °C (mean −0.53 °C). Unlike the small-container soot experiments where surface deposits accelerated TC4 onset, the thick 1 g CNT blanket at this scale delays the surface melting event. The thick CNT layer appears to act as a partial thermal insulator, attenuating rather than amplifying the net radiative heat flux reaching the ice surface.

5.1.5.4 Comparison: CNT vs Soot vs Control (Scaled Up)

Average Temperature

The averaged four-TC profiles for all three experiments are presented below on a common 70-minute axis. The CNT 1 g average shows a modest elevation above the control in the final minutes of its 51.9-minute run driven by TC4, then terminates. The soot 1 g average shows a modest TC4 spike at t ≈ 32.6 min. The control sustains the highest long-term average beyond t = 35 min due to its prolonged TC4 high-temperature plateau. Neither contaminant at the 1 g / scaled-up scale produces the dramatic average elevations seen at 25 mg in the small-container experiments, reflecting the dominant contribution of the large thermally stable ice volume to the overall sample average.

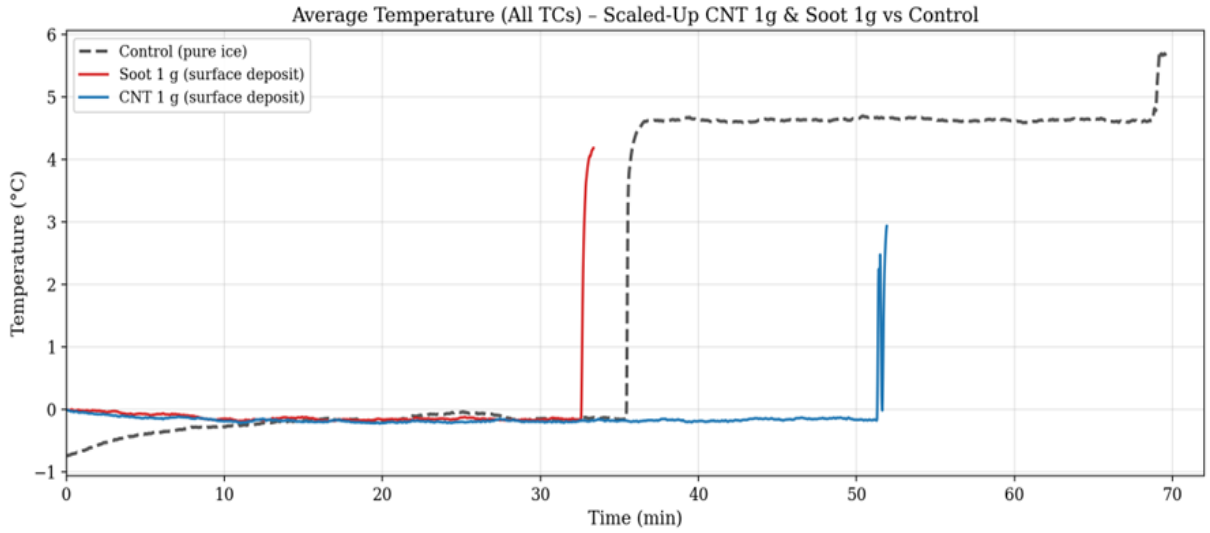

Figure 95: Average temperature of all four thermocouples for CNT 1 g, Soot 1 g, and the scaled-up pure-ice control. Soot 1 g shows an early modest TC4 spike; CNT 1 g terminates latest; the control sustains the highest long-term average

Per-Thermocouple Height Analysis

The per-height figures below confirm that TC1, TC2, and TC3 are thermally inert in all three scaled-up experiments, photothermal heating remains strictly surface-localized at TC4, consistent

with all small-container surface experiments. The TC4 plot shows the clearest separation between experiments, with the three onset times diverging by nearly 19 minutes across the Soot–Control–CNT ordering.

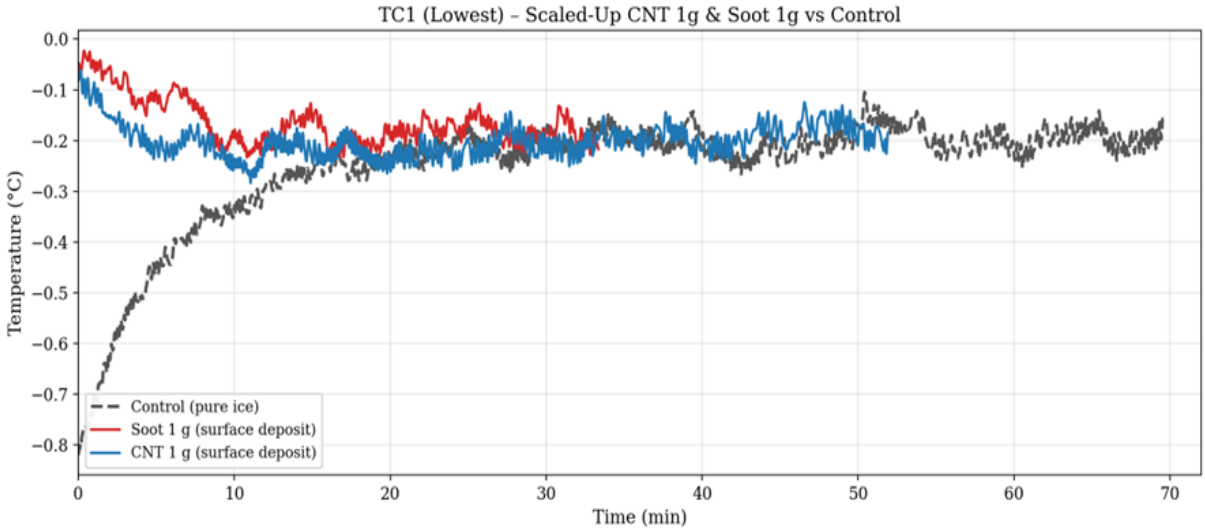

Figure 96: TC1 (lowest height) — all scaled-up experiments. All curves remain near 0 °C throughout with no influence from surface deposits at this height

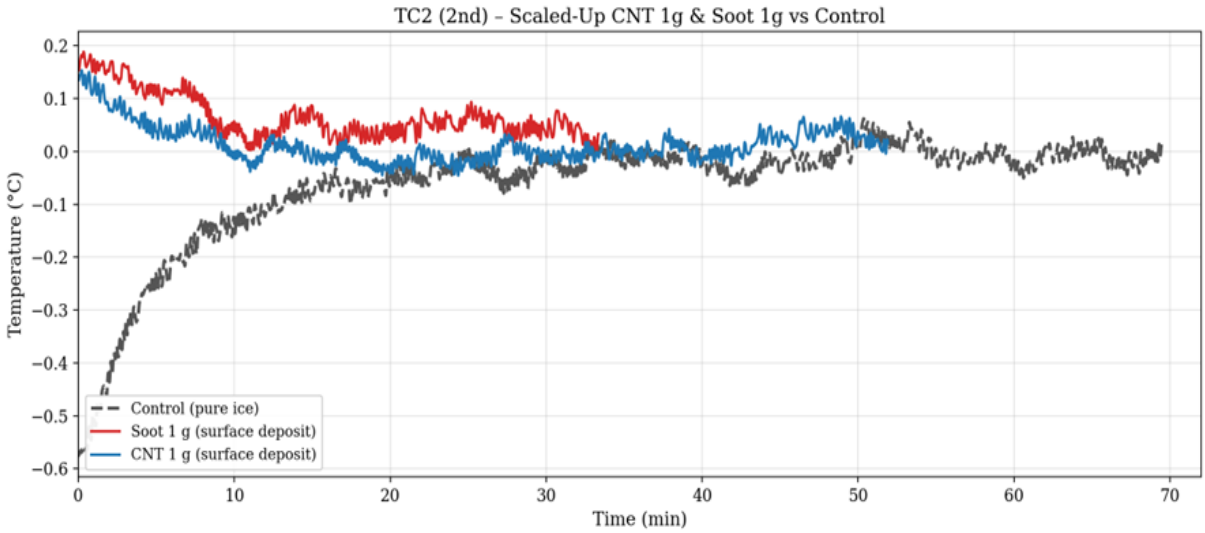

Figure 97: TC2 — all scaled-up experiments. All three experiments remain at the near-0 °C melting plateau; no departure observed for either contaminant

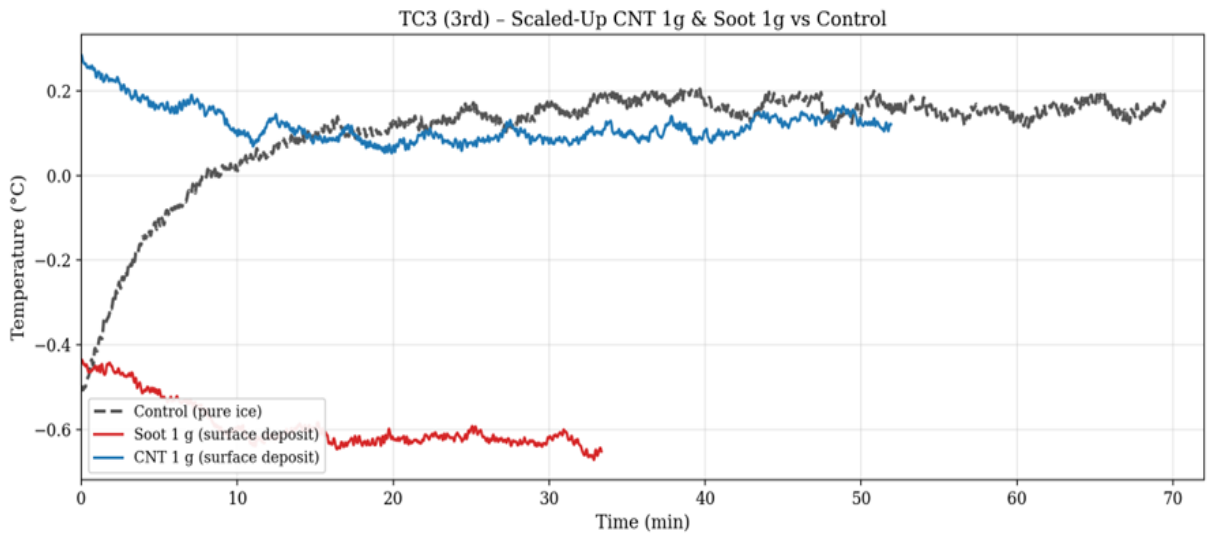

Figure 98: TC3 — all scaled-up experiments. No departure from the melting plateau is observed at this height for any experiment, confirming strict surface localization of photothermal heating in the scaled-up geometry

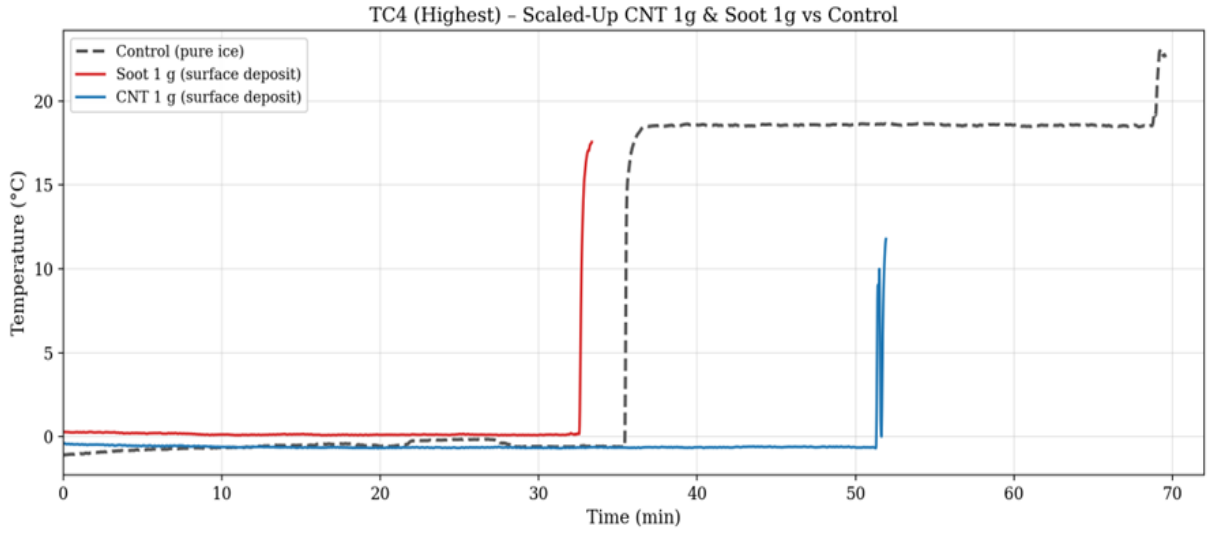

Figure 99: TC4 (surface) — all scaled-up experiments. Soot 1 g rises earliest (t ≈ 32.6 min, peak 17.8 °C), the control intermediate (t ≈ 35.5 min, peak 23.7 °C), and CNT 1 g latest (t ≈ 51.3 min, peak 12.9 °C) — a span of nearly 19 minutes between earliest and latest TC4 onsets

The TC4 profiles overlaid in Figure 99 provide the clearest summary of the scaling results. The soot curve rises 2.9 minutes before the control; the CNT curve rises 15.8 minutes after. This places the control precisely between the two contaminants in terms of surface melt timing. All three curves rise to broadly comparable peak temperatures once the melt front reaches TC4 (23.7, 17.8, and 12.9 °C for control, soot, and CNT respectively), suggesting that the contaminant deposit

governs the timing of TC4 onset but not the subsequent rate of temperature rise once the surface ice layer melts.

5.1.5.5 Summary and Scaling Discussion

The scaled-up experiments confirm that the fundamental surface-photothermal mechanism identified in Section 5.1.2 is robust across a threefold change in container geometry: TC4 remains the sole active thermocouple in all three scaled-up experiments, and TC1 through TC3 remains thermally inert throughout, exactly as observed in the small-container experiments. Three principal findings emerge.

First, the scaled-up control confirms sub-linear scaling of melt time: the TC4 onset increased by 29% (27.5 to 35.5 min) for a threefold volume increase, indicating that the small container benefits from edge effects and a more favorable surface-to-volume ratio that modestly accelerates the melt front relative to a direct dimensional scaling prediction.

Second, soot 1 g advances TC4 onset by 2.9 minutes relative to the scaled-up control, confirming that photothermal acceleration scales to the gram loading level. The advance is smaller in absolute terms than at the 25 mg small-scale, consistent with the greater thermal mass that must be overcome before the melt front reaches TC4 in the larger geometry.

Third, CNT 1 g delays TC4 onset by 15.8 minutes relative to the control, reversing the acceleration trend observed in the small-container CNT 25 mg experiment. This reversal indicates a material- and geometry-dependent transition between an accelerating and a retarding regime for CNT surface deposits, with the transition occurring somewhere between the 25 mg small-scale and the 1 g scaled-up loading. Characterizing this transition would require systematic experiments at intermediate scales and loadings.

Together, these results establish that the photothermal mechanism is qualitatively preserved at scale but that the quantitative effect on melt timing is highly sensitive to contaminant type, loading density, and container geometry. The divergence between soot and CNT behavior, one advancing and one delaying TC4 onset at the same total mass, highlights the importance of characterizing each material independently across a range of scales before drawing conclusions about their real-world impact on ice and snow melting.

5.2 Solid Ice Experiment

The solid ice container (Figure 23), described in Section 4.2.2, was used for this set of experiments. The same surface deposition approach from Section 5.1.2 was applied, with 1 g of CNT and 1 g of soot deposited on the solid ice surface respectively. Compared to crushed ice, solid ice starts well below 0 °C and has higher thermal conductivity, meaning all thermocouples begin at sub-zero temperatures and warm gradually toward the melting point before any surface event occurs.

5.2.1 Control experiment

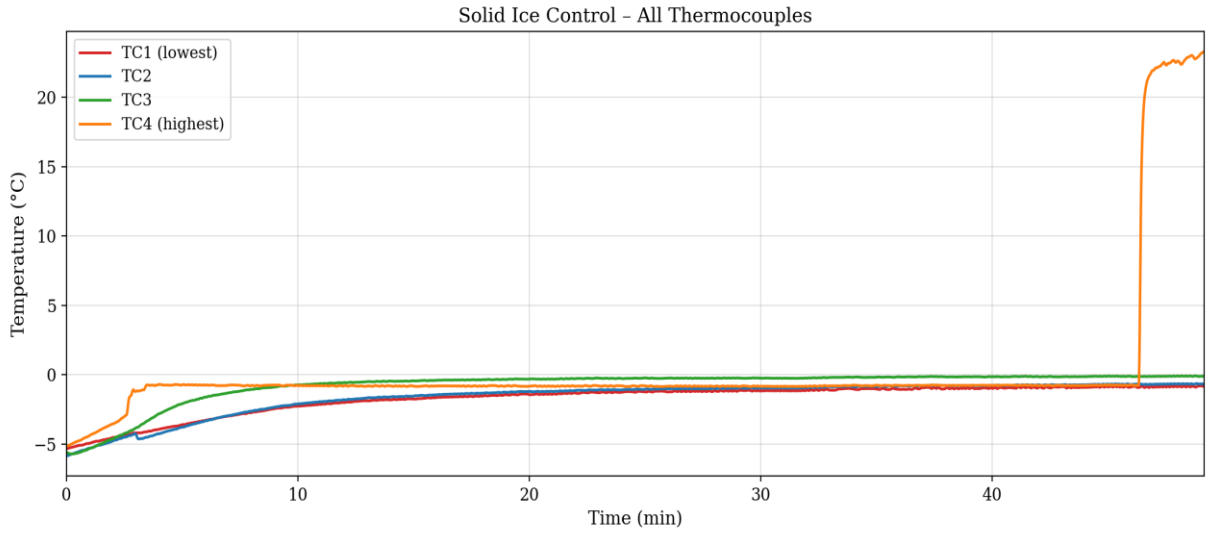

Figure 100: Solid ice control — all four thermocouples. All channels start near −5 °C and warm conductively. TC4 rises at t = 46.4 min, reaching 23.5 °C (total duration: 49.2 min)

All four thermocouples began at approximately −5 °C, reflecting the initially frozen solid block. TC1–TC3 warmed gradually toward 0 °C but remained subzero throughout. TC4 rose above 1 °C at t = 46.4 minutes, reaching a peak of 23.5 °C and ending at 49.2 minutes. The warming gradient across TC1–TC3 is a direct consequence of solid-ice conduction, unlike crushed ice, the thermal front propagates conductively through the dense ice block rather than via a sharp melt-front step.

5.2.2 Impact of Embedded Contaminant

5.2.2.1 Carbon Nano Tubes

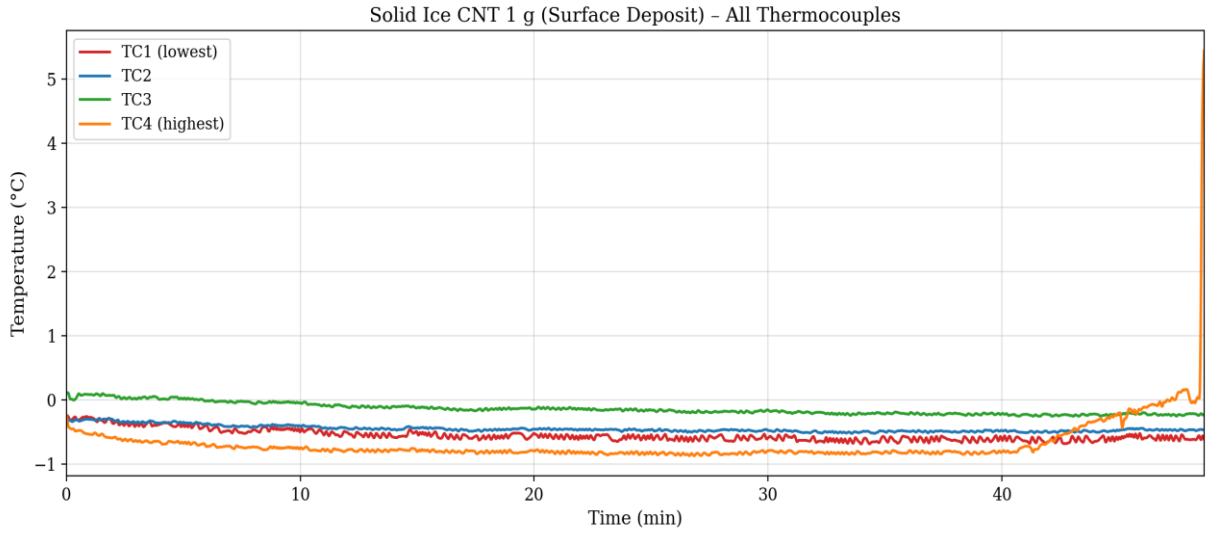

Figure 101: Solid ice CNT 1 g — all thermocouples. TC1–TC3 warm conductively as in the control. TC4 rises marginally later than the control (t = 48.5 min) with a much lower peak of 6.0 °C

TC1–TC3 followed a similar gradual warming profile to the control throughout the 48.7-minute run. TC4 rose to t=48.5 minutes, 2.1 minutes later than the control, reaching a peak of only 6.0 °C. The reduced peak and delayed onset indicate that the CNT deposit does not significantly accelerate surface melting on the solid ice block; if anything, it marginally retards it, possibly because the thick CNT layer insulates the ice surface from ambient heat input. The lower TC4 peak (6.0 vs 23.5 °C) suggests the melt event was less intense, consistent with a surface layer that partially attenuates rather than amplifies the thermal input.

5.2.2.2 Soot

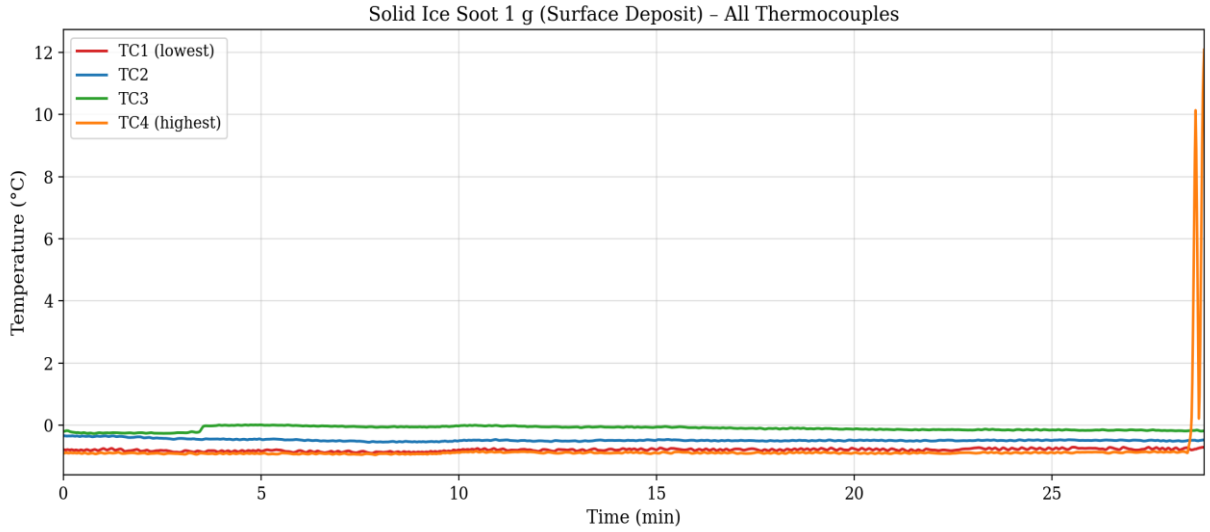

Figure 102:Solid ice Soot 1 g — all thermocouples. TC1–TC3 remain subzero throughout. TC4 rises sharply at t = 28.6 min, 17.8 minutes earlier than the control, reaching 13.4 °C (total duration: 28.9 min)

Soot 1 g produced the strongest and earliest response of all solid ice experiments. TC1–TC3 remained below zero throughout (means of −0.80, −0.48, and −0.11 °C), while TC4 rose above 1°C at t = 28.6 minutes,17.8 minutes earlier than the control, reaching a peak of 13.4 °C. The experiment ended at 28.9 minutes, the shortest of all solid ice runs. This confirms that the soot surface deposit is a far more effective photothermal agent than CNT on the solid ice surface, accelerating the TC4 melt event by nearly 18 minutes relative to the uncontaminated block.

5.2.2.3 Comparison

The TC4 overlay below places all three solid ice experiments on a single axis. Soot dramatically advances the surface melt event while CNT shows a negligible and slightly delayed response relative to the control; a clear divergence between the two materials on solid ice.

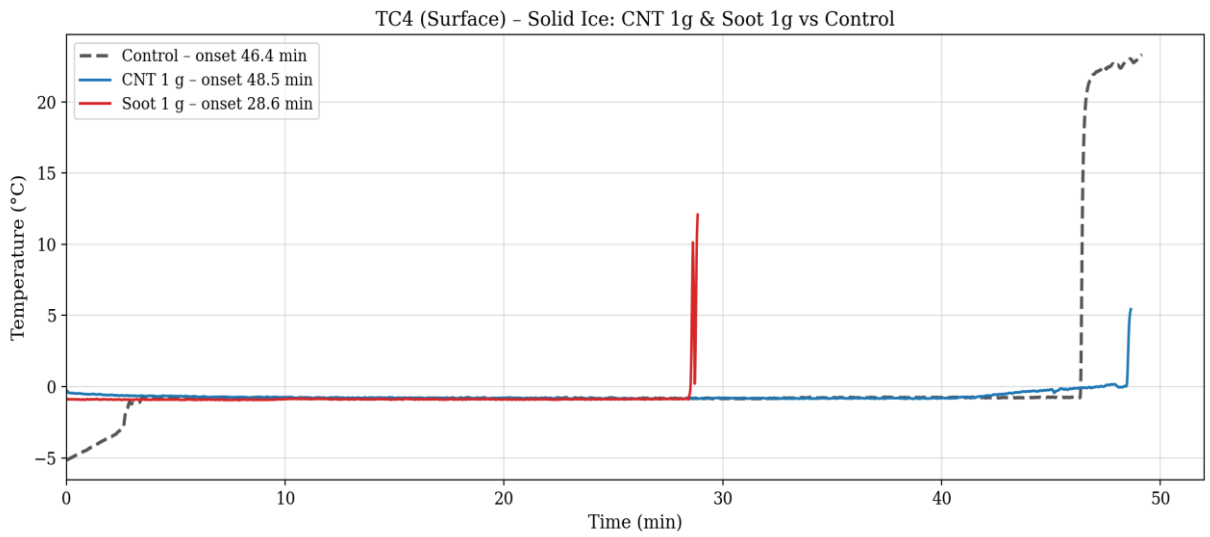

Figure 103: TC4 surface overlay — solid ice. soot 1 g advances TC4 onset by 17.8 min vs control; CNT 1 g delays it by 2.1 min. The three curves span a 19.9-minute range in TC4 onset time

The average temperature comparison and per-height profiles below confirm that the photothermal effect remains strictly surface-localized: TC1–TC3 are near-identical across all three experiments and only TC4 distinguishes them.

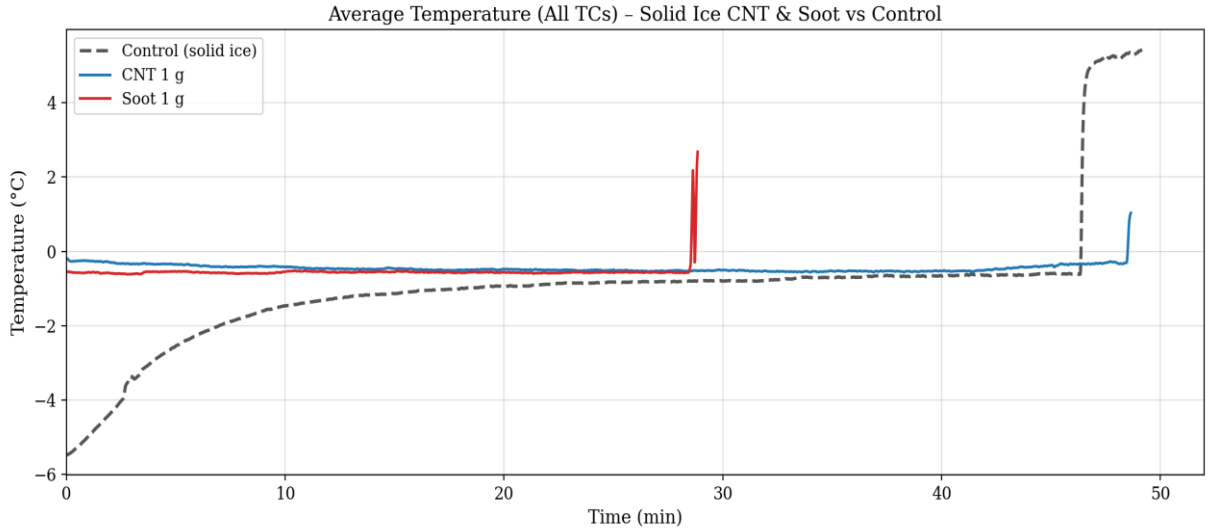

Figure 104: Average temperature (all TCs) — solid ice. soot 1 g produces the highest average driven by its early TC4 rise. CNT 1 g and control track closely together throughout

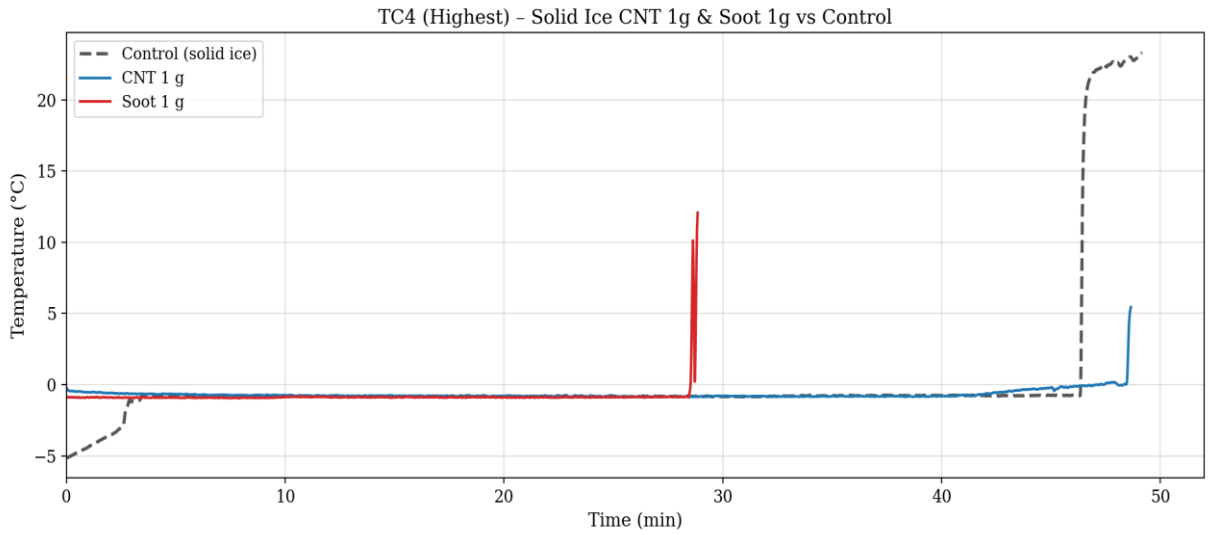

Figure 105: TC4 per-experiment overlay — solid ice, confirming onset times: soot 1 g (28.6 min) < control (46.4 min) < CNT 1 g (48.5 min)

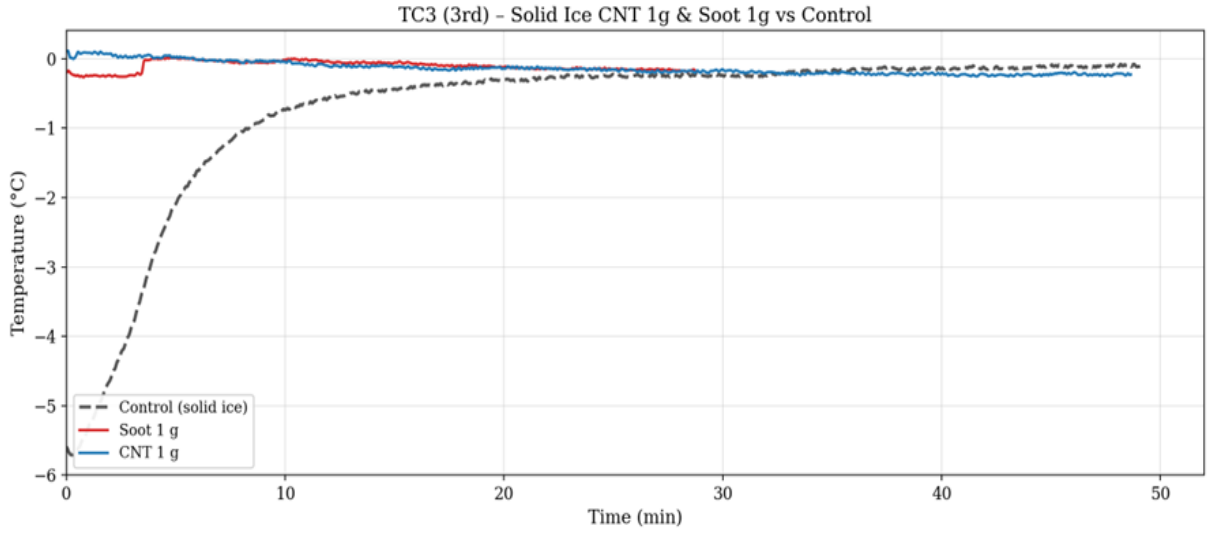

Figure 106:TC3 — all solid ice experiments. No departure from the conductive warming baseline for any experiment at this height

5.2.3 Comparison with Scaled-Up Crushed Ice Experiment

The side-by-side TC4 comparison below contrasts the solid ice results directly with the scaled-up crushed ice experiments from Section 5.1.5. Several key differences emerge from the two ice types.

In crushed ice, all experiments begin at 0 °C (latent-heat plateau) and TC4 rises when the melt front reaches the surface. In solid ice, all experiments begin at −5 °C and TC4 rises only after the block has conductively warmed to the melting point; resulting in longer baseline times and a qualitatively different temperature profile shape (gradual ramp vs flat plateau).

For CNT: in crushed ice CNT advanced TC4 by 2.9 min; in solid ice it delayed it by 2.1 min. The behavior inverts between ice types, suggesting that the CNT deposit's photothermal benefit is marginal and sensitive to the thermal boundary conditions of the ice structure.

For soot: soot accelerated TC4 onset in solid ice (−17.8 min) but delayed it in crushed ice (+15.8 min). On solid ice the soot layer clearly channels solar energy into the ice surface, triggering early melting. On the larger crushed-ice volume, the same 1 g deposit could not overcome the greater thermal mass within the experiment window, resulting in the observed delay.

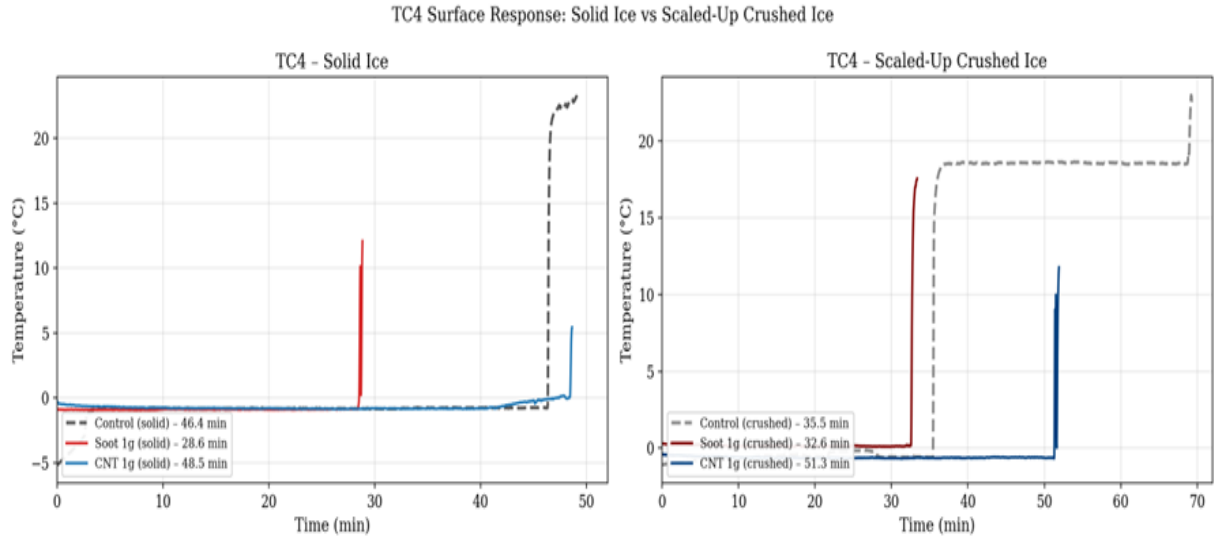

Figure 107: TC4 surface response comparison: solid ice (left) vs scaled-up crushed ice (right). Soot accelerates TC4 onset in solid ice but delays it in crushed ice. CNT shows marginal effects in both cases. The contrasting profiles reflect the fundamental differences in starting temperature, ice density, and thermal conductivity between the two ice types

5.2.4 Summary

The solid ice experiments confirm that the surface-photothermal mechanism identified in Section 5.1.2 extends to dense, conduction-dominated ice structures, though with fundamentally different thermal dynamics. Unlike crushed ice, which begins at 0 °C under a latent-heat plateau, the solid ice block starts at approximately −5 °C and warms conductively before any surface event occurs, meaning TC4 onset times are longer, and the temperature profiles reflect conductive heat transfer rather than a propagating melt front. Despite this, TC4 remains the sole thermocouple that registers photothermal activity, and TC1 through TC3 remains on the conductive warming baseline in all three experiments, preserving the surface-localized character of the mechanism. Three principal findings emerge.

First, the solid ice control establishes a longer baseline TC4 onset of 46.4 minutes, compared to 35.5 minutes for the scaled-up crushed ice control, reflecting the additional energy required to first warm the frozen block from −5 °C to the melting point before the surface melt event can occur. This confirms that ice type, not only container volume, is a primary determinant of melt timing.

Second, soot 1 g advances TC4 onset by 17.8 minutes relative to the solid ice control (28.6 vs 46.4 min), representing the strongest photothermal acceleration observed in any 1 g experiment. This contrasts with the scaled-up crushed ice result where the same soot loading advanced TC4 by only 2.9 minutes, indicating that soot's photothermal effectiveness is amplified by the slower conductive baseline of solid ice.

Third, CNT 1 g delays TC4 onset by 2.1 minutes relative to the solid ice control (48.5 vs 46.4 min), a negligible retarding effect in the same direction as observed on scaled-up crushed ice

(15.8 min delay). The consistently retarding CNT response across both ice types at the 1 g loading confirms that the thick deposit acts primarily as a surface insulator at gram-scale quantities, attenuating rather than amplifying the net thermal input regardless of ice structure.

Together, these results demonstrate that the photothermal mechanism is qualitatively preserved across ice types, TC4 surface localization holds in both crushed and solid ice, but the quantitative impact is strongly modulated by the thermal properties of the ice substrate. Soot emerges as the more effective photothermal agent across both geometries, while CNT shows consistently retarding effects at the 1 g scale in both ice types. These findings underscore that real-world assessments of contaminant-driven ice melting must account not only for the nature and mass of the surface deposit but also for the density, initial temperature, and conductive properties of the underlying ice formation.

Chapter 6: Discussion and Conclusion

6.1 Discussion

6.1.1 Synthesis of Experimental Findings

This study investigated the photothermal ice-melting behavior of soot and carbon nanotubes across five experimental variables: contaminant type, mass loading, deposition geometry, mixed-ratio composition, and ice structure. A single dominant finding emerged across all 22 configurations: photothermal heating is strictly surface-localized. TC4, the thermocouple positioned at the contaminant-ice interface, was the sole channel to register radiation-driven temperature rises in every experiment. TC1 through TC3 remained thermally inert regardless of contaminant type, loading, or deposition geometry, confirming that the carbonaceous surface layer absorbs incident infrared radiation and generates heat exclusively at the air-ice interface without measurably penetrating the bulk ice within the experimental timeframe. This is consistent with the albedo-reduction mechanism described in Section 2.4 and with field observations of black carbon-driven surface warming in polar regions [3, 12].

At milligram-scale surface loadings, both materials accelerated melting relative to the pure-ice control, but the response was non-monotonic with mass: both soot and CNT produced near-zero TC4 activity at 15 mg despite strong responses at 5 mg and 25 mg. This suppression, consistent across two chemically distinct materials, indicates a deposit-structural threshold in optical coupling rather than a simple absorptance effect, and suggests that moderate contamination levels may not produce proportionate melt acceleration. At gram-scale loadings, the two materials diverged sharply: soot consistently advanced TC4 onset in both the scaled-up crushed ice and solid ice configurations, while CNT delayed it in both, confirming a material-dependent divergence that is robust across ice types.

The layered deposition experiments demonstrated that distributing contaminant mass throughout the ice column reduces photothermal effectiveness relative to equivalent surface loading, with the surface-closest layer dominating the TC4 response in all cases. The mixed-ratio experiments revealed a further complexity: two specific CNT-to-soot ratios completely suppressed TC4 heating at 25 mg total mass while three others remained active, demonstrating that binary carbonaceous deposits produce emergent optical behavior that cannot be predicted from single-material results alone. Finally, the comparison between crushed and solid ice confirmed that substrate structure is as important a determinant of photothermal effectiveness as contaminant type: the same gram-scale soot deposit advanced TC4 onset by 17.8 minutes on solid ice but only 2.9 minutes on crushed ice.

6.1.2 Why 15 mg Melts Later Than the Control: Proposed Mechanism

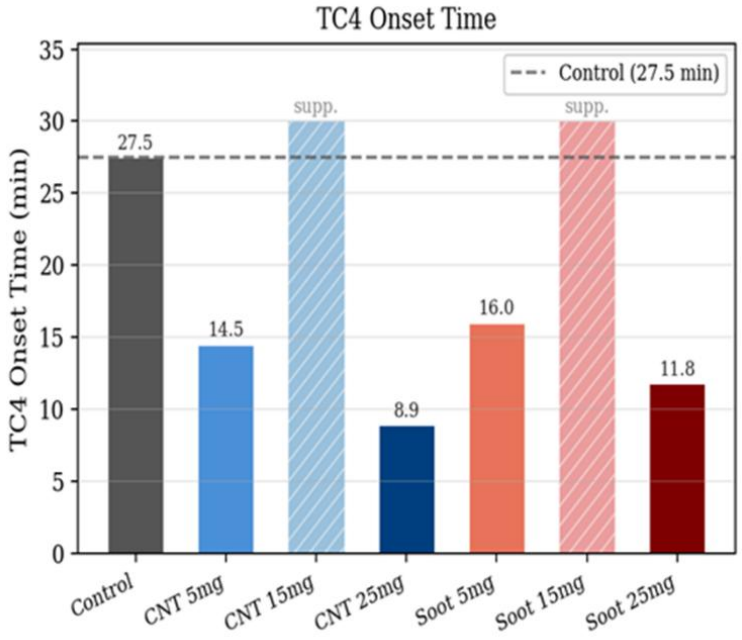

Figure 108: TC4 onset time for all surface deposition experiments (Section 5.1.2). Both CNT 15 mg and Soot 15 mg are suppressed (hatched), melting later than the control despite containing three times the mass of the 5 mg cases, confirming the non-monotonic loading dependence

The complete suppression of TC4 heating at 15 mg surface loading for both soot and CNT is the most counterintuitive finding of this study. Despite containing three times the mass of the 5 mg case, the intermediate loading consistently failed to accelerate surface melting above the control baseline. The proposed explanation combines an optical effect and a mechanical effect that operate simultaneously and compound each other.

The optical effect is rooted in radiative heat transfer and is supported by the 3D light microscope surface profiles of Figures 12 and 18, which show that the 15 mg deposit sits in a structural transition zone between the thin absorbing regime at 5 mg and the bulk absorbing regime at 25 mg. At 5 mg, the deposit is sparse and discontinuous, allowing direct radiation contact with the ice surface and reducing albedo effectively. At 25 mg, the deposit is sufficiently thick to function as a bulk absorber: incident radiation is absorbed within the layer itself, the layer heats up, and energy is conducted downward into the ice. At 15 mg, the intermediate deposit thickness creates a poorly coupled particulate blanket that reflects rather than absorbs a significant fraction of incident radiation, reducing the net radiative flux reaching the ice surface below it. This behavior is consistent with the radiative transfer framework of Khuller and Warren [30], who showed that as particulate loading on ice increases, absorption initially dominates but eventually saturates and scattering by the deposit becomes the governing mechanism, causing the effective albedo of the surface to partially recover. The 15 mg loading appears to sit precisely in this reflective transition zone for both materials.

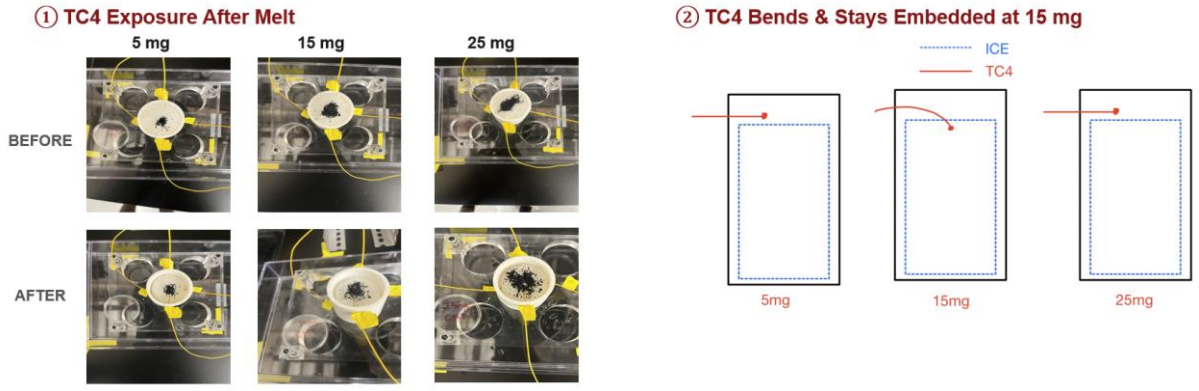

Figure 109: Before and after melt photographs at 5 mg, 15 mg, and 25 mg surface loadings (left), and schematic of TC4 wire behavior at each loading (right)

The mechanical effect reinforces the optical one. As shown in the before-and-after photographs and the thermocouple bending diagram, at 5 mg and 25 mg the TC4 wire is fully exposed after melting and correctly records the melt event. At 15 mg, the TC4 wire bends under the weight and structural pressure of the intermediate-thickness deposit and remains embedded in residual ice below the nominal surface height. Even as the surface ice melts and drops, TC4 stays in contact with ice and registers no temperature rise. The melt occurs but TC4 cannot detect it.

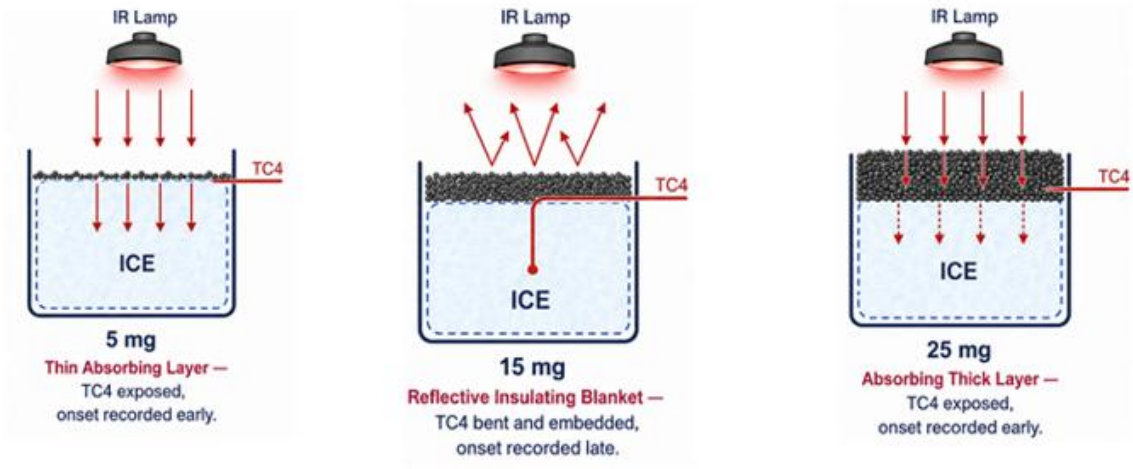

Figure 110: Schematic of the proposed photothermal mechanism at each mass loading under infrared irradiation. At 5 mg, the thin sparse deposit absorbs radiation directly and TC4 is exposed, recording an early onset. At 15 mg, the intermediate-thickness deposit reflects incident radiation back upward and TC4 bends into residual ice, producing a late recorded onset. At 25 mg, the thick deposit absorbs radiation in bulk and conducts heat into the ice, TC4 is exposed, and onset is recorded early

Because both the optical blanket effect and the mechanical TC4 displacement are governed by deposit thickness rather than material chemistry, they affect soot and CNT identically at the same mass loading. The 15 mg anomaly is therefore not a material-specific result but a deposit-structural one, with important implications for real-world contamination scenarios: moderate aerosol deposition levels on polar ice may produce less melt acceleration than either lower or higher loading concentrations. Further theoretical support for the absorption-to-reflection transition is provided by Mishchenko et al. [31], who established through rigorous radiative transfer analysis that optically thick particulate layers exhibit bidirectional reflectance behavior dominated by scattering rather than absorption, this confirms that once a deposit exceeds a critical optical thickness, as observed at 15 mg in this study, the layer acts as a reflector rather than an absorber of incident radiation, fundamentally altering the net energy delivered to the ice surface below.

6.1.3 CNTs vs Soot: Why the Lab-Scale Result Inverts the Environmental Expectation

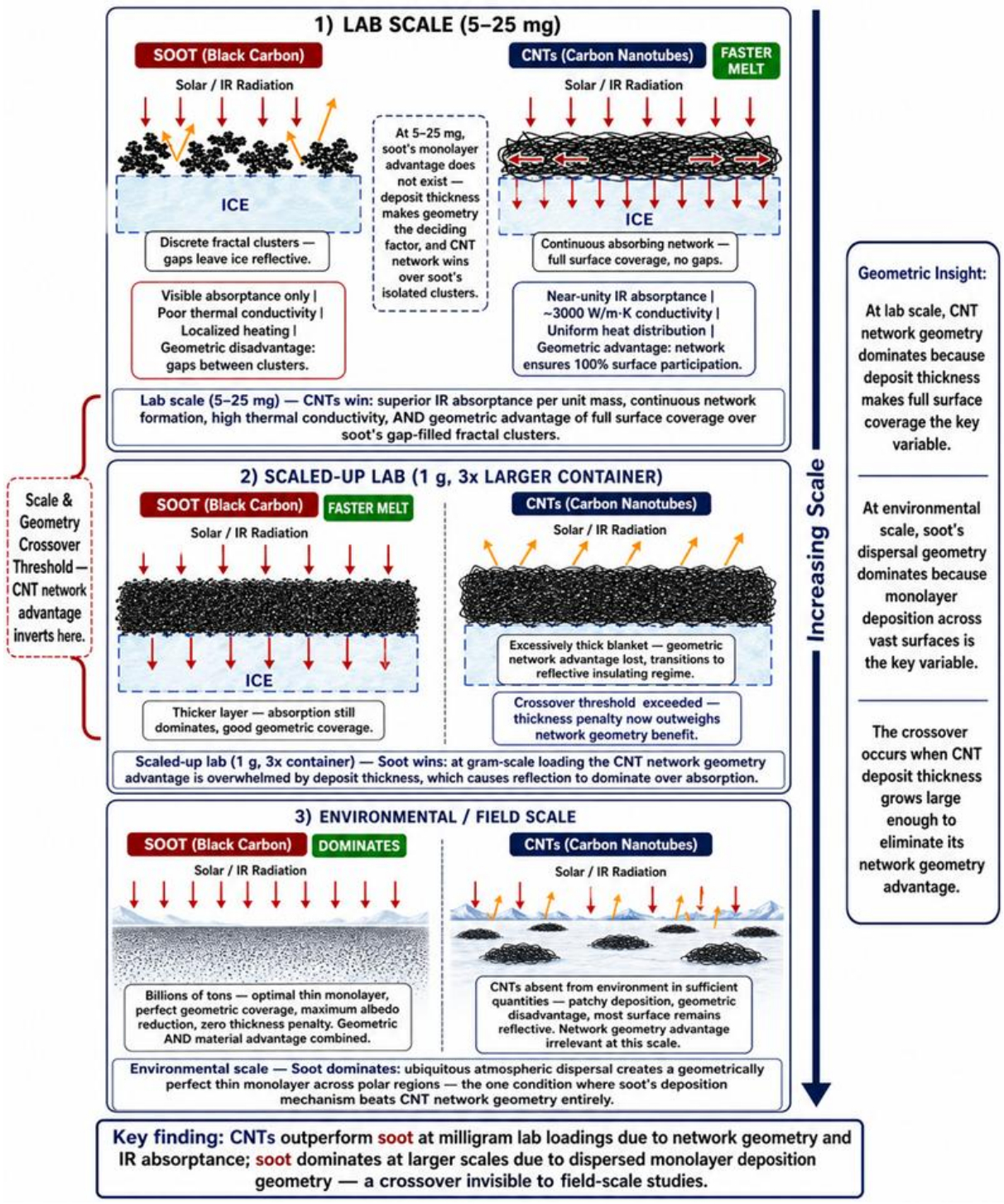

Figure 111: Scale-dependent photothermal mechanism of soot and CNTs across three regimes. At lab scale (5–25 mg), CNTs outperform soot due to continuous network geometry, near-unity IR absorptance, and high thermal conductivity, while soot's fractal clusters leave reflective gaps. At gram-scale loading, the CNT deposit transitions into a reflective insulating blanket and soot dominates. At environmental scale, soot's ubiquitous monolayer deposition across polar surfaces provides a geometric advantage that CNTs cannot replicate. The crossover occurs when CNT deposit thickness grows large enough to eliminate its network geometry advantage

At laboratory-scale loadings of 5 to 25 mg, CNTs consistently outperform soot in accelerating surface melting, contrary to environmental literature predictions. This inversion may be driven by three cooperative CNT advantages: near-unity broadband IR absorptance, continuous fibrous network geometry ensuring full surface coverage with no reflective gaps, and axial thermal conductivity of approximately 3000 W/m·K enabling rapid heat conduction into the ice. As illustrated in Figure 111, these factors give CNTs a decisive advantage over soot's discrete fractal aggregates when deposit thickness, rather than total dispersed mass, governs the photothermal response.

At larger scale loading this relationship inverts. The CNT deposit becomes thick enough that scattering dominates over absorption and the insulating blanket mechanism takes over, while soot's compact cluster morphology remains in the absorption-dominant regime and its melt-acceleration advantage re-emerges.

At environmental scale, soot dominates entirely for geometric rather than material reasons. Hansen and Nazarenko [32] confirmed that atmospheric transport deposits soot as an optimal thin monolayer across polar surfaces, generating a radiative forcing of approximately 0.3 W/m² in the Northern Hemisphere, while the NASA visualization [33] directly demonstrates how trace soot concentrations progressively darken ice. CNTs are absent from the environment in sufficient quantities to form their network advantage, making their deposition patchy and geometrically inefficient [32]. This scale-dependent crossover is invisible to field-scale studies and has not previously been identified in controlled laboratory experimentation [32, 33].

6.2 Conclusions

1. Photothermal heating is strictly surface-localised. TC4 was the sole active thermocouple in every experiment; TC1–TC3 remained thermally inert regardless of contaminant type, loading, or deposition method.

2. Both soot and CNT accelerate surface melting at milligram scale, but soot is the more consistent and scalable photothermal agent. At gram-scale loading, soot advanced TC4 onset in both ice configurations while CNT delayed it in both, driven by the reflective insulating blanket mechanism that limits CNT effectiveness beyond the milligram scale.

3. The photothermal response is non-monotonic with loading. Both materials exhibited complete TC4 suppression at 15 mg surface loading, revealing a loading-dependent threshold in deposit optical coupling that produces counterintuitive behavior at intermediate concentrations.

4. Layered deposition reduces photothermal effectiveness relative to surface deposition. Distributing the total mass throughout the ice column consistently delayed and reduced TC4 heating compared to equivalent surface loading, with the surface-closest layer dominating the response in all cases.

5. Mixed CNT-soot deposits exhibit a non-additive compositional window effect. Two specific ratios completely suppressed TC4 heating at a fixed total mass of 25 mg, demonstrating that binary carbonaceous deposits cannot be characterized from single-material results alone.

6. Ice structure is a primary determinant of photothermal effectiveness. The same gram-scale soot deposits advanced TC4 onset by 17.8 minutes on solid ice but only 2.9 minutes on crushed ice, confirming that substrate density, conductivity, and initial temperature are as important as contaminant properties in governing melt acceleration.

6.3 Potential Applications of the Insulating Blanket Effect

The intermediate-loading insulating blanket effect identified in this study, wherein a carbonaceous deposit of intermediate thickness reflects rather than absorbs incident radiation, has direct relevance to several engineering applications. At controlled loadings within the absorption-dominant regime, CNT-based sprayable coatings could be applied to road and rooftop surfaces to passively accelerate snow melting under solar irradiance, reducing reliance on chemical de-icing agents; to aircraft wing leading edges as a lightweight passive supplement to active anti-icing systems, leveraging CNT axial thermal conductivity of approximately 3000 W/m·K to distribute heat uniformly across the surface; to cold-weather apparel and personal protective equipment to simultaneously absorb solar radiation and reduce radiative heat loss from the body; and to outdoor industrial pipelines and infrastructure to provide passive freeze protection during daylight hours. The low density of CNTs, approximately 1300 to 1400 kg/m³ compared to 8960 kg/m³ for copper, makes all of these applications weight competitive. However, deployment must be approached with caution: inhaled CNT fibers pose documented respiratory and potential carcinogenic risks at occupational exposure levels, CNTs are persistent in aquatic environments and toxic to marine organisms at microgram-per-liter concentrations, and any spray-applied system must be engineered to remain above the insulating blanket thickness threshold identified in this study to ensure net heat delivery to the substrate rather than reflection of incident radiation away from it.

6.4 Recommendations for Future Work

Four areas are identified for future investigation. First, the transition in CNT behavior between accelerating (25 mg small-scale) and retarding (1 g scaled-up) TC4 onset was not resolved. Systematic experiments at intermediate masses (50–500 mg) would identify the transition loading and the mechanism governing the reversal. Second, the mixed-ratio suppression window warrants

dedicated optical characterization of co-deposited layers at suppressing and non-suppressing ratios using diffuse reflectance spectroscopy and SEM, to determine whether suppression is driven by increased scattering, absorption saturation, or changes in deposit packing structure. Third, the effect of forced convection on the photothermal melting mechanism should be investigated. The experimental setup includes a fan for controlled airflow; applying varying fan speeds would quantify how surface wind conditions modify the heat balance at the contaminated ice surface and alter TC4 onset time, adding an environmental variable directly relevant to polar wind-driven melt scenarios. Fourth, extending the experiment to non-uniform and wet deposition conditions would bring the laboratory setup closer to real Arctic aerosol deposition scenarios, where particles are not uniformly applied but transported and deposited by wind and precipitation. Fifth, developing a coupled numerical model of the experimental setup using ANSYS Fluent or ANSYS Mechanical would allow the effective surface absorptance and internal temperature gradients measured by TC1–TC4 to be reproduced computationally, with agreement between simulated and experimental TC4 onset times validating the proposed heat transfer mechanisms and enabling parametric studies beyond the experimental range.

References

[1] S. G. W. a. W. J. Wiscombe, "A model for the spectral albedo of snow. II: Snow containing atmospheric aerosols," *Journal of the Atmospheric Sciences,* vol. 37, no. 12, p. 2734–2745, 1980.

[2] A. G. a. M. Sharp, "A review of snow and ice albedo and the development of a new physically based broadband albedo parameterization," *Journal of Geophysical Research,* vol. 115, no. F01009, 2010.

[3] C. Z. J. R. a. P. R. M. Flanner, "Present-day climate forcing and response from black carbon in snow," *Journal of Geophysical Research,* vol. 112, no. D11202, 2007.

[4] T. C. B. e. al., "Bounding the role of black carbon in the climate system: A scientific assessment," *Journal of Geophysical Research: Atmospheres,* vol. 118, p. 5380–5552, 2013..

[5] K. L. a. A. Stohl, "Arctic air pollution: Origins and impacts," *Science,* vol. 315, no. 5818, p. 1537–1540, 2007.

[6] S. D. e. al., "Light-absorbing impurities in Arctic snow," *Journal of Geophysical Research,* vol. 115, no. D17302, 2010.

[7] Z. C. a. V. P. P. Avouris, "Carbon-based electronics," *Nature Nanotechnology,* vol. 2, p. 605–615, 2007.

[8] E. P. e. al., "Thermal conductance of an individual single-wall carbon nanotube," *Nano Letters,* vol. 6, no. 1, p. 96–100, 2006.

[9] IPCC, "Climate Change 2021: The Physical Science Basis," Cambridge University Press, 2021. [Online]. Available: https://www.ipcc.ch/report/ar6/wg1/. [Accessed 22 March 2026].

[10] T. B. a. R. Bergstrom, "Light absorption by carbonaceous particles: An investigative review," *Aerosol Science and Technology,* vol. 40, no. 1, p. 27–67 2006., 2006.

[11] Y. Z. Y. Q. a. H. W. S. Kang, "A review of black carbon in snow and ice and its impact on the cryosphere," *Earth-Science Reviews,* vol. 210, 2020.

[12] O. L. H. a. T. W. Kirchstetter, "Black-carbon reduction of snow albedo," *Nature Climate Change,* vol. 2, p. 437–440, 2012.

[13] T. S. J. C. Y. C. Y. Z. a. X. W. W. Pu, "Enhancement of snow albedo reduction and radiative forcing due to coated black carbon in snow," *The Cryosphere,* vol. 15, p. 2255–2272 , 2021.

[14] A. A. M. a. M. D. King, "The effects of additional black carbon on the albedo of Arctic sea ice: variation with sea ice type and snow cover," *The Cryosphere,* vol. 7, p. 1193–1204, 2013.

[15] T. J. Y. S. J. D. e. a. Y. Qian, "Light-absorbing particles in snow and ice: Measurement and modeling of climatic and hydrological impact," *Advances in Atmospheric Sciences,* vol. 32, p. 64–91, 2015.

[16] The Engineering ToolBox, "Ice – Thermal Properties," [Online]. Available: https://www.engineeringtoolbox.com/ice-thermal-properties-d_576.html. [Accessed 26 March 2026].

[17] D. M. Q. W. K. G. a. H. D. E. Pop, "Thermal conductance of an individual single-wall carbon nanotube," *Nano Letters,* vol. 6, no. 1, p. 96–100, 2006.

[18] A. N. V. e. al., "Thermal conductivity of carbon nanotube networks: a review," *Journal of Materials Science,* vol. 54, p. 7926–7953, 2019.

[19] A. G. Yunus Cengel, Heat and Mass Transfer - Fundamentals and Applications, New York, NY: McGraw-Hill Education, 2019.

[20] Y. Cengel, Fluid Mechanics: Fundamentals and Applications, McGraw-Hill Higher Education, 2024.

[21] D. P. D. T. L. B. a. A. S. L. F. P. Incropera, Fundamentals of Heat and Mass Transfer, NJ: Wiley, 7th ed. Hoboken, , 2011.

[22] S. G. Warren, "Optical properties of snow," *Reviews of Geophysics,* vol. 20, no. 1, p. 67–89, 1982.

[23] K. M. e. al., "A black body absorber from vertically aligned single-walled carbon nanotubes," *Proceedings of the National Academy of Sciences,* vol. 106, no. 15, 2009.

[24] J. M. e. al., Vogel’s Textbook of Quantitative Chemical Analysis, 6th ed. Prentice Hall, 2000.

[25] K. S. Suslick, "Sonochemistry," *Science,* vol. 247, no. 4949, p. 1439–1445, 1990.

[26] L. Bergström, "Hamaker constants of inorganic materials," *Advances in Colloid and Interface Science,* vol. 70, p. 125–169, 1997.

[27] A. H. Rosenfeld, "The role of reflective materials in reducing building heat gain," *Energy and Buildings,* vol. 22, no. 1, p. 1–7, 1995.

[28] V. F. P. a. R. W. Whitworth, Physics of Ice, Oxford University Press, 1999.

[29] YU XING,, "Adjustable Brooder Lamp — 10.5″ Aluminium Reflector and Bulb Guard, 250 V 660 W," YX228," [Online]. Available: https://yx228.com/product/brooder_lamp/. [Accessed Febuary 2026].

[30] A. P. K. a. S. G. Warren, "Spectral albedo of dusty Martian H_2O snow and ice," *J. Geophys. Res. Planets,* vol. 126, no. e2021JE006910, 2021.

[31] M. I. M. e. al, "Bidirectional reflectance of flat, optically thick particulate layers," *J. Quant. Spectrosc. Radiat. Transfer,* vol. 63, p. 409–432, 1999.

[32] J. H. a. L. Nazarenko, "Soot climate forcing via snow and ice albedos," *PNAS,* vol. 101, no. 2, p. 423–428, 2004.

[33] S. Twardy, "Ice Albedo: Black Soot and Snow," NASA, 9 February 2004. [Online]. Available: https://svs.gsfc.nasa.gov/20023/. [Accessed 20 April 2026].

[34] S. X. J. H. a. Z. Z. Sigrid Ronneberg, "Nanoscale Correlations of Ice Adhesion Strength and Water Contact Angle," *MDPI,* 2020.